Applied Maritime Physics

Ocean Environment, Structures, and Safety

Vahit ÇALIŞIR, PhD

EĞİTİM
yayınevi

Applied Maritime Physics Ocean Environment, Structures, and Safety
Vahit Çalışır

Chairman of the Publishing House Group: Yusuf Ziya Aydoğan (yza@egitimyayinevi.com)
Editor in Chief: Yusuf Yavuz (yusufyavuz@egitimyayinevi.com)
Interior Designer: Kübra Konca Nam
Cover Designer: Egitim Publishing House Design Department

Turkish Republic Ministry of Tourism and Culture
Publisher Certificate No: 76780

E-ISBN: 978-625-385-819-3
1. Edition, March 2026

Library Information Card
Applied Maritime Physics Ocean Environment, Structures, and Safety
Vahit Çalışır
170 s., 150x220 mm
Includes references, no index.
E-ISBN: 978-625-385-819-3

EĞİTİM yayınevi

Publisher Türkiye Office: İstanbul: Eğitim Yayınevi Tic. Ltd. Şti., Atakent mah. Yasemen sok. No: 4/B, Ümraniye, İstanbul, Türkiye

Konya: Eğitim Yayınevi Tic. Ltd. Şti., Fevzi Çakmak Mah. 10721 Sok. B Blok, No: 16/B, Safakent, Karatay, Konya, Türkiye +90 332 351 92 85, +90 533 151 50 42
bilgi@egitimyayinevi.com

Publisher USA Office: New York: Egitim Publishing Group, Inc.
P.O. Box 768/Armonk, New York, 10504-0768, United States of America
americaoffice@egitimyayinevi.com

Logistics and Shipping Center: Kitapmatik Lojistik ve Sevkiyat Merkezi, Fevzi Çakmak Mah. 10721 Sok. B Blok, No: 16/B, Safakent, Karatay, Konya, Türkiye
sevkiyat@egitimyayinevi.com

Bookstore Branch: Eğitim Kitabevi, Şükran mah. Rampalı 121, Meram, Konya, Türkiye
+90 332 499 90 00
bilgi@egitimkitabevi.com
Internet Sales: www.kitapmatik.com.tr
bilgi@kitapmatik.com.tr

EĞİTİM YAYINEVİ GRUBU

Contents

Preface ix

1 Wave Mechanics and Ocean Waves 1
- 1.1 Introduction . . . 1
- 1.2 Scientific Background . . . 1
  - 1.2.1 Fundamentals of Wave Physics . . . 1
  - 1.2.2 Classification of Ocean Waves . . . 2
  - 1.2.3 Wave Generation by Wind . . . 3
- 1.3 Theoretical Framework . . . 4
  - 1.3.1 Linear Wave Theory (Airy Wave Theory) . . . 4
  - 1.3.2 Deep Water and Shallow Water Approximations . . . 8
  - 1.3.3 Wave Energy and Power . . . 10
  - 1.3.4 Wave Refraction, Diffraction, and Reflection . . . 15
  - 1.3.5 Wave Spectra and Statistical Description . . . 16
  - 1.3.6 Wave Statistics and Extreme Values . . . 19
- 1.4 Applications in Maritime Systems . . . 19
  - 1.4.1 Wave Loads on Ships and Offshore Structures . . . 19
  - 1.4.2 Wave Forecasting and Hindcasting . . . 21
- 1.5 Discussion . . . 22
- 1.6 Conclusion . . . 23

2 Electromagnetism and Maritime Navigation 27
- 2.1 Introduction . . . 27
- 2.2 Scientific Background . . . 27
  - 2.2.1 Maxwell's Equations and Electromagnetic Waves . . . 27
  - 2.2.2 Electromagnetic Radiation at the Sea Surface . . . 29
  - 2.2.3 Earth's Magnetic Field . . . 30
- 2.3 Theoretical Framework . . . 31
  - 2.3.1 Inherent Optical Properties of Seawater . . . 31
  - 2.3.2 Apparent Optical Properties and Underwater Irradiance 31
  - 2.3.3 Ocean Water Classification . . . 32
  - 2.3.4 Radar Physics and Principles . . . 33
  - 2.3.5 Antenna Theory for Maritime Applications . . . 33

2.3.6 Global Navigation Satellite Systems (GNSS) 34
2.3.7 Differential GNSS and Augmentation Systems 34
2.3.8 Magnetic Compass Physics 35
2.3.9 Gyroscope Physics and Inertial Navigation 36
2.3.10 Automatic Identification System (AIS) and VHF Communication 37
2.4 Applications in Maritime Systems 38
2.4.1 Electronic Chart Display and Information System (ECDIS) 38
2.4.2 Radar Navigation and Collision Avoidance (ARPA) . . 38
2.4.3 Voyage Data Recorder (VDR) 39
2.4.4 Long Range Identification and Tracking (LRIT) 39
2.5 Discussion 40
2.6 Conclusion 40

3 Marine Meteorology and Atmospheric Physics 43
3.1 Introduction 43
3.2 Scientific Background 43
3.2.1 Atmospheric Structure and Composition 43
3.2.2 Solar Radiation and Earth's Energy Balance 44
3.2.3 Atmospheric Pressure and Measurement 45
3.3 Theoretical Framework 46
3.3.1 Wind Systems and the Coriolis Effect 46
3.3.2 Global Atmospheric Circulation 47
3.3.3 Cyclones, Anticyclones, and Frontal Systems 47
3.3.4 Tropical Cyclones (Hurricanes/Typhoons) 48
3.3.5 Sea–Air Interaction 49
3.3.6 Visibility, Fog, and Precipitation Physics 50
3.3.7 Sea State and Wind–Wave Relationship 51
3.4 Applications in Maritime Systems 51
3.4.1 Weather Forecasting for Mariners 51
3.4.2 Weather Routing 52
3.4.3 Heavy Weather Seamanship 52
3.4.4 Ice Accretion Physics 53
3.5 Discussion 54
3.6 Conclusion 55

4 Physical Oceanography 57
4.1 Introduction 57
4.2 Scientific Background 57
4.2.1 Physical Properties of Seawater 57
4.2.2 Temperature and Salinity Distribution 58
4.2.3 Light and Sound in the Ocean 59
4.3 Theoretical Framework 60
4.3.1 Ocean Currents and Circulation 60

4.3.2 Thermohaline Circulation . . . 63
4.3.3 Tidal Physics . . . 65
4.3.4 Tidal Currents and Streams . . . 67
4.3.5 Geostrophic Currents and Sea Surface Topography . . . 68
4.3.6 Upwelling and Downwelling . . . 69
4.4 Applications in Maritime Systems . . . 69
4.4.1 Ocean Currents and Ship Routing . . . 69
4.4.2 Tidal Navigation . . . 70
4.4.3 Density Effects on Ship Draft and Stability . . . 71
4.4.4 Ice Physics and Polar Navigation . . . 71
4.5 Discussion . . . 72
4.6 Conclusion . . . 73

5 Structural Mechanics of Ships **77**
5.1 Introduction . . . 77
5.2 Scientific Background . . . 77
5.2.1 Fundamentals of Stress and Strain . . . 77
5.2.2 Material Properties of Shipbuilding Materials . . . 78
5.2.3 Beam Theory and Bending . . . 80
5.3 Theoretical Framework . . . 81
5.3.1 Hull Girder Bending . . . 81
5.3.2 Shear Force and Bending Moment Distribution . . . 81
5.3.3 Transverse Strength and Racking . . . 84
5.3.4 Local Structural Loading . . . 85
5.3.5 Buckling and Instability . . . 87
5.3.6 Fatigue Damage Mechanics . . . 88
5.3.7 Ship Vibration and Resonance . . . 90
5.3.8 Structural Reliability and Limit States . . . 91
5.4 Applications in Maritime Systems . . . 93
5.4.1 Classification Society Rules and Standards . . . 93
5.4.2 Finite Element Analysis (FEA) in Ship Structures . . . 94
5.4.3 Structural Health Monitoring . . . 94
5.4.4 Collision and Grounding Structural Response . . . 95
5.5 Discussion . . . 96
5.6 Conclusion . . . 97

6 Acoustics and Underwater Sound **101**
6.1 Introduction . . . 101
6.2 Scientific Background . . . 101
6.2.1 Fundamentals of Sound and Acoustic Waves . . . 101
6.2.2 Speed of Sound in Seawater . . . 102
6.2.3 Acoustic Impedance and Reflection . . . 103
6.3 Theoretical Framework . . . 104
6.3.1 Sonar Equation . . . 104
6.3.2 Sound Propagation in the Ocean . . . 105

6.3.3 Transmission Loss . . . 106
6.3.4 Ambient Noise in the Ocean . . . 108
6.3.5 Acoustic Doppler Effect . . . 109
6.3.6 Reverberation . . . 110
6.4 Applications in Maritime Systems . . . 110
6.4.1 Echo Sounding and Bathymetry . . . 110
6.4.2 Acoustic Doppler Current Profiler (ADCP) . . . 111
6.4.3 Sonar for Navigation and Obstacle Detection . . . 111
6.4.4 Underwater Communication . . . 112
6.4.5 Underwater Radiated Noise (URN) and Environmental Impact . . . 112
6.5 Discussion . . . 113
6.6 Conclusion . . . 113

7 Maritime Safety and Risk Physics 115
7.1 Introduction . . . 115
7.2 Scientific Background . . . 116
7.2.1 Risk Concepts and Probability Theory . . . 116
7.2.2 Fire Physics Fundamentals . . . 117
7.2.3 Explosion Mechanics Fundamentals . . . 118
7.3 Theoretical Framework . . . 118
7.3.1 Flooding and Damage Stability . . . 118
7.3.2 Fire Dynamics on Ships . . . 120
7.3.3 Explosion and Blast Loading . . . 121
7.3.4 Collision Mechanics . . . 122
7.3.5 Grounding Mechanics . . . 123
7.4 Applications in Maritime Systems . . . 124
7.4.1 Life-Saving Appliance Physics . . . 124
7.4.2 Quantitative Risk Assessment (QRA) . . . 124
7.4.3 Fire Detection and Suppression Systems . . . 126
7.4.4 Watertight Integrity . . . 127
7.4.5 Formal Safety Assessment (FSA) . . . 127
7.5 Discussion . . . 128
7.6 Conclusion . . . 130

8 Environmental Physics in Maritime Operations 133
8.1 Introduction . . . 133
8.2 Scientific Background . . . 133
8.2.1 Combustion Chemistry and Emission Formation . . . 133
8.2.2 Atmospheric Dispersion of Pollutants . . . 135
8.2.3 Suspended Particles in Seawater . . . 135
8.2.4 Oil Spill Physics . . . 136
8.3 Theoretical Framework . . . 137
8.3.1 Ship Energy Efficiency . . . 137
8.3.2 Greenhouse Gas Emissions and Carbon Accounting . 138

8.3.3 Ballast Water Treatment Physics 140
8.3.4 Underwater Noise and Marine Ecosystem Impact . . 140
8.4 Applications in Maritime Systems 141
8.4.1 Exhaust Gas Cleaning Systems (Scrubbers) 141
8.4.2 Alternative Fuels and Energy Sources 141
8.4.3 Oil Spill Response Physics 142
8.4.4 Antifouling and Hull Coatings 143
8.4.5 Waste Heat Recovery 143
8.5 Discussion 144
8.6 Conclusion 145

List of Abbreviations **147**

Glossary **151**

Preface

This book provides a unified treatment of the physical sciences that describe the ocean environment and their application to the structural integrity, acoustic behaviour, safety, and environmental impact of ships. It is intended for senior undergraduate and early postgraduate students in naval architecture, marine engineering, ocean engineering, and maritime science, and assumes familiarity with single-variable calculus, introductory mechanics, and basic thermodynamics.

A ship operates within a complex physical environment characterised by ocean waves, electromagnetic propagation, atmospheric dynamics, stratified water columns, and acoustic fields. Understanding these phenomena—and their implications for structural loading, navigation, safety, and environmental stewardship—is essential for the modern maritime engineer and ocean scientist. This text treats each domain from first principles, derives the governing equations, and connects them to maritime practice through worked applications.

The organisation begins with wave mechanics (Chapter 1), then addresses the broader physical environment—electromagnetic navigation, marine meteorology, and physical oceanography (Chapters 2–4). It continues with structural mechanics of ships (Chapter 5), underwater acoustics (Chapter 6), and concludes with maritime safety and risk physics (Chapter 7) and environmental physics in maritime operations (Chapter 8).

Vahit ÇALIŞIR
March 2026

Chapter 1

Wave Mechanics and Ocean Waves

1.1 Introduction

Ocean waves are the dominant environmental force acting on ships and offshore structures. Wave mechanics governs the prediction of wave loads, ship motions, structural design criteria, and safe navigation procedures. Waves are also generated by the vessel itself as it moves through water, and these ship-generated waves impose a fundamental speed limit on displacement hulls. Bejan et al. (2020) identified the transverse bow wave as a critical phenomenon that limits boat speed and shapes optimal hull proportions.

1.2 Scientific Background

1.2.1 Fundamentals of Wave Physics

A particularly important class of surface gravity waves for naval architecture is the transverse wave generated by a moving hull. As a displacement vessel moves through water at speed V, it generates a pattern of waves—the Kelvin wave pattern—consisting of divergent and transverse components. The transverse wave has a wavelength that increases with vessel speed.

Bejan et al. (2020) described the critical (or hull) speed as the velocity at which the wavelength of the transverse bow wave equals the waterline length of the boat:

Equation 6.1 — Critical (hull) speed:

$$V_c = \sqrt{\frac{g\, L_{WL}}{2\pi}} \tag{1.1}$$

where g is gravitational acceleration and L_{WL} is the waterline length. In the traditional imperial form used by Bejan et al. (2020), this expression reduces to $V_c \approx 1.25\,\sqrt{L_{WL}}$ with V_c in knots and L_{WL} in feet.

When a hull approaches V_c, the transverse bow wave grows and traps the boat in its own wave trough. The resistance increases sharply, and the boat

rides in a "cradle" formed by its own wave system (Bejan et al., 2020). Beyond V_c, the hull must climb over or plane on top of its bow wave, which requires a fundamentally different hull form (planing hull) or dramatically more power.

This wave-trapping phenomenon has a direct evolutionary consequence: to achieve higher critical speeds, hulls must be longer. Bejan et al. (2020) showed that the optimal proportions of sailing vessels—specifically the length-to-beam ratio and the relationship between waterline length and displacement—can be derived from the requirement to maximise speed relative to the wave speed limit.

1.2.2 Classification of Ocean Waves

Ocean waves span an enormous range of periods and wavelengths. Dera (1992) classified the continuous spectrum of surface oscillations by period:

- **Capillary waves** ($T \approx 0.1$ s): generated by wind stress on the surface, restored by surface tension.
- **Wind-generated gravity waves**: ultragravity ($T \approx 1$ s), ordinary gravity ($T \approx 10$ s), and infragravity ($T \approx 100$ s). Ordinary gravity waves with $T \approx 10$ s carry the greatest potential and kinetic energy, with average heights of about 1 m and extreme heights exceeding 13 m in strong winds.
- **Long-period waves** ($T \approx 10^3$–10^4 s): generated by storms and earthquakes (including tsunamis).
- **Tidal waves**: ordinary tidal waves ($T \approx 12$ h) and transtidal waves ($T \geq 24$ h), driven by the gravitational attraction of the Moon and Sun.
- **Seiches**: free oscillations of an entire enclosed or semi-enclosed body of water, analogous to the oscillation of water in a bowl (Dera, 1992).

In addition to these surface waves, the ocean supports *internal waves* that propagate at the density interfaces within the water column, particularly the pycnocline. The restoring force for internal waves is the buoyancy associated with the vertical density gradient. Dera (1992) showed that the maximum frequency of internal wave oscillation is the Brunt–Väisälä frequency:
Equation 6.2 — Brunt–Väisälä frequency:

$$N = \sqrt{-\frac{g}{\rho}\frac{\mathrm{d}\rho}{\mathrm{d}z}} \tag{1.2}$$

In the ocean pycnocline, $N_{\max} \approx 10^{-2}$ s^{-1}, corresponding to an oscillation period of approximately 10 min (Cushman-Roisin & Beckers, 2011). The lowest observed Brunt–Väisälä frequencies are of order 10^{-3}–10^{-4} s^{-1} (periods of 1.7–17 h). When the oscillation frequency exceeds N, the wave motion becomes turbulent (Dera, 1992, Eq. 1.2.27).

1.2.3 Wave Generation by Wind

The generation of ocean surface waves by the wind is a complex air–sea interaction problem that was first placed on a rigorous theoretical footing in the 1950s. Two complementary mechanisms—the resonance theory of Phillips and the shear instability theory of Miles—together explain the initial growth and subsequent exponential amplification of the wave field (Gill, 1982; Pierini, 2025).

Pierini (2025) formulates the evolution of the wave power spectrum $\Psi(\mathbf{k}, t)$ through a source function:

Equation 6.3 — Spectral energy evolution:

$$\frac{\partial \Psi(\mathbf{k}, t)}{\partial t} = S(\mathbf{k}, t) \tag{1.3}$$

where S is the source function containing terms for each generation mechanism (Pierini, 2025, Eq. 10.14).

Phillips Resonance Mechanism

The first mechanism, due to Phillips (1957), as presented in Pierini (2025), considers the generation of waves from a perfectly calm sea surface. The onset of wind produces turbulent fluctuations of atmospheric pressure at the surface. A surface wave with wave number $\mathbf{k}$ is excited resonantly by pressure fluctuations whose spatial and temporal scales match those of the wave. The corresponding source function is (Pierini, 2025, Eq. 10.15):

Equation 6.4 — Phillips source function:

$$S_{\text{Phillips}} \propto E_p[\mathbf{k},\ \sigma(\mathbf{k})] \tag{1.4}$$

where $E_p(\mathbf{k}, \sigma)$ is the power spectrum of the turbulent atmospheric surface pressure field (Pierini, 2025). Since S_{Phillips} is independent of the wave energy itself, the solution of Equation 1.3 yields a spectral energy density that grows *linearly* with time: $\Psi \propto t$. This linear growth is slow, producing only a weak initial wave field, but it is essential for providing the seed perturbation upon which the second mechanism can act (Pierini, 2025).

Miles Shear Instability Mechanism

Once a wave field has been established by the Phillips mechanism, a more powerful growth process takes over. Pierini (2025) describes the Miles (1957) mechanism as a positive feedback (instability) of the coupled air–sea system: the existing waves perturb the atmospheric boundary layer, and this perturbation in turn reinforces the waves. The source function is (Pierini, 2025, Eq. 10.16):

Equation 6.5 — Miles source function:

$$S_{\text{Miles}} \propto \Psi(\mathbf{k}, t)\ \frac{1}{z_c(\mathbf{k})} \tag{1.5}$$

where z_c is the *critical height* at which the mean wind speed $U(z_c)$ equals the phase velocity of the wave (Pierini, 2025, Eq. 10.17). In the atmospheric surface layer, the wind profile is logarithmic, $U(z) = (u_*/\kappa)\ln(z/z_0)$, where u_* is the friction velocity, κ is the von Kármán constant, and z_0 is the roughness length (Faltinsen, 1990; Pierini, 2025).

Because S_{Miles} is proportional to the wave energy Ψ itself, the solution of Equation 1.3 is an *exponential* growth: $\Psi \propto e^{t/\tau}$, where τ is a characteristic growth time (Pierini, 2025). This exponential growth is far more rapid than the linear Phillips growth and is the dominant mechanism for building the wave field to its equilibrium state.

Two important consequences follow from Equation 1.5 (Pierini, 2025). First, since $S \propto z_c^{-1}$, a stronger wind produces a lower critical height for a given wave speed, leading to greater energy input and a higher equilibrium wave energy. Second, the stronger the wind, the higher the maximum wave phase velocity that can be generated; since in deep water $\sigma = g/c_p$ (where c_p is the phase velocity), stronger winds shift the spectral peak toward *lower* frequencies and *longer* wavelengths. These generation mechanisms, together with nonlinear wave–wave interactions, continue until a statistical equilibrium is reached in which energy input from the wind balances dissipation by wave breaking and turbulence (Pierini, 2025).

The generation process also depends on the *fetch*—the horizontal distance over which the wind acts on the sea surface. A larger fetch allows waves to accumulate energy over a greater distance, producing a more energetic wave field even far from the generation area (Pierini, 2025).

1.3 Theoretical Framework

1.3.1 Linear Wave Theory (Airy Wave Theory)

Linear wave theory begins with the physics of *simple harmonic motion* (SHM). An oscillator undergoes SHM when the restoring force is proportional to—and directed opposite to—the displacement from equilibrium (Hewitt et al., 2012). Campbell (2025) writes the defining equation of SHM as:

Equation 6.6 — Simple harmonic motion:

$$a(t) = -\omega^2\, x(t) \tag{1.6}$$

where ω is the angular frequency. For a mass–spring system $\omega = \sqrt{k/m}$, while for a simple pendulum $\omega = \sqrt{g/l}$ (Campbell, 2025). The general solution is:

Equation 6.7 — SHM displacement:

$$x(t) = A\sin(\omega t + \phi) + x_0 \tag{1.7}$$

where A is the amplitude, ϕ is the phase shift, and x_0 is the equilibrium position. The angular frequency relates to the oscillation period and linear frequency by $\omega = 2\pi/T = 2\pi f$ (Campbell, 2025).

When a sinusoidal oscillation propagates through a medium, the result is a *traveling wave*. Introducing the wave number $k = 2\pi/\lambda$ (where λ is the wavelength), the displacement at position x and time t is (Campbell, 2025):

Equation 6.8 — Traveling sine wave:

$$y(x,\, t) = A\sin(kx \pm \omega t + \phi) \tag{1.8}$$

The wave propagates at a speed given by the fundamental relation (Campbell, 2025):

Equation 6.9 — Wave speed:

$$v = \frac{\lambda}{T} = \lambda\, f \tag{1.9}$$

For a concise treatment of wave propagation, see (Fischer-Cripps, 2014).

For deep-water ocean gravity waves, linear (Airy) theory gives $v = \sqrt{g\lambda/(2\pi)}$; longer waves travel faster, leading to wave dispersion. The critical hull speed (Equation 1.1) is precisely the speed at which the vessel matches the phase velocity of its own transverse bow wave. For shallow water ($d \ll \lambda$), the phase speed simplifies to $v = \sqrt{gd}$, which is independent of wavelength—hence shallow-water waves are non-dispersive, and tsunami wavefronts maintain their shape over long distances.

Birk (2019) presents the complete mathematical formulation of linear (Airy) wave theory as a boundary value problem (BVP) for the velocity potential $\phi(x, z, t)$ (Newman, 1977), assuming inviscid, incompressible, irrotational flow. The fluid domain V is bounded above by the free surface S_F at $z = \zeta(x, t)$ and below by the ocean bottom S_B at $z = -h$.

Since the flow is irrotational, the velocity field $\mathbf{v} = \nabla\phi$ and mass conservation requires (Birk, 2019):

Equation 6.10 — Laplace equation:

$$\Delta\phi = \frac{\partial^2\phi}{\partial x^2} + \frac{\partial^2\phi}{\partial z^2} = 0 \qquad \text{in } V \tag{1.10}$$

For a rigorous mathematical treatment of Laplace's equation and boundary-value problems, see (Burton & Noble, 2024).

At the impermeable ocean bottom, the vertical velocity must vanish (Birk, 2019):

Equation 6.11 — Bottom boundary condition:

$$\frac{\partial\phi}{\partial z} = 0 \qquad \text{at } z = -h \tag{1.11}$$

Two boundary conditions are needed at the free surface because both the potential ϕ and the wave elevation ζ are unknown. The *kinematic* free surface

condition requires the surface to be a stream surface (no fluid crosses it); the *dynamic* condition requires the pressure at the surface to equal atmospheric pressure. In the exact (nonlinear) formulation, both conditions must be satisfied at the *unknown* surface $z = \zeta(x,t)$ and contain products of the unknown functions, making the problem nonlinear and implicit (Birk, 2019).

Linearisation is achieved through a perturbation expansion with the wave steepness $\varepsilon = H/L_w \ll 1$ as the small parameter. The nonlinear terms vanish at first order, and—critically—the free surface conditions are imposed at the *calm water level* $z = 0$ rather than at the actual surface (Birk, 2019). The linearised kinematic and dynamic free surface conditions are: **Equation 6.12** — Kinematic free surface condition:

$$-\frac{\partial \zeta}{\partial t} + \frac{\partial \phi}{\partial z} = 0 \qquad \text{at } z = 0 \tag{1.12}$$

Equation 6.13 — Dynamic free surface condition:

$$\frac{\partial \phi}{\partial t} + g\,\zeta = 0 \qquad \text{at } z = 0 \tag{1.13}$$

The wave elevation is recovered from the dynamic condition as (Birk, 2019): **Equation 6.14** — Wave elevation recovery:

$$\zeta(x,t) = -\frac{1}{g}\,\frac{\partial \phi}{\partial t}\bigg|_{z=0} \tag{1.14}$$

Eliminating ζ between Equations 1.12 and 1.13 yields the *combined linear free surface boundary condition* (Birk, 2019):

Equation 6.15 — Combined free surface condition:

$$\frac{\partial^2 \phi}{\partial t^2} + g\,\frac{\partial \phi}{\partial z} = 0 \qquad \text{at } z = 0 \tag{1.15}$$

The complete linearised BVP (Birk, 2019) is thus: **Equation 6.16** — Complete linearised boundary-value problem:

$$\boxed{\begin{aligned} &\Delta\phi = 0 && \text{in } V \\ &\phi_{tt} + g\,\phi_z = 0 && \text{at } z = 0 \\ &\phi_z = 0 && \text{at } z = -h \\ &c = \text{const.} \geq 0 && \text{at } |x| \to \infty \end{aligned}} \tag{1.16}$$

The solution is a velocity potential of the form $\phi = f(z)\,\sin(kx - \omega t)$ where $f(z)$ must satisfy the Laplace equation and all boundary conditions. The resulting *dispersion relation* links the angular frequency ω to the wave number k and water depth h (Birk, 2019):

Equation 6.17 — Dispersion relation:

$$\omega^2 = g\,k\,\tanh(kh) \tag{1.17}$$

The phase velocity (celerity) of the wave is $c = \omega/k = \sqrt{(g/k)\,\tanh(kh)}$. In deep water ($kh \gg 1$, i.e. $\tanh(kh) \to 1$), this simplifies to $c = \sqrt{g/(2\pi)}\,\sqrt{\lambda}$— longer waves travel faster, producing dispersion. In shallow water ($kh \ll 1$, i.e. $\tanh(kh) \to kh$), the phase speed is $c = \sqrt{gh}$, independent of wavelength— waves are non-dispersive and tsunami wavefronts maintain their shape (Birk, 2019).

Perturbation Expansion and the Kelvin Wave Pattern

The linearised boundary-value problem underlying Equations 1.10–1.17 is derived rigorously by Timman et al. (1985) through a perturbation expansion in a small parameter ε representing the ratio of wave amplitude to wavelength. By writing the free-surface elevation as $\eta = \varepsilon\bar{\eta}$ and the velocity potential as $\phi = \phi_0 + \varepsilon\phi_1 + \varepsilon^2\phi_2 + \cdots$, where $\phi_0 = Ux$ is the undisturbed uniform stream, the Euler equations and kinematic/dynamic boundary conditions on the unknown free surface are transferred to the undisturbed surface $y = 0$ at each order of ε. At first order the free-surface elevation is recovered from the velocity potential by $\eta_1 = -(1/g)(\phi_{1t} + U\phi_{1x})|_{y=0}$, and the combined free-surface condition becomes (Timman et al., 1985):

Equation 6.18 — Linearised free-surface condition with forward speed:

$$\phi_{1tt} + 2U\,\phi_{1xt} + U^2\,\phi_{1xx} + g\,\phi_{1y} = 0 \quad \text{at } y = 0 \tag{1.18}$$

For steady flow ($\partial/\partial t = 0$) past a pressure disturbance at the origin, this reduces to $U^2\phi_{xx} + g\phi_y = 0$. Timman et al. (1985) solve this problem by Fourier transform and evaluate the surface elevation for large distances using the method of stationary phase. The resulting wave pattern is defined parametrically by the locus of constant phase:

Equation 6.19 — Kelvin wave pattern (parametric form):

$$x = -\psi\,(2\cos\alpha - \cos^3\alpha), \qquad z = -\psi\,\cos^2\alpha\,\sin\alpha \tag{1.19}$$

where ψ is the phase parameter and α is a parametric angle. The curves are similar about the origin, with cusps lying on straight lines at a fixed half-angle $\theta_K = \arctan(1/\sqrt{8}) \approx 19.47^\circ$ from the vessel's track. Inside this angle, the pattern comprises *transverse waves* (nearly perpendicular to the track) and *divergent waves* (radiating outward from the bow), both systems intersecting at the cusp line (Timman et al., 1985). The hull-speed concept of Equation 1.1 is a direct consequence: when the vessel speed U equals $\sqrt{gL/(2\pi)}$, the transverse wavelength matches the waterline length, and the wave system demands a disproportionate fraction of the propulsive power.

Timman et al. (1985) further establish that the group velocity $c_G = \mathrm{d}\omega/\mathrm{d}k$ (Equation 1.25) has a precise physical interpretation as the propagation speed

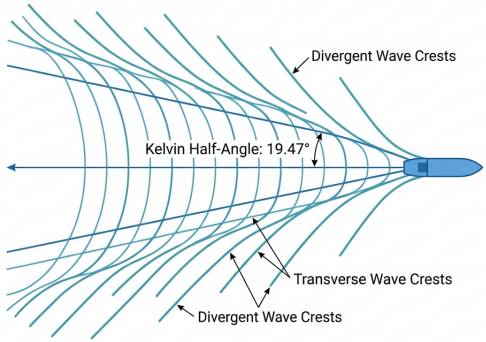

Figure 1.1: Plan view of the Kelvin wave pattern generated by a vessel moving to the right at constant speed U. The transverse wave crests (nearly perpendicular to the track) and divergent wave crests (radiating outward) are confined within cusp lines at a universal half-angle $\theta_K = \arctan(1/\sqrt{8}) \approx 19.47^\circ$, independent of vessel speed (Equation 1.19). The wavelength of the transverse system increases with speed; at the hull speed V_c (Equation 1.1), the transverse wavelength equals the waterline length and the wave resistance rises sharply (Timman et al., 1985).

of the centre of gravity of wave energy. By representing the surface elevation as a Fourier integral $\eta(x,t) = \int A(k)\, e^{i(\omega t - kx)}\, \mathrm{d}k$ and computing the first moment of the energy density $|\eta|^2$, they show that the centroid of the energy distribution propagates at exactly the mean group velocity $\mathrm{d}\omega/\mathrm{d}k$, weighted by the spectral energy $|A(k)|^2$. For a narrow-band spectrum centred at wave number k_0, the wave amplitude envelope travels at $c_G(k_0)$ while individual crests move at the phase velocity $\omega(k_0)/k_0$—the familiar beating pattern of a modulated wave group (Timman et al., 1985).

1.3.2 Deep Water and Shallow Water Approximations

In shallow water, a fundamentally different class of wave phenomena arises: bores. A bore is a translating front of elevated water that propagates into a region of lower water depth under the action of gravity. Bores occur naturally in tidal rivers (tidal bores), in tsunami propagation, and in the interaction of breaking waves with coastal structures.

Hernández-Fontes et al. (2020) investigated the physics of bores generated by the wet dam-break method, in which a vertical gate separates two bodies of calm water at different levels. When the gate is removed, the higher upstream volume (h_1) drives a bore into the lower downstream volume (h_0). The theoretical framework for this bore formation was established by Stoker (1957), as cited in Hernández-Fontes et al. (2020), assuming infinite propagation domains on both sides of the gate.

In the experiments of Hernández-Fontes et al. (2020), four wet dam-break ratios $r_d = h_0/h_1 = 0.7$, 0.6, 0.5, and 0.4 were tested. As the upstream-to-downstream depth ratio decreased (lower r_d), the initial potential energy difference increased, producing bores of greater height. The measured bore heights overestimated the infinite-domain theoretical values by approximately 10–16%, attributed to the finite propagation distance (0.505 m from gate to structure) and the presence of a downstream structure (Hernández-Fontes et al., 2020).

Solitary Wave Characterisation of Bores

Hernández-Fontes et al. (2020) characterised the resulting bores as solitary waves, following the approach of earlier researchers who adopted this approximation for gravity-collapse-generated flows. For a solitary wave, the two governing parameters are the wave height and the constant water depth at which it propagates. In the wet dam-break context, these correspond to the non-dimensional bore height $h_w^* = h_w/h_1$ and the downstream depth $h_0^* = h_0/h_1$, respectively.

A characteristic length for the bore is required to define its steepness. For non-periodic wave shapes, no single length describes the entire wave accurately (Hernández-Fontes et al., 2020). Based on solitary wave theory, the characteristic length of the bores was estimated as:

Equation 6.20 — Characteristic bore length (solitary wave approximation):

$$L_c^* = 1.5 \left(\frac{h_w^*}{h_0^*} \right)^{-1/2} h_0^* \tag{1.20}$$

The bore steepness is then defined as:

Equation 6.21 — Bore steepness:

$$\varepsilon = \frac{h_w^*}{L_c^*} \tag{1.21}$$

For the four experimental cases in Hernández-Fontes et al. (2020), considering experiments without the structure, the steepness values were $\varepsilon \approx 0.12$, 0.21, 0.33, and 0.55 for wet dam-break ratios of 0.7, 0.6, 0.5, and 0.4, respectively. This range of steepness produced fundamentally different behaviours when the bores interacted with a downstream structure (see the discussion of bore–structure interaction in the *Ship Motions and Seakeeping* chapter of the companion volume).

The bore height h_w^* increased from case C1 to C4 (i.e., from higher to lower dam-break ratios). For C2, C3, and C4, the non-dimensional bore heights were approximately 1.2, 1.4, and 1.6 times the value obtained for C1, respectively (Hernández-Fontes et al., 2020). These increases were associated with steeper rising limbs in the water elevation time series, reflecting a faster transfer of potential energy into kinetic energy in the bore front.

1.3.3 Wave Energy and Power

Ocean waves contain both kinetic and potential energy. Birk (2019) derives both components rigorously within the linear wave theory framework.

The *kinetic energy* in a control volume spanning one wavelength L_w, width b, and depth h is obtained by integrating the velocity magnitude over the fluid domain. Using the velocity components from the Airy wave potential and the identity $\cosh^2\alpha\cos^2\theta + \sinh^2\alpha\sin^2\theta = \frac{1}{2}[\cosh(2\alpha)+\cos(2\theta)]$, the integration simplifies. The $\cos(2kx - 2\omega t)$ term integrates to zero over a full wavelength, and the dispersion relation $\omega^2 = gk\tanh(kh)$ reduces the remaining hyperbolic expression, yielding (Birk, 2019): **Equation 6.22** — Kinetic energy over one wavelength:

$$E_{\text{kin}} = \tfrac{1}{4}\,\rho\,g\,\zeta_a^2\,b\,L_w \tag{1.22}$$

The *potential energy* is the work done in lifting or depressing fluid elements above or below the calm water level. Integrating the potential energy $\mathrm{d}E_{\text{pot}} = \frac{1}{2}\rho g b\,\zeta^2\,\mathrm{d}x$ over one wavelength gives (Birk, 2019): **Equation 6.23** — Potential energy over one wavelength:

$$E_{\text{pot}} = \tfrac{1}{4}\,\rho\,g\,\zeta_a^2\,b\,L_w \tag{1.23}$$

A remarkable result: kinetic and potential energy are exactly equal in linear wave theory. The *total wave energy density* (energy per unit ocean surface area) is (Birk, 2019):

Equation 6.24 — Total wave energy density:

$$E = E_{\text{kin}} + E_{\text{pot}} = \tfrac{1}{2}\,\rho\,g\,\zeta_a^2 \tag{1.24}$$

The energy density depends only on the wave amplitude squared and is independent of water depth and wave frequency (Birk, 2019). This has important consequences: doubling the wave amplitude quadruples the energy density, explaining why storm waves carry disproportionately more energy.

The rate at which wave energy propagates is characterised by the *group velocity* (Birk, 2019):

Equation 6.25 — Group velocity:

$$c_G = \frac{c}{2}\left[1 + \frac{2kh}{\sinh(2kh)}\right] \tag{1.25}$$

where $c = \omega/k$ is the phase velocity. In deep water ($kh \gg 1$), $c_G = c/2$—wave energy propagates at half the phase speed. In shallow water ($kh \ll 1$), $c_G = c$—energy and phase travel at the same speed (Birk, 2019). The group velocity governs the arrival time of swell energy from distant storms and determines the rate at which wave conditions build in a towing tank (Birk, 2019).

The sinusoidal profile described by Equation 1.8 is a first-order approximation. Real ocean waves have crests that are sharper and troughs that are

broader than a pure sine wave. The simplest nonlinear profile used in classical naval architecture is the *trochoidal wave*, formed by a point at distance r from the centre of a circle of radius R rolling steadily along a horizontal line (Attwood, 1917).

For a trochoidal wave of length L and height h, the rolling circle has radius $R = L/(2\pi)$ and the tracing radius is $r = h/2$. The parametric equations of the surface profile are (Attwood, 1917):

Equation 6.26 — Trochoidal wave profile:

$$\begin{aligned} x &= \frac{L}{2\pi}\,\theta - \frac{h}{2}\,\sin\theta \\ y &= \frac{h}{2}\,\cos\theta \end{aligned} \tag{1.26}$$

where θ is the angle turned through by the rolling circle, x is the horizontal coordinate, and y is the vertical coordinate measured from the mean water level (Attwood, 1917). When $h \to 0$ (i.e. $r \to 0$), the trochoid degenerates into a straight line; as $h \to L/\pi$ (i.e. $r \to R$), the trochoid becomes a cycloid with cusps at its crests, representing the theoretical maximum steepness.

For structural loading calculations, Attwood (1917) adopted the standard assumption $h = L/20$—that is, a wave height equal to one-twentieth of the wavelength. A ship is then poised on this trochoidal wave with the crest amidships (hogging condition) or the trough amidships (sagging condition), and the buoyancy distribution recalculated to obtain the curves of loads, shearing force, and bending moment (see Chapter 5, Section 5.3.2) (Attwood, 1917). The trochoidal profile concentrates more volume near the crest and less near the trough than a sinusoidal wave of the same height and length, producing a more severe hogging condition and a somewhat less severe sagging condition.

Rawson and Tupper (2001) extend these results to the sub-surface kinematics. The orbital radius at depth d beneath a trochoidal wave decays exponentially:

$$r_d = r\,e^{-2\pi d/\lambda}$$

where $r = h/2$ is the surface orbital radius. At a depth of $\lambda/2$, the motions are negligible; at $\lambda/9$ the orbital diameter is approximately halved. The deep-water phase velocity is $c = \sqrt{g\lambda/(2\pi)}$ and the period is $T = \sqrt{2\pi\lambda/g}$ (Rawson & Tupper, 2001). For a 100 m wavelength, this gives a speed of approximately 12.5 m/s and a period of approximately 8 s. Rawson and Tupper (2001) note that surfaces of equal pressure beneath the trochoidal surface are themselves trochoidal, with the same wavelength but decreasing amplitude—a result that bears directly on the pressure distribution on a submerged hull.

While the trochoidal and linear theories are adequate for many engineering purposes, higher-order wave theories are required when the wave steepness ak is not negligible or when depth effects introduce important nonlinearities.

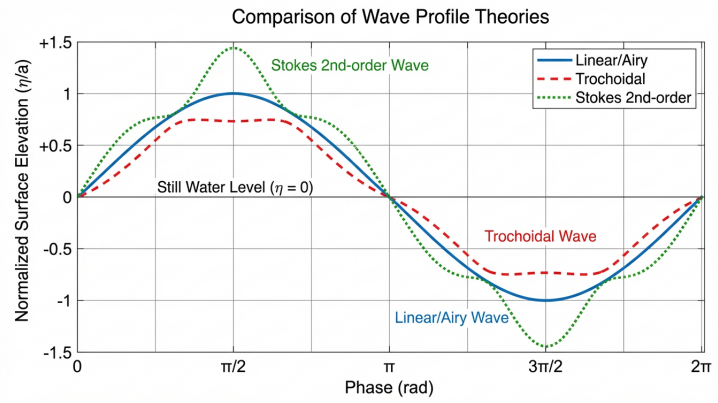

Figure 1.2: Comparison of surface wave profiles predicted by linear, trochoidal, and Stokes second-order theories for the same wave height H and wavelength λ. The linear (Airy) profile is purely sinusoidal (Equation 1.8). The trochoidal profile (Equation 1.26) exhibits sharper crests and broader troughs. The Stokes second-order profile (Equation 1.27) further sharpens the crest and flattens the trough due to the $\cos(2\theta)$ harmonic. The deviation from the sinusoidal profile increases with wave steepness ak (Attwood, 1917; Pierini, 2025).

Stokes Waves (Deep Water)

Beyond the trochoidal approximation, a systematic perturbation theory for nonlinear waves was developed by Stokes (1847), as presented in Pierini (2025). The nonlinear terms $(\mathbf{u} \cdot \nabla)\mathbf{u}$ in the Navier–Stokes equations introduce an amplitude dependence into both the wave profile and the dispersion relation. In deep water ($kD \gg 1$), the surface elevation of a Stokes wave is (Pierini, 2025, Eq. 9.33):

Equation 6.27 — Stokes wave profile (deep water):

$$\eta = a\cos\theta + a^2\,\chi\,\cos(2\theta) + \cdots \tag{1.27}$$

where $\theta = kx - \sigma t$, a is the wave amplitude, and the second-order coefficient χ depends on the water depth (Pierini, 2025, Eq. 9.34): **Equation 6.28** — Stokes second-order coefficient:

$$\chi = \tfrac{1}{2}\,k\,\coth(kD)\left[1 + \frac{3}{2\sinh^2(kD)}\right] \tag{1.28}$$

The second harmonic $\cos(2\theta)$ produces the distinctive asymmetry of nonlinear waves: crests become narrower and higher than the linear prediction ($\eta_{\max} > a$), while troughs become wider and shallower ($|\eta_{\min}| < a$). This asymmetry increases with wave steepness (Pierini, 2025).

The dispersion relation also acquires an amplitude dependence. In deep water, the linear relation $\sigma^2 = gk$ generalises to (Pierini, 2025, Eq. 9.35):

Equation 6.29 — Stokes dispersion relation (deep water):

$$\sigma^2 = gk\left(1 + a^2k^2 + \cdots\right) \tag{1.29}$$

This amplitude dependence is a hallmark of all nonlinear wave fields: steeper waves propagate faster than predicted by linear theory (Pierini, 2025). The second-order correction a^2k^2 becomes significant when the wave steepness ak is not negligible, which is precisely the regime where linear Airy theory (Equation 1.17) begins to lose accuracy.

An important nonlinear effect is the *Stokes drift*: in waves of finite amplitude, the orbital paths of fluid particles do not close exactly, resulting in a net mass transport in the direction of wave propagation. The depth-dependent mean drift velocity is (Pierini, 2025, Eq. 9.36):

Equation 6.30 — Stokes drift velocity:

$$\bar{u}_{\text{SD}} = c_p\, a^2k^2\, e^{2kz} \tag{1.30}$$

where $c_p = \sigma/k$ is the phase velocity. The Stokes drift is maximum at the surface and decays exponentially with depth. It contributes to the transport of floating debris, oil slicks, and biological material, and must be accounted for in search-and-rescue drift predictions (Pierini, 2025).

Cnoidal Waves (Shallow Water)

In shallow water ($kD \ll 1$), the nonlinear wave profile takes a different form. Pierini (2025) shows that the surface elevation of a periodic nonlinear shallow-water wave is (Pierini, 2025, Eq. 9.37):

Equation 6.31 — Cnoidal wave profile (shallow water):

$$\eta = a\cos\theta + \frac{3a^2}{4k^2D^3}\cos(2\theta) + \frac{27a^3}{64k^4D^6}\cos(3\theta) + \cdots \tag{1.31}$$

These waves are called *cnoidal waves* because they can be expressed exactly using the Jacobi elliptic function $\mathrm{cn}(\cdot)$ (Pierini, 2025). The corresponding dispersion relation generalises the shallow-water result as (Pierini, 2025, Eq. 9.38): **Equation 6.32** — Cnoidal wave dispersion relation:

$$\sigma = c_0\, k\left(1 - \tfrac{1}{6}\,k^2D^2 + \tfrac{9a^2}{16k^2D^4} + \cdots\right) \tag{1.32}$$

where $c_0 = \sqrt{gD}$ is the linear shallow-water wave speed. The first correction term $-k^2D^2/6$ introduces weak phase dispersion (longer waves travel slightly faster), while the second correction $9a^2/(16k^2D^4)$ is the nonlinear amplitude correction (Pierini, 2025).

The relative importance of nonlinearity is measured by the *Ursell number* (Pierini, 2025, Eq. 9.42):

Equation 6.33 — Ursell number:

$$\mathrm{Ur} = \frac{a\,\lambda^2}{D^3} \tag{1.33}$$

where λ is the wavelength and D is the water depth. When Ur $\gg 1$, nonlinear effects dominate and the cnoidal or solitary wave description is appropriate; when Ur $\ll 1$, linear Airy theory is adequate. The Ursell number thus provides a practical criterion for selecting the appropriate wave theory for a given water depth and wave condition (Pierini, 2025). This is particularly relevant for coastal engineering applications, where waves approaching the shore enter progressively shallower water and the transition from linear to nonlinear behaviour must be identified.

Weakly Nonlinear Wave Group Dynamics

The linear superposition model (Equation 1.8) predicts that individual wave components propagate independently, so that any wave group envelope disperses and changes shape during propagation. In reality, nonlinear interactions among components modify the evolution of wave groups, leading to phenomena such as modulational instability and rogue wave formation. The classical *nonlinear Schrödinger equation* (NLSE) captures these leading-order effects by extending the perturbation expansion of the water wave boundary value problem (Equations 1.10–1.15) to third order in wave steepness (Klein et al., 2021).

The NLSE derivation requires two small parameters: the wave steepness $\epsilon = k_c\,\zeta_a$ and the relative bandwidth $\mu = \Delta k/k_c \ll 1$, where k_c is the carrier wave number and ζ_a the wave amplitude (Klein et al., 2021). Taylor series expansion about the still water level and sequential solution at each order $\mathcal{O}(\epsilon^n)$ up to $n = 3$ yields the NLSE for the complex envelope A of a time series evolving in space (Klein et al., 2021):

Equation 6.34 — Nonlinear Schrödinger equation (spatial evolution form):

$$\frac{\partial A}{\partial x} + \frac{1}{C_g}\,\frac{\partial A}{\partial t} + i\left(\alpha'\,\frac{\partial^2 A}{\partial t^2} + \beta'\,|A|^2\,A\right) = 0 \tag{1.34}$$

where $C_g = (\omega_c/2k_c)\,\nu$ is the group velocity with the finite-depth correction $\nu = 1 + 2k_cd/\sinh(2k_cd)$, d is the water depth, ω_c the carrier angular frequency, and the dispersive coefficient α' and nonlinear coefficient β' depend on ω_c, k_c, and d (Klein et al., 2021). The second term represents advection at the group velocity, the α'-term governs linear dispersive spreading of the envelope, and the β'-term captures cubic nonlinear self-interaction. In deep water ($k_cd \gg 1$), the product $\alpha'\beta' > 0$, which makes the NLSE *focussing*: dispersive and nonlinear effects can balance exactly, giving rise to stable localised wave groups (Klein et al., 2021).

One such localised solution is the *envelope soliton*, an exact solution of Equation (1.34) in which dispersion and nonlinearity are perfectly balanced so that the wave group propagates with permanent form. Its surface elevation is (Klein et al., 2021):

Equation 6.35 — Envelope soliton surface elevation:

$$\zeta_{\mathrm{ES}}(x,t) = \frac{a_c}{\cosh\left[a_c\sqrt{\frac{\beta'}{2\alpha'}}\left(t-\frac{x}{C_g}\right)\right]}\cos(k_c\,x-\omega_c\,t+\phi_s) \tag{1.35}$$

where a_c is the soliton amplitude and ϕ_s is the carrier wave phase (Klein et al., 2021). The hyperbolic secant envelope determines the wave group width: with increasing amplitude the group becomes narrower and steeper, in contrast to linear design wave profiles where the shape is independent of the wave height. Soliton-like wave groups have been shown to persist in unidirectional irregular sea states for more than 200 wave periods, increasing the probability of extreme wave heights even in moderately rough conditions (Klein et al., 2021).

A distinct class of exact NLSE solutions are the *breather solutions*, which describe extreme wave events driven by modulational instability. The *Peregrine breather*—localised in both time and space—represents a wave that "appears from nowhere and disappears without trace" (Klein et al., 2021). At the point of maximum focussing, the Peregrine breather reaches an amplitude amplification factor (AAF) of exactly three (Klein et al., 2021):

Equation 6.36 — Peregrine breather maximum amplification:

$$\zeta_{\mathrm{max}} = 3\,a_c \tag{1.36}$$

This threefold amplification is independent of carrier frequency and steepness. The resulting extreme wave profiles share many characteristics with observed rogue waves, most notably the New Year Wave recorded at the Draupner platform on 1 January 1995 (Klein et al., 2021). The similarity establishes modulational instability as a viable physical mechanism for deep-water rogue wave formation.

1.3.4 Wave Refraction, Diffraction, and Reflection

When waves enter a semi-enclosed basin such as a harbour or fjord, reflections from the basin boundaries produce standing oscillation patterns known as *harbour oscillations* or *seiches*. The natural (resonant) frequencies and associated modal shapes of these oscillations are fundamental properties of the basin, determined by its geometry, size, and internal bathymetry (Zheng et al., 2022).

Zheng et al. (2022) investigated harbour oscillations excited by seismic ground motion using a fully nonlinear Boussinesq wave model. In this framework, the coordinate system is fixed to the harbour, and the seismic ground motion introduces horizontal inertial acceleration terms $\mathbf{a}' = (a_x,\, a_y)$ and a vertical acceleration a_z into the Boussinesq momentum equation. The effective gravitational acceleration becomes $(g - a_z)$, while the horizontal inertial accelerations appear as additional body force terms driving wave generation within the basin. The resulting wave fields are three-dimensional

and multi-modal even when the seismic excitation is uni-directional and simple harmonic, because of reflections against the complicated boundaries of the harbour (Zheng et al., 2022).

The coupling between the depth-averaged Boussinesq wave model and a three-dimensional panel model for ship motion analysis requires the wave motions to satisfy the linearisation criterion (Zheng et al., 2022):

Equation 6.37 — Linearisation validity criterion for long waves:

$$\frac{kA}{\tanh kh} \ll 1 \tag{1.37}$$

where A is the wave amplitude, k the wavenumber, and h the water depth.

The seismic excitation of harbour oscillations differs fundamentally from excitation by incident waves from the open sea. The oscillating quay walls act as a piston-type wavemaker, and breakwaters—which are effective barriers against incoming ocean waves—provide no protection because the excitation originates within the basin itself (Zheng et al., 2022). Seismic excitation can therefore trigger natural modes that cannot be excited by steady incident waves or transient tsunamis.

For Hambantota Port (Sri Lanka), Zheng et al. (2022) determined that seismic excitation with a period of 5 s and a peak ground acceleration of $0.6\,\mathrm{m\,s^{-2}}$ triggers multiple natural modes simultaneously, with periods ranging from approximately 24 s (high-order sloshing modes between parallel quay walls) to 1333 s (the lowest pumping mode featuring strong oscillatory currents at the harbour entrance). The modal shapes are spatially variable: the lowest mode features a vertical rise and fall of the water surface in unison throughout the harbour, while higher-order modes exhibit nodal lines that divide the basin into regions oscillating in antiphase (Zheng et al., 2022). The direction of seismic excitation governs which modes dominate: excitation perpendicular to the quay walls drives violent high-order modes, while excitation directed from the harbour end toward the entrance generates weaker oscillations governed by low-order modes (Zheng et al., 2022).

The real-world significance of seismic-induced harbour oscillations was demonstrated during the 2011 Tōhoku Earthquake. A VLCC (333×60 m) moored in a Japanese harbour experienced long-period (~ 100 s) sway movements of approximately 10 m, resulting in damage to the ship and mooring system. Seismic waves from the same event propagated over 8000 km and triggered free-surface oscillations in Norwegian fjords, forcing boats to oscillate periodically (Zheng et al., 2022).

1.3.5 Wave Spectra and Statistical Description

Real ocean waves are not periodic; they result from many independent wave components superimposed with different amplitudes, frequencies, and propagation directions. The statistical description of such a wave field is

achieved through the wave energy spectrum $S(\omega)$, which describes the distribution of wave energy over angular frequency ω. Zhang et al. (2025) adopt the general *Bretschneider spectral form*, in which the wave energy spectrum takes the shape:

Equation 6.38 — Bretschneider spectral form:

$$S(\omega) = \frac{A}{\omega^5} \exp\left(-\frac{B}{\omega^4}\right) \tag{1.38}$$

where A and B are coefficients that determine the spectral shape (Zhang et al., 2025). This form was established by Bretschneider (1959), as cited in Zhang et al. (2025), and serves as the basis for several standard spectral models.

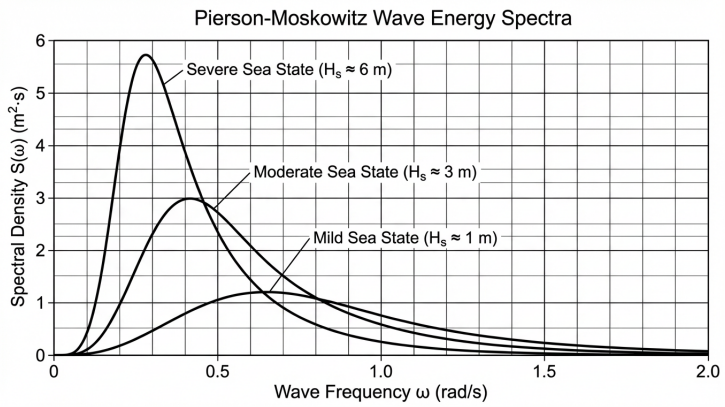

Figure 1.3: Pierson–Moskowitz wave energy spectrum $S(\omega)$ for three sea states with significant wave heights $H_{1/3} = 2\,\text{m}$, $4\,\text{m}$, and $6\,\text{m}$ (Equations 1.38–1.39). As $H_{1/3}$ increases, the spectral peak shifts toward lower frequencies (longer waves) and the total spectral energy (area under the curve) grows as $H_{1/3}^2$. The characteristic ω^{-5} high-frequency tail and exponential cut-off are visible in all three curves (Zhang et al., 2025).

For fully developed wind seas, the two-parameter *Pierson–Moskowitz spectrum* (Talley et al., 2011), recommended by the 15th International Towing Tank Conference (1978) as cited in Zhang et al. (2025), specifies the coefficients A and B in terms of the significant wave height $H_{1/3}$ and the mean wave period T_1:

Equation 6.39 — Pierson–Moskowitz spectrum parameters:

$$A = \frac{173\,H_{1/3}^2}{T_1^4}, \qquad B = \frac{691}{T_1^4} \tag{1.39}$$

where $H_{1/3}$ is the significant wave height in metres and T_1 the mean wave period in seconds (Zhang et al., 2025). The significant wave height $H_{1/3}$ is defined as the average of the highest one-third of wave heights in a record and serves as the single most important parameter characterising the severity

of a sea state. The Pierson–Moskowitz spectrum thus requires only two observable quantities—wave height and period—to specify the complete energy distribution across all frequencies.

Real seas are not long-crested (i.e. the energy does not propagate in a single direction). To describe the directional distribution of wave energy, a *spreading function* $D(\mu)$ distributes the total spectral energy among the various propagation directions μ measured relative to the primary wave direction. Zhang et al. (2025) adopt the cosine power form:

Equation 6.40 — Directional spreading function:

$$D(\mu) = \begin{cases} \dfrac{2^{2n-1}\, n!\,(n-1)!}{\pi\,(2n-1)!}\,\cos^{2n}\mu & \text{for } -\dfrac{\pi}{2} \le \mu \le \dfrac{\pi}{2} \\ 0 & \text{otherwise} \end{cases} \tag{1.40}$$

where n is a positive integer governing the degree of directional spreading (Zhang et al., 2025). Large values of n concentrate the wave energy near the primary propagation direction (narrow spreading), while small values produce a broad directional distribution. This form satisfies the normalisation condition $\int_{-\pi/2}^{\pi/2} D(\mu)\,\mathrm{d}\mu = 1$, so that the omnidirectional spectrum is recovered by integration over all directions.

The *short-crested wave spectrum* is then defined as $S(\omega,\mu) = S(\omega)\,D(\mu)$ (Zhang et al., 2025). A practical realisation of the short-crested irregular sea is obtained by superimposing $N \times M$ independent regular wave components, comprising N angular frequencies at interval $\delta\omega$ and M propagation directions at interval $\delta\mu$, each with amplitude determined by the directional spectrum (Zhang et al., 2025):

Equation 6.41 — Short-crested irregular wave surface:

$$\zeta_w(x_w, y_w, t) = \sum_{i=1}^{N}\sum_{j=1}^{M} \sqrt{2\,S(\omega_i)\,D(\mu_j)\,\delta\omega\,\delta\mu} \times \cos\left[\frac{\omega_i^2}{g}\left(\cos\mu_j\, x_w + \sin\mu_j\, y_w\right) - \omega_i\, t + \varepsilon_{ij}\right] \tag{1.41}$$

where ω_i is the angular frequency of the ith component, μ_j the propagation direction of the jth component, g the gravitational acceleration, and ε_{ij} a random phase uniformly distributed on $[0, 2\pi)$ (Zhang et al., 2025). The deep-water dispersion relation $k = \omega^2/g$ (Equation 1.17 in the limit $kh \gg 1$) has been used to express the wave number in terms of angular frequency. Equation (1.41) provides a computationally realisable representation of a random sea surface: by choosing N and M sufficiently large, the simulated wave field reproduces the target spectrum and spreading characteristics to any desired statistical accuracy (Zhang et al., 2025).

1.3.6 Wave Statistics and Extreme Values

The statistical description of the wave climate at a given site requires long-term records of the significant wave height H_s. Guedes Soares and Santos (2015) analysed a 41-year wave hindcast database generated by the WAM spectral wave model under the HIPOCAS project for the Black Sea. The analysis revealed that 50-year return period significant wave heights in the western Black Sea reach $H_s \approx 10.9\,\text{m}$, while in the eastern region values are lower ($H_s \approx 7.0\,\text{m}$), consistent with the stronger storm activity in the western basin (Guedes Soares & Santos, 2015).

Reliable extreme value estimation requires the identification and removal of outliers from hindcast datasets. Guedes Soares and Santos (2015) applied the classical boxplot method of Tukey to daily maximum H_s data from 15 offshore sites along the Portuguese coast (HIPOCAS, 1958–1978). The inter-quartile range (IQR) is defined as:

Equation 6.42 — Inter-quartile range:

$$\text{IQR} = q_{0.75} - q_{0.25} \tag{1.42}$$

where $q_{0.25}$ and $q_{0.75}$ are the first and third quartiles. The upper and lower outer fences are then placed at $q_{0.75} + 3 \times \text{IQR}$ and $q_{0.25} - 3 \times \text{IQR}$, respectively. Observations beyond these fences are classified as extreme outliers (Guedes Soares & Santos, 2015). For a standard normal distribution, the inner fences ($\pm 1.5 \times$ IQR) correspond to ± 2.698, meaning that 99.3% of the population lies within them and the probability of an observation being flagged as a mild outlier is only 0.7% (Guedes Soares & Santos, 2015).

The removal of extreme outliers was shown to alter the composition of homogeneous sub-regions formed during Regional Frequency Analysis and to affect the 100-year return period extreme quantiles, demonstrating the sensitivity of extreme value predictions to data quality (Guedes Soares & Santos, 2015).

1.4 Applications in Maritime Systems

1.4.1 Wave Loads on Ships and Offshore Structures

The spectral description of ocean waves (Section 1.3.5) enables the prediction of wave-induced structural loads. Under the standard model of ocean wave loading, the irregular sea surface is decomposed into harmonic wave components (Equation 1.8), and the structural response to each component is obtained from a transfer function—the response amplitude operator (RAO). The response spectrum is then $S_S(\omega) = |H(\omega)|^2\, S_\zeta(\omega)$, relating the wave energy spectrum S_ζ to the response energy spectrum S_S through the squared modulus of the RAO (see the *Ship Motions and Seakeeping* chapter of the companion volume) (Klein et al., 2021). This spectral approach enables efficient evaluation of any linear response quantity—motions, accelerations, or global

structural loads—across the full frequency range of a given sea state (Klein et al., 2021).

The design of ships and offshore structures requires identification of the short-duration wave events that produce the most critical structural response. Klein et al. (2021) describe two principal design wave concepts based on the spectral framework. The *Critical Wave Episode* (CWE) concept generates a large number of random sea-state realisations from the product of the wave spectrum and the RAO, and extracts the wave group that produces the highest response. The *Most Likely Response Wave* (MLRW) concept conditions the amplitudes and phases of the wave components to produce the most probable wave profile corresponding to a specified extreme response level. The MLRW surface elevation takes the form (Klein et al., 2021):

Equation 6.43 — Most Likely Response Wave:

$$\zeta_{\text{MLRW}}(x,t) = \sum_{j=1}^{N} \zeta_{a_j} \left[V_j \, \cos(k_j \, x - \omega_j \, t) + W_j \, \sin(k_j \, x - \omega_j \, t) \right] \tag{1.43}$$

where ζ_{a_j} is the amplitude of the jth wave component, k_j its wave number, ω_j its angular frequency, and the conditioning coefficients V_j and W_j are functions of the spectral moments of the response spectrum and a prescribed target response level M_c (Klein et al., 2021). The shape and width of the MLRW depend on the sea state parameters and the RAO, while the absolute values scale linearly with M_c, enabling rapid evaluation of multiple response levels from a single calculation (Klein et al., 2021).

A fundamental limitation of these linear design wave concepts is that the resulting wave profiles can exceed physical limits. Klein et al. (2021) demonstrated this for the vertical wave bending moment of a chemical tanker ($L_{pp} = 161$ m, $C_B = 0.75$): the most critical CWE yielded a wave steepness $\epsilon = Hk/2 \approx 0.52$, which exceeds the theoretical breaking limit. In nature, wave steepness rarely surpasses $\epsilon \approx 0.4$ because of wave breaking (Klein et al., 2021). Even the MLRW for the ultimate hull girder bending capacity reached $\epsilon \approx 0.39$—near the physical bound. Reproducing such steep wave profiles in physical model tests is therefore difficult, since the linear superposition model does not account for the nonlinear interactions within steep wave groups (Klein et al., 2021).

The envelope soliton solutions (Equation 1.35) provide a physically valid alternative. Because the soliton balances dispersion and nonlinearity exactly, it produces steep but inherently stable wave groups. Model tests by Klein et al. (2021) showed that the extreme vertical bending moment produced by envelope solitons at steepness $\epsilon = 0.35$ differed by less than 4% from that produced by a Peregrine breather at the breaking limit for the same carrier wave length. The wave length to ship length ratio L_w/L_{pp} in the range 1.1–1.5 was identified as most critical for the vertical bending moment response. The permissible vertical wave bending moment in sagging was $M_{VW\text{-}S} = -1.25 \times 10^6$ kN m and the ultimate hull girder capacity was $M_{VW\text{-}S\text{-}U} = -1.51 \times 10^6$ kN m; en-

velope solitons at the highest steepness approached or exceeded the permissible limit, confirming their relevance as design waves for extreme response investigations (Klein et al., 2021).

The short duration of envelope soliton wave groups offers practical advantages: in wave tank experiments the calm-down time between successive test runs is significantly reduced compared to irregular sea-state tests, and for numerical simulations the compact wave group requires a shorter simulation domain, reducing computational cost while maintaining full nonlinear fidelity (Klein et al., 2021).

1.4.2 Wave Forecasting and Hindcasting

The planning of marine operations—such as the installation of offshore wind turbines or the maintenance of wave energy converters—requires knowledge of weather windows: periods during which the significant wave height remains below a specified threshold h_{ac}.

Guedes Soares and Santos (2015) derived a probabilistic framework for waiting time estimation. If n consecutive wave height observations all remain below h_{ac}, the probability that the maximum of these observations exceeds the threshold is:

Equation 6.44 — Exceedance probability:

$$P(H_{\max} > h_{ac}) = 1 - \left[F(h_{ac})\right]^n \tag{1.44}$$

where $F(h_{ac})$ is the cumulative distribution of H_s (Guedes Soares & Santos, 2015). When $H_{\max}$ exceeds h_{ac}, an unfavourable condition begins. The expected number of consecutive observations above the threshold before an accessible condition resumes follows a geometric distribution, giving an average waiting time in days:

Equation 6.45 — Average waiting time:

$$T_{aw} = \frac{E(K)}{8} \tag{1.45}$$

where $E(K) = 1/G$, $G = 1 - [F(h_{ac})]^n$, and the factor of 8 converts from 3-hourly observation intervals to days (Guedes Soares & Santos, 2015).

Six probability distributions—Generalised Extreme Value (GEV), three-parameter log-normal (LN3), Gumbel, three-parameter Weibull, Gamma, and Generalised Pareto (GP3)—were fitted to winter-season H_s data off Portugal using the method of L-moments. Goodness of fit was assessed by the Z-test at the 95% confidence level ($|Z| \leq 1.96$), with the Gumbel distribution providing the most consistent fit across both decadal samples (Guedes Soares & Santos, 2015).

1.5 Discussion

The critical velocity concept (Equation 1.1) from Bejan et al. (2020) provides a direct link between wave physics and ship design. The transverse bow wave is not merely a curiosity of wave mechanics; it is the single most important constraint on the speed of displacement vessels. Every naval architect designs with this limit in mind, and the concept of the speed–length ratio $V/\sqrt{L}$ (equivalent to the Froude number) is central to resistance prediction, hull form optimisation, and powering calculations.

The wave-trapping phenomenon also illustrates a general principle of wave–structure interaction: when the characteristic length of a structure matches the wavelength of the disturbance, resonance-like amplification occurs. This principle reappears throughout maritime physics—in wave-induced motions (treated in the *Ship Motions and Seakeeping* chapter of the companion volume), in structural vibration (Chapter 5), and in harbour resonance.

Equations 1.6–1.9, drawn from the foundational oscillation and wave framework of Campbell (2025), provide the mathematical language underlying all wave phenomena in this chapter. The defining equation of SHM (Equation 1.6) reappears whenever a restoring force is proportional to displacement—in the heave of a barge, the roll of a vessel, or the oscillation of water in a U-tube tank. The traveling wave equation (Equation 1.8) is the starting point for both regular and irregular sea descriptions, while the wave speed relation (Equation 1.9) connects the temporal and spatial characteristics of ocean waves.

The bore characterisation work of Hernández-Fontes et al. (2020) contributes to wave mechanics through the rigorous treatment of non-periodic shallow water waves. Their solitary wave approximation for wet dam-break bores (Equations 1.20–1.21) provides a consistent framework for defining bore steepness, which in turn governs the type of wave–structure interaction produced. The experimental finding that bore heights overestimate infinite-domain theoretical values by 10–16% highlights the sensitivity of bore propagation to boundary effects, including finite tank length and the presence of downstream structures. This has implications for laboratory-scale modelling of bore-like phenomena such as tsunamis and tidal bores.

The steepness parameter ε emerging from L_c^* offers a practical criterion for classifying incoming bore severity. As demonstrated by Hernández-Fontes et al. (2020), the range $0.12 \leq \varepsilon \leq 0.55$ spans qualitatively distinct regimes of wave–structure interaction (see the discussion of bore–structure interaction in the *Ship Motions and Seakeeping* chapter of the companion volume), from gentle overtopping to violent plunging events with large air cavity formation.

The wave generation theory of Pierini (2025) completes the physical chain from wind to waves. The Phillips resonance mechanism (Equation 1.4) explains the initial creation of surface waves from a calm sea, while the Miles shear instability mechanism (Equation 1.5) accounts for the rapid exponen-

tial growth that builds the wave field to its observed intensity. The critical height z_c—where the wind speed equals the wave phase velocity—governs the energy transfer rate, providing a direct physical explanation for the observation that stronger winds produce higher, longer waves with lower peak frequencies.

The Stokes wave theory (Equation 1.27) and cnoidal wave theory (Equation 1.31) from Pierini (2025) extend the chapter's nonlinear wave framework beyond the trochoidal profile of Attwood (1917). The Stokes expansion reveals the amplitude dependence of the dispersion relation ($\sigma^2 = gk(1 + a^2k^2)$, Equation 1.29), a nonlinear effect absent from linear Airy theory. The Stokes drift (Equation 1.30) has practical maritime applications in oil spill trajectory prediction and search-and-rescue planning. The Ursell number (Equation 1.33) provides a single dimensionless parameter for selecting the appropriate wave theory—linear, Stokes, or cnoidal—for a given combination of wave amplitude, wavelength, and water depth.

The perturbation expansion approach of Timman et al. (1985) places the linearised theory of Sections 1.3.1–1.3.3 on rigorous mathematical footing. By expanding the velocity potential and free-surface elevation in powers of the amplitude-to-wavelength ratio ε, the nonlinear free-surface conditions are systematically transferred to the known undisturbed surface, exposing the linear boundary-value problem as the $O(\varepsilon)$ approximation and the Stokes corrections as $O(\varepsilon^2)$ and higher terms. This hierarchy makes explicit both the domain of validity of linear Airy theory (small ε, i.e. small wave steepness) and the route to the nonlinear extensions of Section 1.3.3. The Kelvin wave pattern (Equation 1.19), derived from the same perturbation framework evaluated by the method of stationary phase, provides the analytical basis for the hull-speed concept (Equation 1.1): the half-angle of $\arctan(1/\sqrt{8}) \approx 19.47°$ is a universal geometric constant of the deep-water dispersion relation, independent of vessel speed. The rigorous proof that group velocity equals the propagation speed of the energy centroid unifies the kinematic definition $c_G = \mathrm{d}\omega/\mathrm{d}k$ with the energetics of wave propagation, confirming that Equation 1.25 governs not only swell arrival times but also the rate of energy delivery to coasts and offshore structures (Timman et al., 1985).

1.6 Conclusion

This chapter has developed the physics of ocean waves from first principles through to the statistical and nonlinear frameworks required for maritime engineering. Linear wave theory, formulated as a boundary-value problem for the velocity potential (Birk, 2019), yields the dispersion relation (Equation 1.17) that governs both the deep-water dispersive regime and the non-dispersive shallow-water limit. The critical hull speed (Equation 1.1) (Bejan et al., 2020) emerges as a direct consequence of the Kelvin wave pattern (Equation 1.19), connecting wave kinematics to the single most important

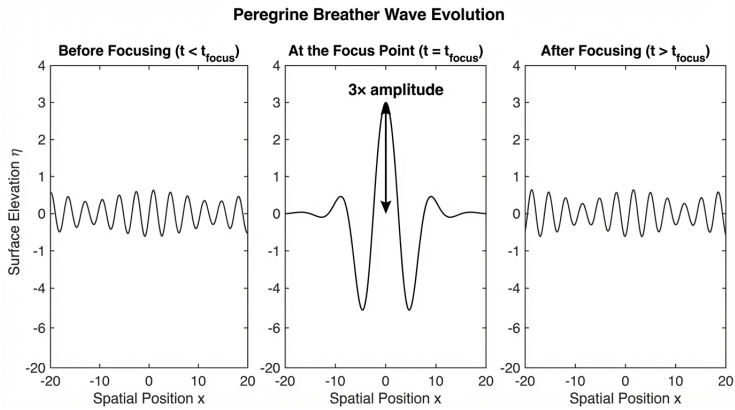

Figure 1.4: Schematic of the Peregrine breather evolution, showing the wave amplitude amplification from the background carrier wave (a_c) to the maximum focussing point ($\zeta_{\max} = 3\,a_c$, Equation 1.36). The breather appears from an apparently regular wave train, reaches threefold amplification at a single point in space and time, and disappears without trace. This localised extreme event is a candidate physical mechanism for deep-water rogue waves, consistent with the Draupner New Year Wave observation (Klein et al., 2021).

constraint on displacement-vessel performance (Timman et al., 1985). The energy equipartition result—kinetic and potential energy exactly equal in linear theory—together with the group velocity expression (Equation 1.25) establishes how wave energy propagates from generation regions to distant coastlines and offshore structures (Birk, 2019).

Beyond the linear regime, three progressively nonlinear frameworks extend the description of real ocean waves. The classical trochoidal profile (Attwood, 1917) captures the crest–trough asymmetry used in traditional hull-girder bending calculations, while the Stokes expansion (Pierini, 2025) introduces amplitude-dependent dispersion (Equation 1.29) and net mass transport via the Stokes drift (Equation 1.30). In shallow water, cnoidal wave theory governs propagation when the Ursell number exceeds unity (Equation 1.33), providing a practical criterion for selecting the appropriate wave model (Pierini, 2025). At the most extreme end of the nonlinear spectrum, the nonlinear Schrödinger equation (Equation 1.34) predicts modulational instability and the Peregrine breather's threefold amplitude amplification (Equation 1.36), offering a plausible physical mechanism for rogue wave formation consistent with the Draupner observation (Klein et al., 2021).

The statistical description of real sea states through the Pierson–Moskowitz spectrum (Equations 1.38–1.39) and directional spreading functions (Equation 1.40) provides the input to all spectral response calculations in subsequent chapters (Zhang et al., 2025). The bore characterisation framework of Hernández-Fontes et al. (2020), the harbour oscillation analysis

of Zheng et al. (2022), and the wind-wave generation theory of Pierini (2025) together demonstrate that the wave environment confronting ships and offshore structures is shaped by processes spanning time scales from fractions of a second (capillary waves) to hours (tidal oscillations and seiches) and spatial scales from centimetres to ocean basins. The extreme value methods of Guedes Soares and Santos (2015) close the chain from physics to engineering practice by providing the statistical tools needed to estimate design wave heights for return periods of 50–100 years. These wave mechanics foundations underpin the ship motions and seakeeping analysis presented in the *Ship Motions and Seakeeping* chapter of the companion volume and the structural loading calculations of Chapter 5.

References

Attwood, E. L. (1917). *A text-book of theoretical naval architecture* (7th ed.) [First published 1899; seventh edition revised 1916, reprinted 1917]. Longmans, Green; Co.

Bejan, A., Ferber, L., & Lorente, S. (2020). Convergent evolution of boats with sails. *Scientific Reports*, *10*, Article 2703. https://doi.org/10.1038/s41598-020-58940-5

Birk, L. (2019). *Fundamentals of ship hydrodynamics: Fluid mechanics, ship resistance and propulsion*. John Wiley & Sons.

Burton, D. A., & Noble, A. (2024). *A geometrical approach to physics*. Springer. https://doi.org/10.1201/9781003228943

Campbell, C. (2025). *Physics: A focused introduction*. CRC Press. https://doi.org/10.1201/9781003571568

Cushman-Roisin, B., & Beckers, J.-M. (2011). *Introduction to geophysical fluid dynamics: Physical and numerical aspects* (2nd ed.). Academic Press.

Dera, J. (1992). *Marine physics* (P. Senn, Trans.) [Translated from Polish. Original: *Fizyka morza*, 1983]. Elsevier.

Faltinsen, O. M. (1990). *Sea loads on ships and offshore structures*. Cambridge University Press.

Fischer-Cripps, A. C. (2014). *The physics companion* (2nd ed.). CRC Press. https://doi.org/10.1201/b17356

Gill, A. E. (1982). *Atmosphere-ocean dynamics* (Vol. 30). Academic Press.

Guedes Soares, C., & Santos, T. A. (Eds.). (2015). *Maritime technology and engineering: Proceedings of MARTECH 2014*. CRC Press.

Hernández-Fontes, J. V., Vitola, M. A., Esperança, P. T. T., Sphaier, S. H., & Silva, R. (2020). Patterns and vertical loads in water shipping in systematic wet dam-break experiments. *Ocean Engineering*, *197*, 106891. https://doi.org/10.1016/j.oceaneng.2019.106891

Hewitt, P. G., Suchocki, J. A., & Hewitt, L. A. (2012). *Conceptual physical science* (5th ed.). Pearson.

Klein, M., Clauss, G. F., & Hoffmann, N. (2021). Introducing envelope soliton solutions for wave–structure investigations. *Ocean Engineering*, *234*, 109271. https://doi.org/10.1016/j.oceaneng.2021.109271

Newman, J. N. (1977). *Marine hydrodynamics*. The MIT Press.

Pierini, S. (2025). *Oceanic and atmospheric fluid dynamics*. Springer. https://doi.org/10.1007/978-3-031-77991-6

Rawson, K. J., & Tupper, E. C. (2001). *Basic ship theory* (5th ed.). Butterworth-Heinemann.

Talley, L. D., Pickard, G. L., Emery, W. J., & Swift, J. H. (2011). *Descriptive physical oceanography: An introduction* (6th ed.). Academic Press.

Timman, R., Hermans, A. J., & Hsiao, G. C. (1985). *Water waves and ship hydrodynamics: An introduction*. Springer. https://doi.org/10.1007/978-94-017-3657-2

Zhang, J., Qu, L., Du, L., & Hong, G. (2025). Numerical modeling of vessel's wave-induced responses based on fast surface pressure method. *Ocean Engineering*, *337*, 121887. https://doi.org/10.1016/j.oceaneng.2025.121887

Zheng, Z., Ma, X., Yan, M., Ma, Y., & Dong, G. (2022). Hydrodynamic response of moored ships to seismic-induced harbor oscillations. *Coastal Engineering*, *176*, 104147. https://doi.org/10.1016/j.coastaleng.2022.104147

Chapter 2

Electromagnetism and Maritime Navigation

2.1 Introduction

Electromagnetic phenomena govern modern maritime navigation and communication systems—from radar and satellite positioning to radio communications and magnetic compasses (National Geospatial-Intelligence Agency, 2019; Skolnik, 2001). Furthermore, the interaction of electromagnetic radiation with seawater determines the optical properties of the ocean, governing light penetration, remote sensing capabilities, and the fundamental limits of vision and imaging underwater.

Dera (1992) provided a detailed treatment of light and electromagnetic radiation in the marine environment, covering both the inherent optical properties (absorption and scattering) of seawater and the apparent optical properties that describe underwater irradiance fields. This chapter presents the electromagnetic foundations alongside the optical physics of the ocean.

2.2 Scientific Background

2.2.1 Maxwell's Equations and Electromagnetic Waves

The electromagnetic theory underlying all maritime navigation and communication systems rests on four interrelated phenomena (Griffiths, 2013; Hewitt et al., 2012). The electric force between two stationary charges separated by distance r is given by Coulomb's law (Campbell, 2025):

Equation 10.10 — Coulomb's law:

$$F_E = K\,\frac{Qq}{r^2}, \qquad K = 8.99 \times 10^9\ \mathrm{N\,m^2\,C^{-2}} \tag{2.1}$$

where Q and q are the charges and K is the Coulomb constant (Campbell, 2025, Eq. 9.7). A charge Q creates an electric field $\vec{E}_Q = KQ/r^2\,\hat{r}$ in the surrounding

space, and any charge q immersed in that field experiences a force $\vec{F}_E = q\vec{E}$ (Campbell, 2025, Eq. 9.9).

Moving charges create magnetic fields and experience magnetic forces. For a charge q moving with velocity $\vec{v}$ through a magnetic field $\vec{B}$, the magnetic force is (Campbell, 2025, Eq. 12.3)

Equation 10.11 — Magnetic force on a moving charge:

$$\vec{F}_B = q(\vec{v} \times \vec{B}) \tag{2.2}$$

The combined electromagnetic force on a charged particle is the Lorentz force $\vec{F} = q(\vec{E} + \vec{v} \times \vec{B})$ (Campbell, 2025; Griffiths, 2013, Eq. 12.25), which governs the behaviour of charged particles in every maritime electromagnetic system, from radar waveguides to the ionospheric plasma that refracts radio signals.

The magnetic field produced by a current-carrying conductor is described by the Biot–Savart law. For a long straight wire carrying current I, the field at perpendicular distance R is (Campbell, 2025, Eq. 12.14)

Equation 10.12 — Magnetic field of a long straight wire:

$$B_{\text{wire}} = \frac{\mu_0 I}{2\pi R} \tag{2.3}$$

where $\mu_0 = 4\pi \times 10^{-7}\ \text{T m A}^{-1}$ is the permeability of free space. For a solenoid of n turns per unit length, $B_{\text{sol}} = \mu_0 n I$ (Campbell, 2025, Eq. 12.16)—a result directly applicable to the electromagnets used in compass correction and degaussing systems.

The link between time-varying magnetic fields and electric fields is provided by Faraday's law of electromagnetic induction (Campbell, 2025; Griffiths, 2013):

Equation 10.13 — Faraday's law:

$$\left| \frac{\mathrm{d}\Phi_B}{\mathrm{d}t} \right| = \varepsilon \tag{2.4}$$

where $\Phi_B = \int \vec{B} \cdot \mathrm{d}\vec{a}$ is the magnetic flux through a conducting loop and ε is the induced electromotive force (emf) (Campbell, 2025, Eqs. 12.20–12.22). This principle is the operating basis of every shipboard generator: mechanical rotation of a coil in a magnetic field produces a continuously changing flux that drives an alternating current (Campbell, 2025, Exs. 12.5, 12.13).

Maxwell unified these phenomena into four equations that, in free space, take the differential form (Griffiths, 2013):

$$\begin{aligned} \nabla \cdot \vec{E} &= \frac{\rho}{\varepsilon_0}, & \nabla \times \vec{E} &= -\frac{\partial \vec{B}}{\partial t}, \\ \nabla \cdot \vec{B} &= 0, & \nabla \times \vec{B} &= \mu_0 \vec{J} + \mu_0 \varepsilon_0 \frac{\partial \vec{E}}{\partial t} \end{aligned} \tag{2.5}$$

where ρ is the charge density, $\vec{J}$ is the current density, $\varepsilon_0 = 8.854 \times 10^{-12}\ \text{F m}^{-1}$ is the permittivity of free space, and μ_0 is the permeability

defined above. The crucial addition by Maxwell was the displacement current term $\mu_0\varepsilon_0\,\partial\vec{E}/\partial t$ in the last equation, which predicts that time-varying electric fields produce magnetic fields even in the absence of conduction currents (Griffiths, 2013); for a rigorous mathematical treatment, see (Burton & Noble, 2024).

In a source-free region ($\rho = 0$, $\vec{J} = \vec{0}$), these equations combine to yield the electromagnetic wave equation (Griffiths, 2013):

$$\nabla^2\vec{E} = \mu_0\varepsilon_0\frac{\partial^2\vec{E}}{\partial t^2} \tag{2.6}$$

from which the speed of electromagnetic waves in vacuum is $c = 1/\sqrt{\mu_0\varepsilon_0} = 2.998\times10^{8}\ \mathrm{m\,s^{-1}}$. Maritime systems exploit different portions of the electromagnetic spectrum: MF/HF radio (300 kHz–30 MHz) for long-range communication, VHF (30–300 MHz) for short-range radio and AIS, L-band ($\sim$ 1.5 GHz) for GNSS, and X-band (9.2–9.5 GHz) and S-band (2.9–3.1 GHz) for marine radar (National Geospatial-Intelligence Agency, 2019; Skolnik, 2001).

2.2.2 Electromagnetic Radiation at the Sea Surface

When solar radiation reaches the sea surface, a fraction is reflected and the remainder is transmitted into the water column. The partitioning depends on the angle of incidence, sea surface roughness, and the refractive index of seawater. The resulting vertical distribution of light governs the euphotic zone depth and the thermal structure of the upper ocean discussed in Chapter 4.

For a smooth sea surface with the refractive index $n \approx 4/3 \approx 1.33$ (visible light), the Fresnel reflection coefficient is approximately $R_s \approx 0.02$ for solar zenith angles less than 40° (Dera, 1992). At grazing incidence ($\theta_s = 90^\circ$), total reflection occurs ($R_s = 1$).

Dera (1992) showed that the transmittance of diffuse light through the sea surface under overcast skies is:

Equation 10.1 — Surface transmittance (overcast sky):

$$\langle T_p\rangle_{\text{cloudy}} \approx 0.95 \tag{2.7}$$

meaning that 95% of diffuse skylight penetrates the surface. For general conditions with fractional cloud cover n_c (Dera, 1992, Eq. 5.2.16):

$$\langle T_p\rangle = (1 - n_c)\,\langle T_{p,s}\rangle + 0.95\,n_c \tag{2.8}$$

where $\langle T_{p,s}\rangle$ is the clear-sky transmittance averaged over the day.

Once light enters the water, its radiance is enhanced by a factor of n^2 due to the compression of the solid angle by Snell's law refraction (Dera, 1992, Eq. 5.3.7):

$$\frac{L(\theta,\varphi)_{\text{below}}}{L(\theta,\varphi)_{\text{above}}} = n^2\,[1 - R_s(\theta)] \tag{2.9}$$

where L denotes spectral radiance and θ, φ are the zenith and azimuth angles.

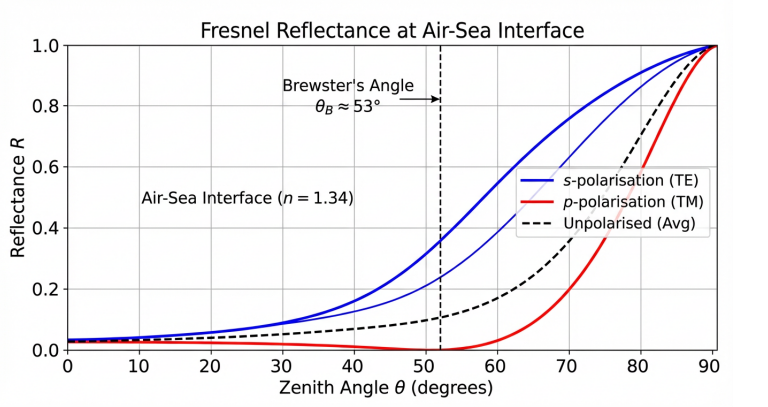

Figure 2.1: Fresnel reflection coefficient at the sea surface ($n = 1.33$) as a function of solar zenith angle θ_s for unpolarised, s-polarised, and p-polarised light. At low zenith angles less than approximately 2% of incident light is reflected, while at grazing incidence total reflection occurs. Brewster's angle marks the zero of R_p.

2.2.3 Earth's Magnetic Field

A magnetic dipole immersed in an external magnetic field experiences a torque (Campbell, 2025, Eq. 12.18):

Equation 10.14 — Torque on a magnetic dipole:

$$\vec{\tau} = \vec{m} \times \vec{B} \tag{2.10}$$

where $\vec{m}$ is the magnetic dipole moment and $\vec{B}$ is the external field. This torque drives the dipole toward alignment with the field. The corresponding potential energy is $U = -\vec{m} \cdot \vec{B}$, which is minimised when $\vec{m}$ and $\vec{B}$ are parallel (Campbell, 2025, Eq. 12.19); for a concise treatment, see (Fischer-Cripps, 2014).

The Earth behaves as a large magnetic dipole, with field lines emerging from the southern geographic hemisphere and entering near the northern geographic hemisphere (geographic north is magnetic south) (Campbell, 2025). At the Earth's surface the field strength is approximately 25–$65\ \mu$T, and its orientation is described by two angles: the magnetic declination (the horizontal angle between geographic north and magnetic north) and the magnetic inclination or dip (the angle below the horizontal) (National Geospatial-Intelligence Agency, 2019).

The geomagnetic field is not static: secular variation causes the declination and inclination to change slowly over time as convection currents in the Earth's liquid outer core evolve. The rate of secular variation differs by location; in some regions declination changes by more than $0.1°$ per year (National Geospatial-Intelligence Agency, 2019). Navigators must apply the current declination correction, which is printed on nautical charts together

with an annual rate of change. Geomagnetic reference models—updated at five-year intervals—provide the mathematical representation of the main field as a spherical harmonic expansion, enabling computation of declination, inclination, and total field intensity at any location and date (National Geospatial-Intelligence Agency, 2019). Local magnetic anomalies caused by geological structures (e.g. basaltic intrusions) can produce deviations of several degrees from the model values. Anomaly charts indicate regions where such discrepancies are significant for compass navigation (National Geospatial-Intelligence Agency, 2019).

2.3 Theoretical Framework

2.3.1 Inherent Optical Properties of Seawater

The optical behaviour of seawater is described by two sets of properties. The *inherent optical properties* (IOPs) depend only on the medium itself, not on the light field. The fundamental IOPs are the absorption coefficient $a\,[\mathrm{m}^{-1}]$, the scattering coefficient $b\,[\mathrm{m}^{-1}]$, and the total attenuation coefficient (Dera, 1992):

Equation 10.4 — Total attenuation coefficient:

$$c = a + b \quad [\mathrm{m}^{-1}] \tag{2.11}$$

These coefficients are functions of wavelength. Pure seawater has a minimum attenuation in the blue-green spectral window ($\lambda \approx 400$–$500\,\mathrm{nm}$), which is why the deep ocean appears blue (Dera, 1992).

2.3.2 Apparent Optical Properties and Underwater Irradiance

The *apparent optical properties* (AOPs) depend on both the medium and the angular structure of the ambient light field. The key AOP is the diffuse attenuation coefficient of downward irradiance:

Equation 10.5 — Diffuse attenuation coefficient:

$$K_d(z) = -\frac{1}{E_{\downarrow}(z)}\,\frac{\mathrm{d}E_{\downarrow}(z)}{\mathrm{d}z} \tag{2.12}$$

where $E_{\downarrow}(z)$ is the downward plane irradiance at depth z (Dera, 1992, Eq. 5.4.2). Integration yields the exponential decay law for underwater irradiance:

Equation 10.6 — Underwater irradiance (Beer–Lambert analogue):

$$E_{\downarrow}(z) = E_{\downarrow}(0)\,e^{-K_d z} \tag{2.13}$$

This is the oceanic equivalent of the Beer–Lambert law (Dera, 1992, Eq. 5.4.16). The fraction of surface irradiance reaching depth z is $T_{wE} = e^{-K_d z}$.

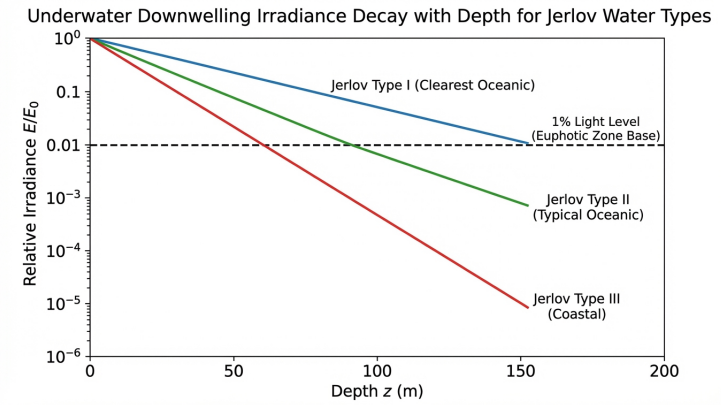

Figure 2.2: Exponential decay of normalised downward irradiance $E_{\downarrow}(z)/E_{\downarrow}(0)$ with depth for three Jerlov water types at $\lambda \approx 475$ nm: Type I (clear open ocean, $K_d = 0.017$ m^{-1}), Type III (productive ocean, $K_d = 0.055$ m^{-1}), and Coastal 5 (turbid nearshore, $K_d = 0.35$ m^{-1}). The dashed line marks the 1% irradiance level defining the euphotic zone depth (Equation 2.13).

A fundamental connection between the inherent and apparent optical properties is provided by the Gershun equation (Dera, 1992, Eq. 5.4.21b):

Equation 10.7 — Gershun equation:

$$\nabla \cdot \mathbf{E} = -a\, E_0 \tag{2.14}$$

where $\mathbf{E}$ is the irradiance vector and E_0 is the scalar irradiance. This equation states that the divergence of the irradiance vector equals the negative product of the absorption coefficient and the scalar irradiance. In a horizontally homogeneous ocean, it reduces to (Dera, 1992, Eq. 5.4.23):

$$\frac{\mathrm{d}E_z(z)}{\mathrm{d}z} = -a(z)\, E_0(z) \tag{2.15}$$

enabling in situ determination of the absorption coefficient from irradiance measurements.

The relationship between the diffuse attenuation coefficient and the absorption coefficient is (Dera, 1992, Eq. 5.4.24b):

$$K_z(z) = a(z) \cdot D(z) \tag{2.16}$$

where $D(z)$ is the distribution function characterising the angular spread of the light field. The absorbed radiant power per unit volume is $\mathrm{d}P/\mathrm{d}V = -a\, E_0$ [W m^{-3}] (Dera, 1992, Eq. 5.4.22).

2.3.3 Ocean Water Classification

Ocean waters are classified by their optical clarity according to the Jerlov system (Dera, 1992):

- **Type I** (clearest open ocean): 1% irradiance depth ~ 140 m at $\lambda = 475$ nm; maximum transparency in the blue.
- **Type III** (productive open ocean): 1% depth ~ 40 m.
- **Coastal type 5** (turbid nearshore): 1% depth ~ 10 m.

At longer wavelengths such as red light ($\lambda = 600$ nm), even type I water attenuates the irradiance to 1% at only ~ 20 m depth, illustrating the strong wavelength dependence of absorption (Dera, 1992).

2.3.4 Radar Physics and Principles

Marine radar operates by transmitting short pulses of microwave energy and detecting the echoes reflected by targets. The fundamental relationship governing radar detection is the radar equation (Skolnik, 2001):

$$P_r = \frac{P_t G^2 \lambda^2 \sigma}{(4\pi)^3 R^4} \tag{2.17}$$

where P_r is the received power, P_t is the transmitted power, G is the antenna gain, λ is the wavelength, σ is the radar cross section (RCS) of the target in m^2, and R is the range to the target. The R^{-4} dependence arises because the signal travels to the target (spreading as R^{-2}) and the echo returns over the same path (another R^{-2}) (Skolnik, 2001).

The radar cross section σ is a measure of the target's reflectivity and depends on its size, shape, material, and orientation relative to the radar beam. A large metal ship broadside-on may present $\sigma \sim 10^3$–10^5 m^2, while a small fibreglass yacht may have $\sigma < 1$ m^2 (Skolnik, 2001).

The range resolution of a pulsed radar is $\Delta R = c\tau/2$, where τ is the pulse duration and the factor of 2 accounts for the round trip. A typical marine radar with $\tau = 0.05$ µs achieves $\Delta R \approx 7.5$ m. The bearing resolution is determined by the horizontal beamwidth of the antenna, which for a marine radar with a 1.2 m slotted-waveguide antenna at X-band is approximately 1.2° (Skolnik, 2001).

2.3.5 Antenna Theory for Maritime Applications

An antenna converts between guided electromagnetic energy and free-space radiation. The fundamental radiating element is the half-wave dipole, whose radiation pattern is a toroid with maximum intensity perpendicular to the antenna axis (Griffiths, 2013). The antenna gain G quantifies the concentration of radiated power relative to an isotropic (omnidirectional) radiator: $G = 4\pi A_e/\lambda^2$, where A_e is the effective aperture area (Skolnik, 2001). For a rectangular aperture antenna of physical area A, the effective aperture is $A_e = \eta_a A$, where $\eta_a \approx 0.5$–0.7 is the aperture efficiency (Skolnik, 2001).

Marine radar antennas are predominantly *slotted-waveguide* arrays: a rectangular waveguide with precisely spaced slots cut into one wall, each slot acting as a radiating element (Skolnik, 2001). The phase relationship between the slot elements produces a narrow horizontal beam (typically 0.8–2°) and a broader vertical beam (~ 20–25°). The narrow horizontal beamwidth provides the bearing discrimination essential for navigation, while the broad vertical beam accommodates the ship's roll motion. The antenna rotates at 20–25 rpm to provide 360° azimuthal coverage (Skolnik, 2001).

2.3.6 Global Navigation Satellite Systems (GNSS)

Global Navigation Satellite Systems (GNSS) determine position by measuring the propagation time of electromagnetic signals from satellites at known orbital positions. Each satellite transmits a coded signal containing its ephemeris (orbital parameters) and precise time from an onboard atomic clock. The receiver measures the pseudorange to each satellite (National Geospatial-Intelligence Agency, 2019):

$$\rho_i = c\,(t_{\text{rx}} - t_{\text{tx},i}) = R_i + c\,\delta t_{\text{rx}} \tag{2.18}$$

where ρ_i is the pseudorange to satellite i, R_i is the true geometric range, c is the speed of light, t_{rx} and $t_{\text{tx},i}$ are the reception and transmission times, and δt_{rx} is the receiver clock bias. Because four unknowns must be resolved (three position coordinates plus the clock bias), a minimum of four satellites must be simultaneously observed (National Geospatial-Intelligence Agency, 2019).

The accuracy of the position fix depends on the geometric arrangement of the observed satellites, quantified by the *dilution of precision* (DOP). A low DOP value (satellites widely spread across the sky) yields a strong geometry and high accuracy; a high DOP (satellites clustered together) degrades the solution. Under open-sky conditions with good geometry, single-frequency civilian GNSS provides a horizontal accuracy of approximately 5–10 m (95% confidence) (National Geospatial-Intelligence Agency, 2019).

Four operational GNSS constellations are available: the US Global Positioning System (GPS, L-band: 1575.42 MHz and 1227.60 MHz), the Russian GLONASS, the European Galileo, and the Chinese BeiDou. Multi-constellation receivers track satellites from all constellations simultaneously, improving geometry and availability, particularly in areas of restricted sky visibility such as ports and narrow waterways (National Geospatial-Intelligence Agency, 2019).

2.3.7 Differential GNSS and Augmentation Systems

Differential GNSS (DGNSS) improves positioning accuracy by broadcasting corrections derived from a reference station at a known location. The reference station computes the difference between the measured and true pseudoranges and transmits these corrections to the user receiver, which

applies them to its own measurements. This technique eliminates common-mode errors (atmospheric delays, satellite clock offsets) and typically reduces the horizontal position error to 1–3 m (National Geospatial-Intelligence Agency, 2019).

Satellite-Based Augmentation Systems (SBAS) provide differential corrections over a wide area via geostationary satellites. Regional implementations include the Wide Area Augmentation System (WAAS, North America) and the European Geostationary Navigation Overlay Service (EGNOS, Europe). SBAS corrections improve accuracy to approximately 1–2 m horizontally and additionally provide integrity monitoring—alerting users within seconds if a satellite signal becomes unreliable (National Geospatial-Intelligence Agency, 2019).

For high-precision applications such as hydrographic survey and harbour approach, Real-Time Kinematic (RTK) positioning resolves the carrier-phase ambiguity of the GNSS signal to achieve centimetre-level accuracy. RTK requires a local reference station (or a network of stations) transmitting carrier-phase corrections, and the baseline between the reference and user must typically be less than 20–50 km (National Geospatial-Intelligence Agency, 2019).

2.3.8 Magnetic Compass Physics

The magnetic compass operates on the principle expressed in Equation 2.10: a magnetised needle, free to rotate on a pivot, experiences a torque $\vec{\tau} = \vec{m} \times \vec{B}$ that aligns it with the local geomagnetic field (Campbell, 2025). The torque magnitude is $\tau = mB \sin\theta$, where θ is the angle between the needle's dipole moment $\vec{m}$ and the horizontal component of the Earth's field $\vec{B}_H$. Equilibrium is reached when $\theta = 0$ (needle aligned with magnetic north).

In practice, the compass needle does not settle instantaneously but undergoes damped oscillation about the equilibrium direction, with a natural period $T \propto \sqrt{I_{\text{needle}}/(mB_H)}$, where I_{needle} is the needle's moment of inertia. On steel-hulled vessels, the ship's own ferromagnetic structure creates a local magnetic field that deflects the compass from magnetic north—an error called *deviation* (National Geospatial-Intelligence Agency, 2019). Compass adjustment compensates for this deviation using corrector magnets, Flinders bars, and soft-iron spheres arranged to cancel the ship's magnetic signature at the compass location.

The deviation of a magnetic compass on a steel vessel is a systematic function of the ship's heading ψ. It is classically decomposed into five harmonic coefficients (National Geospatial-Intelligence Agency, 2019):

$$\delta(\psi) = A + B\sin\psi + C\cos\psi + D\sin 2\psi + E\cos 2\psi \tag{2.19}$$

where A represents a constant (asymmetric soft iron), B and C are semicircular deviations caused by permanent magnetism of the hull (corrected by permanent magnets), and D and E are quadrantal deviations arising from induced magnetism in the ship's horizontal soft iron (corrected by soft-iron

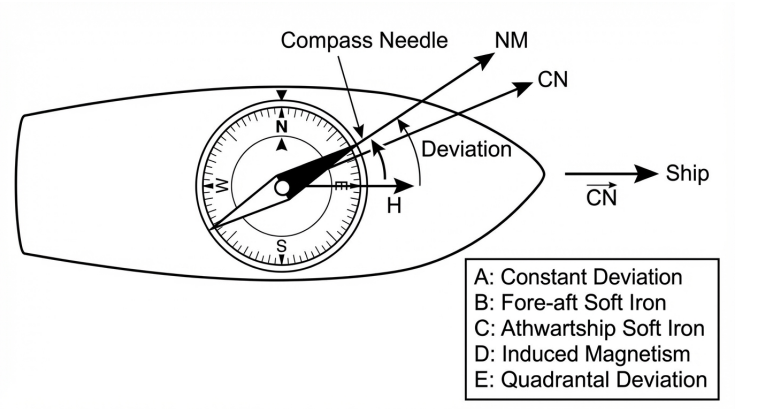

Figure 2.3: Magnetic compass schematic showing the restoring torque $\vec{\tau} = \vec{m} \times \vec{B}$ (Equation 2.10) that drives the compass needle (dipole moment $\vec{m}$) toward alignment with the Earth's horizontal field $\vec{B}_H$. The deviation angle δ arises from the ship's ferromagnetic structure, which creates a local field that deflects the needle from magnetic north.

spheres) (National Geospatial-Intelligence Agency, 2019). A deviation table or curve is prepared by swinging the ship through all headings and comparing the compass reading against a known reference.

A further error arises when the vessel heels: the vertical component of the ship's permanent magnetism, which has no effect on the horizontal compass needle when the ship is upright, acquires a horizontal component proportional to the sine of the heel angle. This *heeling error* is most pronounced on north–south headings and is corrected by a vertical permanent magnet (heeling magnet) placed below the compass (National Geospatial-Intelligence Agency, 2019).

2.3.9 Gyroscope Physics and Inertial Navigation

A gyroscope is a spinning body whose angular momentum $\vec{L} = I\vec{\omega}$ resists changes to its orientation. When an external torque $\vec{\tau}$ is applied perpendicular to the spin axis, the angular momentum vector precesses according to $\vec{\tau} = \mathrm{d}\vec{L}/\mathrm{d}t$, causing the spin axis to rotate at right angles to both the torque and the spin axis (Campbell, 2025). A *gyrocompass* exploits this property: a spinning rotor is constrained so that the Earth's rotation provides a small torque that causes the spin axis to precess until it aligns with the geographic meridian (true north), independent of the ship's magnetic environment (National Geospatial-Intelligence Agency, 2019).

The gyrocompass replaced the magnetic compass as the primary heading reference on large vessels because it indicates true north (no declination or deviation correction required), is unaffected by the ship's ferromagnetic struc-

ture, and provides a stable heading input to radar, ECDIS, and autopilot systems (National Geospatial-Intelligence Agency, 2019). Errors in the gyrocompass arise from speed and latitude effects: the vessel's velocity over the ground has a component that mimics Earth rotation, producing a heading error that increases with speed and latitude and must be corrected either manually or by the compass electronics (National Geospatial-Intelligence Agency, 2019).

Modern inertial navigation systems (INS) use triads of gyroscopes and accelerometers to measure angular rate and specific force in three axes. Integration of these measurements yields attitude, velocity, and position without external references. *Ring laser gyroscopes* (RLG) and *fibre optic gyroscopes* (FOG) measure angular rate via the Sagnac effect: two counter-propagating laser beams in a closed path experience different optical path lengths when the platform rotates, producing an interferometric fringe shift proportional to the rotation rate (National Geospatial-Intelligence Agency, 2019). Because INS position errors grow with time due to sensor drift, shipboard INS is invariably aided by GNSS (Section 2.3.6); the GNSS provides bounded position accuracy while the INS provides continuous high-rate attitude and velocity data between GNSS updates (National Geospatial-Intelligence Agency, 2019).

2.3.10 Automatic Identification System (AIS) and VHF Communication

VHF radio (156–$174\,\mathrm{MHz}$) is the primary short-range maritime communication band. Propagation at VHF frequencies is essentially line-of-sight, with the radio horizon slightly beyond the geometric horizon due to atmospheric refraction. The range between two stations with antenna heights h_1 and h_2 (in metres) is approximately $R \approx 2.2(\sqrt{h_1} + \sqrt{h_2})$ nautical miles, where the factor 2.2 accounts for standard atmospheric refraction (National Geospatial-Intelligence Agency, 2019).

The *Automatic Identification System* (AIS) operates on two dedicated VHF channels ($161.975\,\mathrm{MHz}$ and $162.025\,\mathrm{MHz}$) using Self-Organising Time Division Multiple Access (SOTDMA). Each equipped vessel periodically broadcasts a data packet containing its identity (MMSI), position (from GNSS), course, speed, heading, rate of turn, and navigational status. The transmission rate adapts to the vessel's dynamic state: a vessel at anchor transmits every $3\,\mathrm{min}$, while a vessel manoeuvring at high speed transmits every $2\,\mathrm{s}$ (National Geospatial-Intelligence Agency, 2019). The SOTDMA protocol allows each station to autonomously reserve time slots in the $1\,\mathrm{min}$ frame, enabling the channel to support more than 4,500 reports per minute per channel without central coordination (National Geospatial-Intelligence Agency, 2019).

2.4 Applications in Maritime Systems

2.4.1 Electronic Chart Display and Information System (ECDIS)

The Electronic Chart Display and Information System (ECDIS) integrates navigation sensor data—GNSS position, gyrocompass heading, radar overlay, AIS targets, echo sounder depth—onto an electronic navigational chart (ENC). The ENC is a vector chart in the S-57 standard, containing georeferenced features (coastline, depth contours, aids to navigation, traffic separation schemes) stored in layers that can be selectively displayed (National Geospatial-Intelligence Agency, 2019).

The chart datum defines the vertical reference for charted depths. The datum adopted by the International Hydrographic Organization is *Lowest Astronomical Tide* (LAT), meaning that charted depths represent the minimum depth that can be expected under any combination of astronomical tidal constituents. The navigator must add the predicted tidal height to the charted depth to obtain the actual water depth at the time of passage (National Geospatial-Intelligence Agency, 2019).

ECDIS provides automated watchkeeping functions including route monitoring (cross-track distance alarm), grounding avoidance (comparison of draught against charted depth plus safety contour), and target tracking (AIS and radar fusion). When type-approved ECDIS with up-to-date ENC data is carried, it satisfies the SOLAS chart carriage requirement, replacing the paper chart as the primary means of navigation (National Geospatial-Intelligence Agency, 2019).

2.4.2 Radar Navigation and Collision Avoidance (ARPA)

Automatic Radar Plotting Aid (ARPA) functionality extracts target motion information from the radar display. After a target echo has been acquired (automatically or manually), the system tracks its position over successive antenna scans, fitting a track to the sequence of plots to estimate the target's course and speed (National Geospatial-Intelligence Agency, 2019).

From the relative motion between own ship and the tracked target, ARPA computes two critical collision avoidance parameters: the *Closest Point of Approach* (CPA), which is the minimum distance the target will pass if both vessels maintain their present courses and speeds, and the *Time to Closest Point of Approach* (TCPA), which is the time remaining until that point is reached. If CPA falls below a navigator-set threshold (a common value is 1 nautical mile), the system generates an alarm (National Geospatial-Intelligence Agency, 2019).

The ARPA also supports *trial manoeuvre*: the navigator can simulate a proposed change of course or speed and observe the resulting effect on CPA/TCPA for all tracked targets before executing the manoeuvre. This allows systematic assessment of compliance with the International Regulations for Preventing

Collisions at Sea (COLREGs). The tracking accuracy depends on the quality of the radar signal, the target's radar cross section (Equation 2.17), and the sea clutter environment (National Geospatial-Intelligence Agency, 2019; Skolnik, 2001).

2.4.3 Voyage Data Recorder (VDR)

The Voyage Data Recorder (VDR) is the maritime equivalent of the aviation flight recorder. It continuously records data from the ship's navigation and communication sensors: radar image, audio from the bridge, VHF radio communications, GNSS position, heading, speed, depth, engine orders, rudder angle, hull openings status, and fire and watertight door alarms (National Geospatial-Intelligence Agency, 2019).

The recorded data is stored in a protective capsule designed to survive a maritime casualty. The capsule must withstand immersion at a depth corresponding to the seabed at the ship's operating area (at least 6000 m depth, equivalent to a hydrostatic pressure of approximately 60 MPa), exposure to a temperature of $1100\,^{\circ}$C for 60 min (fire survival), and a mechanical shock of 250 g for 6 ms (impact survival). The capsule incorporates a locating beacon (ultrasonic pinger and satellite EPIRB) that activates on immersion to enable recovery (National Geospatial-Intelligence Agency, 2019). The VDR retains at least the final 12 h of data in a continuous-overwrite buffer.

2.4.4 Long Range Identification and Tracking (LRIT)

Long Range Identification and Tracking (LRIT) provides global ship tracking through satellite communication. Each SOLAS-class vessel transmits a position report (derived from its GNSS receiver) at six-hour intervals via an Inmarsat-C satellite terminal to a national data centre (National Geospatial-Intelligence Agency, 2019).

The Inmarsat system uses geostationary satellites at an altitude of approximately $35\,786$ km operating in the L-band (1.5–1.6 GHz). At this altitude, the orbital period equals the Earth's rotation period, so the satellite remains stationary relative to the ground. The signal path length of $\sim\ 36\,000$ km introduces a one-way propagation delay of $\sim\ 120$ ms and requires a link budget that accounts for free-space path loss of approximately 188 dB at 1.5 GHz (Skolnik, 2001). The ship earth station (SES) uses a small omnidirectional or low-gain antenna, and the satellite's high-gain spot beams close the link despite the modest shipboard antenna (National Geospatial-Intelligence Agency, 2019). Beyond LRIT, the Inmarsat system supports ship-to-shore telephony, data communication, and the Global Maritime Distress and Safety System (GMDSS) distress alerting (National Geospatial-Intelligence Agency, 2019).

2.5 Discussion

The optical properties of seawater and the physics of electromagnetic wave propagation represent two facets of the same fundamental interaction between electromagnetic fields and matter. In the marine environment, this interaction is characterised by two striking contrasts: (i) the extreme transparency of the ocean to acoustic waves versus the rapid attenuation of electromagnetic radiation (compare the SOFAR channel range of thousands of kilometres with the photic zone of $\sim$10–140 m), and (ii) the wavelength dependence that makes the ocean a spectral filter, transmitting blue-green light and absorbing red and infrared radiation within the first few metres (Dera, 1992). The electromagnetic foundations presented in Section 2.2.1—Coulomb's law (Equation 2.1), the magnetic force (Equation 2.2), and Faraday's law (Equation 2.4)—govern the full range of maritime navigation and communication technologies. Faraday's law, in particular, is the operating principle of ship generators, and the Biot–Savart result (Equation 2.3) governs both degaussing coil design and compass corrector magnet placement (Campbell, 2025; Griffiths, 2013). The integration of multiple electromagnetic navigation systems—GNSS, radar, gyrocompass, AIS, ECDIS—into a coherent bridge system has transformed isolated instruments into a fused navigation environment. The redundancy inherent in carrying independent position sources (GNSS trilateration, radar fixing, dead reckoning from INS) reflects the fundamental principle that no single electromagnetic measurement is immune to failure: GNSS signals can be jammed or spoofed, radar is degraded by sea clutter and propagation anomalies, and the gyrocompass drifts during power interruptions (National Geospatial-Intelligence Agency, 2019). The navigator's task is to cross-check these independent sources continuously and maintain situational awareness that transcends any individual sensor.

The electromagnetic frontier in maritime navigation is the transition toward *e-Navigation*: a harmonised framework in which shipboard and shore-based systems exchange data digitally to enhance navigational safety and efficiency. The physics underpinning this transition remains the same—Maxwell's equations (Equation 2.5), satellite ranging (Equation 2.18), and the radar equation (Equation 2.17)—but the information layer built upon it grows steadily richer, enabling route optimisation, automated collision avoidance algorithms, and real-time hydrographic data dissemination (National Geospatial-Intelligence Agency, 2019).

2.6 Conclusion

Electromagnetic phenomena govern two complementary domains of maritime technology: the interaction of light with seawater and the navigation and communication systems built on Maxwell's equations. The refractive index of seawater ($n \approx 1.33$) controls Fresnel reflection at the air–sea inter-

face, with less than 2% reflected at high sun angles rising to total reflection at grazing incidence (Dera, 1992). Below the surface, underwater irradiance follows exponential decay (Equation 2.13), governed by the diffuse attenuation coefficient K_d whose magnitude varies across the Jerlov classification from ~ 0.017 m^{-1} (Type I, euphotic depth ~ 140 m) to ~ 0.35 m^{-1} (Coastal 5, ~ 10 m) (Dera, 1992). The Gershun equation (Equation 2.14) provides the fundamental connection between the divergence of the irradiance vector and the absorption coefficient, enabling in situ determination of inherent optical properties from irradiance measurements.

The electromagnetic foundations—Coulomb's law (Equation 2.1), the magnetic force on moving charges (Equation 2.2), the Biot–Savart law (Equation 2.3), and Faraday's law of induction (Equation 2.4)—govern radar, GNSS, radio communications, shipboard power generation, and compass correction systems (Campbell, 2025; Griffiths, 2013). The magnetic compass exploits the torque $\vec{\tau} = \vec{m} \times \vec{B}$ (Equation 2.10) to align with the Earth's horizontal field, while deviation arising from the ship's ferromagnetic structure must be compensated by careful adjustment. The contrast between the ocean's extreme transparency to acoustic waves and the rapid attenuation of electromagnetic radiation—the SOFAR channel spans thousands of kilometres while the photic zone extends at most 140 m—defines the fundamental operating envelopes for underwater sensing and communication, a theme developed further in Chapter 6.

References

Burton, D. A., & Noble, A. (2024). *A geometrical approach to physics*. Springer. https://doi.org/10.1201/9781003228943

Campbell, C. (2025). *Physics: A focused introduction*. CRC Press. https://doi.org/10.1201/9781003571568

Dera, J. (1992). *Marine physics* (P. Senn, Trans.) [Translated from Polish. Original: *Fizyka morza*, 1983]. Elsevier.

Fischer-Cripps, A. C. (2014). *The physics companion* (2nd ed.). CRC Press. https://doi.org/10.1201/b17356

Griffiths, D. J. (2013). *Introduction to electrodynamics* (4th ed.). Pearson.

Hewitt, P. G., Suchocki, J. A., & Hewitt, L. A. (2012). *Conceptual physical science* (5th ed.). Pearson.

National Geospatial-Intelligence Agency. (2019). *The American practical navigator (Bowditch)* [Bicentennial edition; originally published 1802 by Nathaniel Bowditch].

Skolnik, M. I. (2001). *Introduction to radar systems* (3rd ed.). McGraw-Hill.

Chapter 3

Marine Meteorology and Atmospheric Physics

3.1 Introduction

The atmosphere and the ocean form a coupled thermodynamic system, exchanging heat, moisture, and momentum across the air–sea interface. Atmospheric physics determines maritime safety and efficiency: wind drives waves and surface currents, pressure systems generate storms, and the Coriolis effect organises both atmospheric and oceanic circulation on planetary scales.

Dera (1992) treated the atmosphere–ocean interaction as one of the central problems of marine physics, connecting solar radiation input, heat exchange at the sea surface, and the Coriolis force that dominates large-scale motion in both fluids.

3.2 Scientific Background

3.2.1 Atmospheric Structure and Composition

The atmosphere is divided into distinct layers defined by their temperature profiles (Wallace & Hobbs, 2006). Cornish and Ives (2009) describe the *troposphere* as the lowest layer, extending from the surface to approximately 11 km at mid-latitudes (higher at the equator, lower at the poles), within which temperature generally decreases with altitude. The rate of this decrease is the *lapse rate*. The *dry adiabatic lapse rate* (DALR) is the rate at which an unsaturated parcel of air cools as it rises adiabatically:

Equation 11.3 — Dry adiabatic lapse rate:

$$\Gamma_d = \frac{g}{c_p} \approx 9.8\,^{\circ}\mathrm{C\,km^{-1}} \tag{3.1}$$

where g is gravitational acceleration and c_p is the specific heat capacity of dry air at constant pressure (Cornish & Ives, 2009); for a concise treatment, see

(Fischer-Cripps, 2014). When a rising air parcel becomes saturated and condensation occurs, the release of latent heat reduces the cooling rate; this *saturated adiabatic lapse rate* (SALR) is variable (typically $4\,^{\circ}\mathrm{C\,km^{-1}}$ to $7\,^{\circ}\mathrm{C\,km^{-1}}$) depending on temperature and moisture content (Cornish & Ives, 2009).

The atmospheric stability of an air column depends on the relationship between the *environmental lapse rate* (ELR)—the actual measured rate of temperature decrease—and the DALR/SALR. When the ELR exceeds the DALR, the atmosphere is *absolutely unstable*: a displaced air parcel continues to accelerate upward, promoting convection and cloud formation. When the ELR is less than the SALR, the atmosphere is *absolutely stable*: displaced parcels return to their original level. Between these extremes lies *conditional instability*, where the atmosphere is stable for unsaturated air but unstable once saturation is reached (Cornish & Ives, 2009).

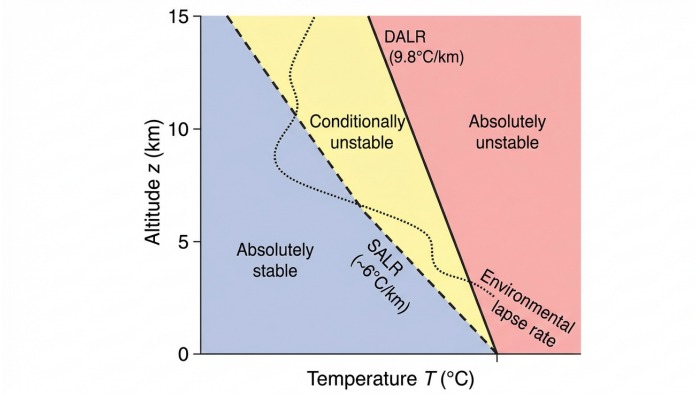

Figure 3.1: Atmospheric lapse rates and stability regimes. The dry adiabatic lapse rate ($\mathrm{DALR} = g/c_p \approx 9.8\,^{\circ}\mathrm{C\,km^{-1}}$; Equation 3.1) and the saturated adiabatic lapse rate ($\mathrm{SALR} \approx 5.5\,^{\circ}\mathrm{C\,km^{-1}}$) define the boundaries of conditional instability. Environmental lapse rates steeper than the DALR produce absolute instability and convection; rates gentler than the SALR produce absolute stability.

Above the troposphere lies the *tropopause*, a boundary marked by a temperature minimum, and then the *stratosphere*, where temperature increases with altitude due to absorption of ultraviolet radiation by ozone. The stratosphere is inherently stable and effectively caps the vertical extent of weather systems (Cornish & Ives, 2009; Wallace & Hobbs, 2006).

3.2.2 Solar Radiation and Earth's Energy Balance

The primary energy input to the atmosphere–ocean system is solar radiation. Of the shortwave radiation reaching the sea surface, a fraction is reflected (Figure 10.1 context in Chapter 2) and the remainder is transmitted into the water

column. Under overcast skies, approximately 95% of the incident diffuse radiation penetrates the surface (Chapter 2, Equation 2.7), while under clear skies the reflection depends on solar altitude (Dera, 1992).

The absorbed solar radiation heats the upper ocean, establishing the thermal structure (mixed layer, thermocline) described in Chapter 4. The ocean in turn releases heat to the atmosphere through longwave radiation, sensible heat flux, and latent heat flux (evaporation). This exchange drives atmospheric circulation and sustains the global hydrological cycle (Dera, 1992).

The total solar irradiance at the mean Earth–Sun distance (the *solar constant*) is approximately $S_0 \approx 1361\,\mathrm{W\,m^{-2}}$ (Wallace & Hobbs, 2006). Because the Earth presents a cross-sectional area πR_E^2 to the solar beam while its total surface area is $4\pi R_E^2$, the globally and annually averaged insolation is $S_0/4 \approx 340\,\mathrm{W\,m^{-2}}$. Of this incoming radiation, approximately 30% is reflected back to space by clouds, aerosols, and the surface without being absorbed; this fraction is the *planetary albedo* $\alpha_p \approx 0.30$ (Wallace & Hobbs, 2006). The remaining 70% ($\approx 238\,\mathrm{W\,m^{-2}}$) is absorbed by the surface and atmosphere, establishing the energy source that drives all atmospheric and oceanic circulation.

For the planet to be in radiative equilibrium, the absorbed solar radiation must equal the outgoing longwave radiation emitted to space. By the Stefan–Boltzmann law, the *effective emission temperature* required for this balance is (Wallace & Hobbs, 2006):

$$T_e = \left(\frac{S_0 (1 - \alpha_p)}{4\sigma} \right)^{1/4} \approx 255\,\mathrm{K} \tag{3.2}$$

where $\sigma = 5.67 \times 10^{-8}\,\mathrm{W\,m^{-2}\,K^{-4}}$ is the Stefan–Boltzmann constant. This temperature is approximately $33\,\mathrm{K}$ below the observed global mean surface temperature ($\approx 288\,\mathrm{K}$); the difference is attributable to the atmospheric greenhouse effect, in which water vapour, carbon dioxide, and other trace gases absorb and re-emit longwave radiation, reducing the net radiative loss from the surface (Wallace & Hobbs, 2006).

Over the ocean, the surface albedo is low ($\alpha_s \approx 0.06$–0.10 for solar elevations above 30°; see the Fresnel reflectance treatment in Chapter 2), so the sea surface absorbs a larger fraction of the incident solar radiation than most land surfaces. This asymmetry makes the ocean the dominant thermal reservoir of the climate system, absorbing approximately 90% of the excess energy in the Earth system (Dera, 1992).

3.2.3 Atmospheric Pressure and Measurement

Atmospheric pressure at sea level averages approximately $1013.25\,\mathrm{hPa}$ ($1\,\mathrm{atm}$). Cornish and Ives (2009) explain that pressure decreases approximately exponentially with altitude according to the hypsometric equation:

$$z_2 - z_1 = \frac{R_d \bar{T}}{g} \ln \frac{p_1}{p_2} \tag{3.3}$$

where $R_d = 287\,\mathrm{J\,kg^{-1}\,K^{-1}}$ is the gas constant for dry air, $\bar{T}$ is the mean virtual temperature of the layer, g is gravitational acceleration, and p_1, p_2 are the pressures at heights z_1, z_2 (Cornish & Ives, 2009). Lines of equal pressure on a weather chart are *isobars*; their spacing indicates the pressure gradient and hence the wind speed. Close isobars indicate strong pressure gradients and high winds—a critical feature for mariners to recognise on synoptic charts (Cornish & Ives, 2009).

The *barometric tendency*—the change of pressure over the preceding three hours—is one of the most valuable indicators of approaching weather systems at sea. A rapidly falling barometer indicates the approach of a depression (low-pressure system) and the likelihood of deteriorating weather, while a rising barometer signals the passage of a front or the establishment of an anticyclone (Cornish & Ives, 2009).

3.3 Theoretical Framework

3.3.1 Wind Systems and the Coriolis Effect

The most important consequence of the Earth's rotation for atmospheric and oceanic dynamics is the Coriolis effect (Holton & Hakim, 2013). Dera (1992) derived the Coriolis acceleration for a body moving with velocity $\mathbf{v}$ on the rotating Earth:

Equation 11.1 — Coriolis acceleration:

$$\mathbf{a}_C = 2\,\boldsymbol{\omega} \times \mathbf{v} \tag{3.4}$$

where $\boldsymbol{\omega}$ is the Earth's angular velocity vector ($\omega = 7.292 \times 10^{-5}$ rad s^{-1}) (Dera, 1992, Eq. 1.2.31). For horizontal motion, the dominant component acts perpendicular to the velocity (to the right in the Northern Hemisphere, to the left in the Southern) with magnitude proportional to the Coriolis parameter:

$$f = 2\omega \sin\varphi \tag{3.5}$$

where φ is the geographic latitude (Dera, 1992, Eq. 1.2.33).

The Coriolis effect explains why wind does not blow directly from high to low pressure. Instead, it deflects the flow until a balance is reached between the pressure gradient force and the Coriolis force, producing the *geostrophic wind* that blows approximately parallel to the isobars (Holton & Hakim, 2013).

In the free atmosphere above the friction layer (approximately $1000\,\mathrm{m}$ above the surface), the Coriolis force balances the horizontal pressure gradient force. Cornish and Ives (2009) derive the geostrophic wind speed as:

$$V_g = \frac{1}{\rho f}\frac{\Delta p}{\Delta n} \tag{3.6}$$

where ρ is the air density, $f = 2\omega\sin\varphi$ is the Coriolis parameter (Equation 3.5), and $\Delta p/\Delta n$ is the horizontal pressure gradient measured perpendicular to the

isobars (Cornish & Ives, 2009). The geostrophic wind blows parallel to the isobars, with low pressure to the left in the Northern Hemisphere (Buys Ballot's law).

Near the surface, friction with the sea (or land) reduces the wind speed and causes the wind to blow across the isobars toward low pressure. The angle of deviation is approximately 10–15° over the open sea and 25–40° over land (Cornish & Ives, 2009). This frictional deflection is the mechanism by which air converges into low-pressure centres, sustaining the upward motion that produces cloud and precipitation.

Where isobars are curved, the geostrophic balance is modified by the centripetal acceleration, producing the *gradient wind* (Holton & Hakim, 2013). In a cyclone (curved isobars around a low), the gradient wind is subgeostrophic (slower than the geostrophic value), while in an anticyclone it is supergeostrophic (Cornish & Ives, 2009).

3.3.2 Global Atmospheric Circulation

The unequal heating of the Earth's surface by solar radiation drives a global atmospheric circulation that redistributes heat poleward. Cornish and Ives (2009) describe the three-cell model: the *Hadley cell* (equator to $\sim 30^\circ$ latitude), in which warm air rises at the Intertropical Convergence Zone (ITCZ) and descends in the subtropical high-pressure belt; the *Ferrel cell* ($\sim 30^\circ$–60°), an indirect, thermally driven cell maintained by eddy heat fluxes from migrating depressions; and the *Polar cell* ($\sim 60^\circ$–90°), where cold dense air descends at the poles and flows equatorward.

The Coriolis effect deflects the surface flow in each cell, producing the major wind belts: the northeast and southeast *trade winds* (Hadley cell), the *westerlies* in mid-latitudes (Ferrel cell), and the *polar easterlies*. The convergence zone between the Hadley cells—the ITCZ—migrates seasonally with the sun and is characterised by calms (*doldrums*), heavy convective rainfall, and squally thunderstorms, conditions of direct significance to mariners transiting tropical waters (Cornish & Ives, 2009).

3.3.3 Cyclones, Anticyclones, and Frontal Systems

Mid-latitude weather is dominated by *extratropical cyclones* (depressions) and *anticyclones*. Cornish and Ives (2009) describe the life cycle of a typical depression: it forms as a wave disturbance on the polar front (the boundary between warm tropical and cold polar air masses), deepens as the warm sector narrows, and eventually occludes when the cold front overtakes the warm front. The sequence of weather experienced by a ship as a depression passes depends on the vessel's position relative to the storm track.

A *warm front* produces a characteristic sequence as it approaches: high cirrus cloud gradually thickening to altostratus and then nimbostratus, with steady rain beginning well ahead of the surface front. After the warm front

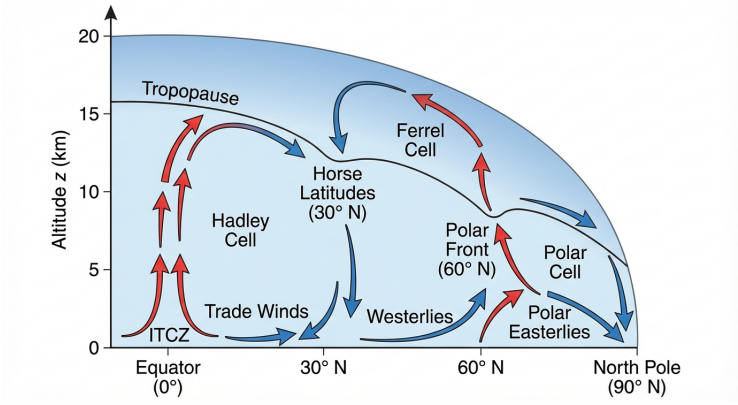

Figure 3.2: Three-cell model of global atmospheric circulation (Northern Hemisphere). The Hadley cell dominates equatorial to subtropical latitudes, the Ferrel cell occupies mid-latitudes, and the Polar cell extends to the poles. The Coriolis effect deflects surface winds to produce the trade winds, westerlies, and polar easterlies. Vertical arrows indicate rising motion at the ITCZ and polar front, and subsidence at the subtropical high and polar high.

passes, temperatures rise, winds veer, and conditions improve temporarily in the warm sector. The subsequent *cold front* is typically steeper, producing heavier but shorter-duration precipitation (often showery), a sharp temperature drop, and a backing then veering of the wind (Cornish & Ives, 2009).

In an *anticyclone*, descending air produces clear skies, light winds, and generally settled conditions. At sea, anticyclones are generally benign but may cause poor visibility through radiation fog in winter or advection fog in spring and summer when warm moist air flows over cold sea surfaces (Cornish & Ives, 2009).

3.3.4 Tropical Cyclones (Hurricanes/Typhoons)

Tropical cyclones (hurricanes, typhoons) are the most destructive weather systems encountered at sea. Cornish and Ives (2009) describe the conditions necessary for their formation: sea surface temperature exceeding $26.5\,^{\circ}\text{C}$ to a depth of at least 50 m, at a latitude greater than approximately 5° (to provide a sufficient Coriolis deflection), with pre-existing low-level convergence and weak vertical wind shear. The energy source is the latent heat released by condensation of moisture evaporated from the warm ocean surface.

The mature tropical cyclone has a characteristic structure: a central *eye* of calm, clear, warm descending air (15 km to 60 km in diameter), surrounded by the *eyewall* of the most intense winds and heaviest rainfall, and spiral *rainbands* extending hundreds of kilometres outward (Cornish & Ives, 2009). Wind

speeds in the eyewall can exceed $65\ \mathrm{m\ s^{-1}}$ (Category 5 on the Saffir–Simpson scale), and the central pressure may fall below $900\ \mathrm{hPa}$.

For mariners, the most critical concept is the *dangerous semicircle*. Cornish and Ives (2009) explain that in the Northern Hemisphere the right-hand semicircle (relative to the storm's direction of motion) is more dangerous because the storm's translational speed adds to the rotational wind speed, producing the highest winds. In the left-hand (*navigable*) semicircle, the translational speed opposes the rotational wind, giving relatively lower wind speeds and a tendency for vessels to be blown away from the storm track. Buys Ballot's law provides the operational rule: face the wind, and the centre of the low is approximately 90° to the right (in the Northern Hemisphere); if the wind veers, the vessel is in the dangerous semicircle (Cornish & Ives, 2009).

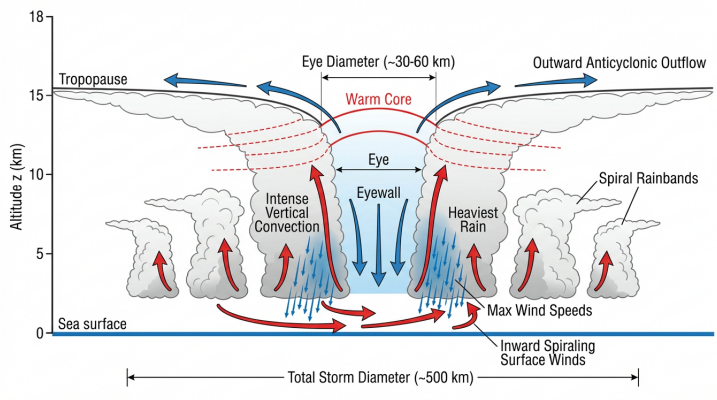

Figure 3.3: Vertical cross-section of a mature tropical cyclone showing the calm, warm eye surrounded by the eyewall of most intense winds and convection, with outer spiral rainbands. Low-level inflow converges toward the centre, rising rapidly in the eyewall, and diverges aloft. The dangerous semicircle (right of the storm track in the Northern Hemisphere) experiences the highest winds where translational and rotational components add.

3.3.5 Sea--Air Interaction

The ocean–atmosphere interface is the site of continuous exchange of heat, mass, and momentum (Gill, 1982). The three pathways of heat transfer from ocean to atmosphere are:

1. **Shortwave radiation:** Solar radiation absorbed by the ocean (governed by the diffuse attenuation coefficient K_d; see Chapter 2, Equation 2.13). The transmittance through the sea surface depends on cloud cover and solar elevation as described by Dera (1992, Eq. 5.2.16).

2. **Longwave radiation:** The ocean emits thermal infrared radiation as a near-blackbody. The net longwave flux depends on the sea surface temperature and the atmospheric greenhouse effect.

3. **Latent and sensible heat:** Evaporation transfers both mass (water vapour) and latent heat from the ocean to the atmosphere. Sensible heat is transferred by conduction and convection across the thin boundary layer at the surface.

The sea surface temperature (SST) is a key variable controlling these fluxes. The upper-ocean mixed layer temperature, maintained by turbulent mixing and wind forcing, determines the rate of evaporation and hence the latent heat flux. Regional SST anomalies (such as El Niño) can substantially alter atmospheric circulation patterns (Dera, 1992).

The turbulent exchange of heat and moisture across the air–sea interface is parameterised by the *bulk aerodynamic formulae*. Dera (1992) express the sensible and latent heat fluxes as:

$$Q_H = \rho_a \, c_p \, C_H \, U_{10} \, (T_s - T_a) \tag{3.7}$$

$$Q_E = \rho_a \, L_v \, C_E \, U_{10} \, (q_s - q_a) \tag{3.8}$$

where ρ_a is the air density, c_p is the specific heat of air, $L_v \approx 2.5 \times 10^6$ J kg^{-1} is the latent heat of vaporisation, U_{10} is the wind speed at 10 m height, T_s and T_a are the sea surface and air temperatures, q_s and q_a are the specific humidities at the surface and at 10 m, and C_H and C_E are the dimensionless bulk transfer coefficients for heat and moisture (Dera, 1992). Similarly, the wind stress on the sea surface is $\tau = \rho_a \, C_D \, U_{10}^2$, where C_D is the drag coefficient (Gill, 1982). Typical values over the open ocean are $C_D \approx (1.0\text{–}2.5) \times 10^{-3}$, increasing with wind speed and sea state, while $C_H \approx C_E \approx 1.1 \times 10^{-3}$ under near-neutral stability conditions (Gill, 1982).

The net heat flux at the sea surface is the sum of shortwave radiation gain, longwave radiation loss, and the turbulent sensible and latent fluxes. At mid-latitudes, the latent heat flux typically dominates, reflecting the enormous capacity of the ocean to supply moisture to the atmosphere through evaporation (Dera, 1992).

3.3.6 Visibility, Fog, and Precipitation Physics

Fog is a critical maritime hazard that reduces visibility below 1000 m. Cornish and Ives (2009) classify the principal types encountered at sea:

- **Advection fog:** Formed when warm, moist air passes over a colder sea surface. The air is cooled below its dew point from below, producing a shallow but persistent fog layer. This is the most common type of sea fog, particularly in spring and summer when warm continental air flows over cold ocean currents (e.g. the Labrador Current, the Oyashio) (Cornish & Ives, 2009).

- **Radiation fog:** Formed over land on clear, calm nights when radiative cooling reduces the near-surface temperature below the dew point. It may drift seaward in light offshore winds, affecting coastal waters (Cornish & Ives, 2009).

- **Frontal fog:** Occurs near warm fronts where rain from the overrunning warm air falls through the cooler air below, saturating it by evaporation. This type is transient, clearing as the front passes (Cornish & Ives, 2009).

Precipitation forms when cloud droplets grow large enough to fall against the updraft. The two principal growth mechanisms are the Bergeron–Findeisen (ice-crystal) process, dominant in mid-latitude clouds that extend above the freezing level, and the collision–coalescence process, dominant in warm tropical clouds. The type and intensity of precipitation are directly linked to the atmospheric stability and the vertical extent of the cloud (Cornish & Ives, 2009).

3.3.7 Sea State and Wind--Wave Relationship

The state of the sea surface is directly related to wind speed, duration, and fetch (the distance over which the wind blows). Cornish and Ives (2009) present the *Beaufort scale*, which classifies wind speeds from Force 0 (calm, $< 0.5\,\mathrm{m\,s^{-1}}$) to Force 12 (hurricane, $> 33\,\mathrm{m\,s^{-1}}$) and associates each level with characteristic sea conditions. At Force 8 (gale, $17\,\mathrm{m\,s^{-1}}$ to $21\,\mathrm{m\,s^{-1}}$), significant wave heights reach 5.5 m to 7.5 m; at Force 12, wave heights can exceed 14 m (Cornish & Ives, 2009).

The relationship between wind speed U_{10} (at $10\,\mathrm{m}$ height), wave height, and wave period in a *fully developed sea* (where the wave field has reached equilibrium with the wind) follows from the Pierson–Moskowitz spectrum. The significant wave height H_s in a fully developed sea grows approximately as $H_s \propto U_{10}^2$, while the peak period increases more gradually (Cornish & Ives, 2009). The Beaufort scale encapsulates these relationships in a form immediately usable by mariners for visual estimation of wind and sea conditions.

3.4 Applications in Maritime Systems

3.4.1 Weather Forecasting for Mariners

Maritime weather forecasting relies on the interpretation of *synoptic charts*, which depict the distribution of atmospheric pressure, frontal positions, and significant weather phenomena over large areas at a standard observation time. Isobars on a surface analysis chart indicate the pressure gradient and, through the geostrophic wind equation (Equation 3.6), the wind speed and direction; closely spaced isobars signal strong winds. Frontal symbols

mark the boundaries between air masses, and their movement and intensity indicate the expected sequence of weather (Cornish & Ives, 2009).

At sea, weather information is received from shore-based meteorological services via radiofacsimile charts, Navtex broadcasts (text-based coastal warnings), and digital gridded data files (GRIB format) that can be overlaid on electronic chart displays. National Geospatial-Intelligence Agency (2019) note that the mariner should cross-check forecast data with direct observations: barometric tendency (Section 3.2.3), wind direction shifts, cloud type progression, and sea state changes all provide immediate local indicators that may precede or contradict the synoptic forecast. Satellite imagery in the visible and infrared bands allows identification of cloud patterns associated with frontal systems, tropical cyclones, and fog banks, complementing the numerical forecast products (National Geospatial-Intelligence Agency, 2019).

3.4.2 Weather Routing

Weather routing (also termed *optimum track ship routing*) uses forecast wind, wave, and current data to determine the route that minimises transit time, fuel consumption, or cargo damage risk. National Geospatial-Intelligence Agency (2019) describe the general principle: the shortest geographic distance (great circle) is not necessarily the fastest or safest route, because adverse weather can slow a vessel far more than a longer but calmer alternative.

The standard analytical method is the *isochrone technique*: from the departure point, the maximum distance achievable in a fixed time interval (e.g. 12 hours) is computed for all headings, using the vessel's speed–sea-state performance envelope and the forecast wave field. The locus of these points forms the first *isochrone*; the process is repeated from each point on the isochrone, advancing the forecast, until the destination is reached. The optimum route is the track that reaches the destination on the earliest isochrone (National Geospatial-Intelligence Agency, 2019).

Three optimisation objectives are common: *minimum time* (fastest arrival, used when schedule compliance is paramount), *minimum fuel* (lowest total consumption, accepting a longer transit), and *minimum risk* (avoiding heavy weather that could cause structural damage, cargo shifting, or crew injury). In practice, the routing recommendation is constrained by the master's obligation to ensure the safety of the vessel and crew above all other considerations (National Geospatial-Intelligence Agency, 2019).

3.4.3 Heavy Weather Seamanship

When heavy weather cannot be avoided, the master must decide how to handle the vessel to minimise the risk of structural damage, loss of stability, and crew injury. Cornish and Ives (2009) describe three classical heavy-weather tactics:

- **Heaving-to:** The vessel maintains minimum steerage way with the bow approximately $30°$–$45°$ off the dominant wave direction, reducing the encounter frequency and preventing beam-on rolling. This tactic is suitable when sea room permits and the vessel has sufficient power to maintain headway against the seas.

- **Running before the sea:** The vessel turns to run downwind, reducing the relative wind and wave impact. The danger is that following seas may cause pooping (seas breaking over the stern) or broaching (loss of directional control in steep following seas), particularly when the vessel's speed approaches the wave phase speed.

- **Lying ahull:** All sail or engine power is removed and the vessel is left to find its own equilibrium attitude. This is a tactic of last resort for vessels unable to maintain steerage way, as the vessel will lie beam-on to the seas, exposing it to maximum rolling (Cornish & Ives, 2009).

For tropical cyclone avoidance, Cornish and Ives (2009) prescribe rules based on the dangerous semicircle concept (Section 3.3.4). In the Northern Hemisphere, a vessel in the dangerous (right) semicircle should bring the wind on the starboard bow and make best speed to open from the storm track. A vessel in the navigable (left) semicircle should bring the wind on the starboard quarter and run with the wind, diverging from the storm path. A vessel directly ahead of the storm should bring the wind on the starboard quarter and run to escape the storm's advance (Cornish & Ives, 2009; National Geospatial-Intelligence Agency, 2019).

3.4.4 Ice Accretion Physics

Ice accretion on ships is a serious stability hazard in high-latitude operations. Cornish and Ives (2009) describe two mechanisms: *spray icing*, caused by sea spray freezing on contact with the vessel's superstructure when the air temperature is below the freezing point of the spray (approximately $-2\,°\mathrm{C}$ for seawater); and *atmospheric icing*, caused by freezing rain, drizzle, or fog depositing ice on exposed surfaces.

Spray icing is the more dangerous mechanism because the spray flux is large and the accretion rate depends on wind speed and sea state: higher winds generate more spray and drive it higher into the superstructure. Cornish and Ives (2009) note that significant icing occurs when the air temperature falls below $-2\,°\mathrm{C}$ and the sea temperature is below $7\,°\mathrm{C}$, with the most severe icing at air temperatures below $-9\,°\mathrm{C}$ combined with wind speeds exceeding $15\,\mathrm{m\,s^{-1}}$ and significant wave heights above $3\,\mathrm{m}$.

The stability consequences of ice accretion are severe. Ice accumulated on decks, masts, rigging, and superstructure raises the vessel's centre of gravity, reducing the metacentric height GM and the righting lever GZ at all angles (see the stability analysis in the companion volume). Cornish and Ives (2009)

report that small fishing vessels are particularly vulnerable: an accumulation of 15 cm to 30 cm of ice on the superstructure can raise the centre of gravity sufficiently to cause capsizing. The prescribed countermeasures are manual removal of ice (chipping and steam lances) and, when possible, altering course to reduce spray generation—either by reducing speed or by steering to place the wind on the quarter rather than the bow (Cornish & Ives, 2009).

3.5 Discussion

The Coriolis effect (Equation 3.4) is the unifying physical mechanism that connects atmospheric and oceanic circulation (Gill, 1982). It deflects wind, drives geostrophic currents (Chapter 12), and is responsible for the large-scale patterns—trade winds, westerlies, and subtropical gyres—that define the oceanic and atmospheric environment in which ships operate. The sea–air interface acts as the coupling boundary, with solar radiation, latent heat, and wind stress as the principal exchange mechanisms (Dera, 1992).

The treatment of atmospheric lapse rates and stability by Cornish and Ives (2009) provides the thermodynamic foundation for understanding why weather events produce the patterns they do: conditionally unstable air leads to cumulonimbus development and convective precipitation, while absolutely stable air suppresses vertical motion and produces stratus clouds and drizzle. The geostrophic wind equation (Equation 3.6) quantifies the fundamental relationship between isobar spacing and wind speed, while Buys Ballot's law converts this physical relationship into an immediately actionable rule for mariners. The dangerous semicircle concept for tropical cyclones combines the Coriolis effect (Equation 3.4), the storm's translational velocity, and the surface wind field into a practical decision framework for storm avoidance (Cornish & Ives, 2009).

The coupling between ocean and atmosphere—parameterised by the bulk aerodynamic formulae (Equations 3.7–3.8) and the wind stress relation—means that the two fluids cannot be understood in isolation. Changes in sea surface temperature alter the heat and moisture fluxes, which modify atmospheric stability and circulation, which in turn change the wind stress and Ekman transport (Chapter 4, Equation 4.15), feeding back to the ocean thermal structure. Gill (1982) demonstrated that this coupling is fundamental to atmosphere–ocean dynamics at all scales, from the diurnal sea breeze to the planetary-scale thermohaline circulation. The continued improvement of coupled numerical weather prediction models, which solve the atmospheric and oceanic equations of motion simultaneously, has steadily extended the useful forecast horizon for maritime weather (Wallace & Hobbs, 2006).

3.6 Conclusion

The Coriolis acceleration $\mathbf{a}_C = 2\boldsymbol{\omega} \times \mathbf{v}$ (Equation 3.4) is the unifying mechanism of atmospheric and oceanic dynamics, deflecting winds, organising global circulation cells, and governing the geostrophic wind $V_g = (1/\rho f)(\Delta p/\Delta n)$ (Equation 3.6) that blows parallel to the isobars (Cornish & Ives, 2009; Dera, 1992). The vertical thermal structure of the atmosphere, characterised by the dry adiabatic lapse rate $\Gamma_d = g/c_p \approx 9.8\,^\circ\mathrm{C\,km^{-1}}$ (Equation 3.1) and the lower saturated rate ($4\,^\circ\mathrm{C\,km^{-1}}$ to $7\,^\circ\mathrm{C\,km^{-1}}$), determines atmospheric stability and thereby controls whether convective clouds, frontal precipitation, or clear skies prevail (Cornish & Ives, 2009). The three-cell model—Hadley, Ferrel, and Polar—explains the trade winds, westerlies, and polar easterlies, while the ITCZ migrates seasonally with the sun, producing the calm doldrums and squally thunderstorms of the tropics.

For mariners, the most operationally critical systems are the extratropical cyclone life cycle (warm front, cold front, occlusion), the tropical cyclone with its dangerous semicircle where translational and rotational winds add, and the fog types—advection, radiation, and frontal—that reduce visibility below 1000 m (Cornish & Ives, 2009). Tropical cyclones require sea surface temperatures exceeding $26.5\,^\circ$C and sufficient Coriolis deflection (latitude above $\sim 5^\circ$); Buys Ballot's law provides the operational rule for locating storm centres and identifying the dangerous semicircle. The Beaufort scale condenses the physics of wind–wave interaction into an observational framework from Force 0 (calm) to Force 12 (hurricane), enabling visual estimation of conditions at sea. At the air–sea interface, the continuous exchange of shortwave radiation, longwave emission, and latent and sensible heat fluxes couples the ocean thermal structure to atmospheric circulation, with sea surface temperature as the controlling variable (Dera, 1992).

References

Cornish, M. M., & Ives, E. E. (2009). *Reeds maritime meteorology* (3rd ed.). Adlard Coles Nautical.

Dera, J. (1992). *Marine physics* (P. Senn, Trans.) [Translated from Polish. Original: *Fizyka morza*, 1983]. Elsevier.

Fischer-Cripps, A. C. (2014). *The physics companion* (2nd ed.). CRC Press. https://doi.org/10.1201/b17356

Gill, A. E. (1982). *Atmosphere-ocean dynamics* (Vol. 30). Academic Press.

Holton, J. R., & Hakim, G. J. (2013). *An introduction to dynamic meteorology* (5th ed.). Academic Press. https://doi.org/10.1016/C2009-0-63394-8

National Geospatial-Intelligence Agency. (2019). *The American practical navigator (Bowditch)* [Bicentennial edition; originally published 1802 by Nathaniel Bowditch].

Wallace, J. M., & Hobbs, P. V. (2006). *Atmospheric science: An introductory survey* (2nd ed.). Academic Press.

Chapter 4

Physical Oceanography

4.1 Introduction

Physical oceanography is the study of the ocean as a physical system: its temperature and salinity distributions, density structure, currents, and the processes that drive them (Talley et al., 2011). For mariners, oceanographic knowledge directly affects navigational safety and efficiency; for marine scientists, the physical properties of seawater determine the propagation of light and sound, the distribution of marine life, and the exchanges of heat and momentum across the air–sea interface.

Dera (1992) provided a comprehensive account of the physical properties of seawater and the processes that shape the ocean environment. This chapter draws primarily on that work for the description of seawater composition, salinity, density, and vertical structure.

4.2 Scientific Background

4.2.1 Physical Properties of Seawater

Seawater is a multicomponent electrolyte solution whose thermodynamic state is determined by three independent variables: temperature T, salinity S, and pressure p (see the *Thermodynamics in Marine Engineering* chapter of the companion volume). The composition of dissolved salts in the open ocean is remarkably constant in relative proportions, a principle known as *Marcet's rule* or the *rule of constant composition*. This constancy makes it possible to characterise the total dissolved salt content by a single parameter—salinity.

The classical definition of salinity due to Knudsen relates it to the chlorinity Cl via (Dera, 1992, Eq. 2.4.1):

$$S = 1.805\,\mathrm{Cl} + 0.030 \quad [‰] \tag{4.1}$$

This was refined by the Joint Panel on Oceanographic Tables and Standards

to (Dera, 1992, Eq. 2.4.3):

$$S = 1.80655\,\mathrm{Cl} \tag{4.2}$$

Modern practice replaces chemical chlorinity titration with in situ conductivity measurements. The Practical Salinity Scale 1978 (PSS-78) defines salinity as a dimensionless ratio of conductivities (Dera, 1992, Eq. 2.5.8):

Equation 12.3 — Practical salinity (PSS-78):

$$S = \sum_{i=0}^{5} a_i \, K_{15}^{i/2} \tag{4.3}$$

where K_{15} is the ratio of the in situ conductivity to the conductivity of standard KCl solution at $15\,^{\circ}\mathrm{C}$, and the coefficients a_i are defined by the UNESCO polynomial (Dera, 1992, Eqs. 2.5.8–2.5.10). Temperature and pressure corrections extend this formula to arbitrary conditions. The PSS-78 system eliminated the need for chemical analysis and enabled routine CTD (conductivity–temperature–depth) profiling.

The conductivity of seawater arises from the migration of dissolved ions under an applied electric field. The ionic drift velocity is $v = \mu E_e$, where μ is the ion mobility and E_e is the electric field strength, leading to Ohm's law in the form (Dera, 1992, Eqs. 2.5.1–2.5.2):

$$j = \gamma_e E_e \tag{4.4}$$

where j is the current density and γ_e is the specific electrical conductivity, given by (Dera, 1992, Eq. 2.5.3):

$$\gamma_e = F_a \, C \, (\mu^{+} + \mu^{-}) \tag{4.5}$$

with F_a the Faraday constant, C the molar concentration, and μ^{+}, μ^{-} the cation and anion mobilities respectively.

4.2.2 Temperature and Salinity Distribution

The vertical structure of the ocean is characterised by three principal layers (Talley et al., 2011). The *mixed layer* extends from the surface to a depth of approximately 20–200 m, depending on wind forcing and season, and has nearly uniform temperature and salinity due to turbulent mixing. Below the mixed layer lies the *thermocline*—a zone of rapidly decreasing temperature extending to approximately 1000 m depth. The *deep ocean* below the thermocline is cold (1–$4\,^{\circ}\mathrm{C}$) and nearly isothermal (Dera, 1992).

The vertical stability of the water column—its resistance to overturning—is governed by the vertical density gradient. Dera (1992) expressed this through the Brunt–Väisälä frequency:

Equation 12.6 — Brunt–Väisälä frequency:

$$N^2 = -\frac{g}{\rho}\,\frac{\mathrm{d}\rho}{\mathrm{d}z} \tag{4.6}$$

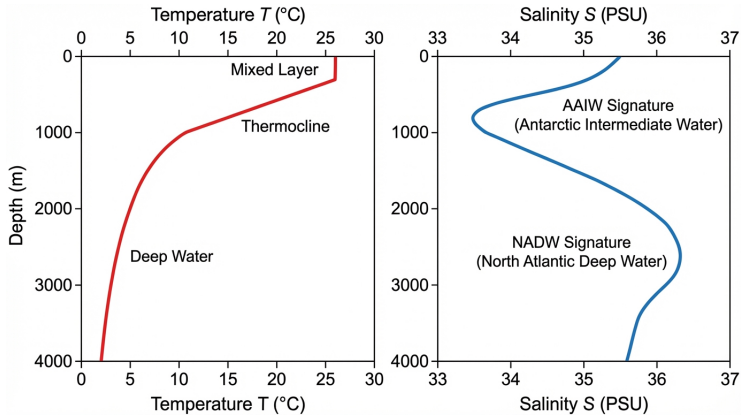

Figure 4.1: Vertical ocean structure showing typical temperature and salinity profiles. The mixed layer (approximately 0–100 m) is nearly uniform due to wind-driven turbulent mixing. The thermocline (100–1000 m) exhibits a rapid temperature decrease with depth, while the deep ocean below 1000 m is cold and nearly isothermal. The salinity profile shows the corresponding halocline where salinity gradients are largest.

where g is gravitational acceleration, ρ is density, and z is the vertical coordinate (positive upward). When $N^2 > 0$, the water column is stably stratified; when $N^2 < 0$, it is unstable and convective overturning occurs (Dera, 1992, Eq. 1.2.27); for a concise treatment, see (Fischer-Cripps, 2014). The pycnocline—the zone of maximum density gradient—coincides broadly with the thermocline in most of the ocean.

4.2.3 Light and Sound in the Ocean

The penetration of light into the ocean governs primary productivity, heat absorption, and defines the photic zone. The downward irradiance decreases exponentially with depth according to (Dera, 1992, Eq. 5.4.16):

$$E_{\downarrow}(z) = E_{\downarrow}(0)\, e^{-K_d z} \tag{4.7}$$

where K_d is the diffuse attenuation coefficient. The depth at which irradiance falls to 1% of the surface value defines the base of the euphotic zone. For the clearest open ocean (Jerlov type I), this depth reaches approximately 140 m at the wavelength of maximum transparency ($\lambda \approx 475$ nm), while for turbid coastal waters (type 5) it may be as shallow as 10 m (Dera, 1992). A detailed treatment of the optical properties of seawater is given in Chapter 2.

The speed of sound in the ocean increases with temperature, salinity, and pressure (Chapter 6). The resulting vertical sound speed profile typically exhibits a minimum at 400–1200 m depth, forming the SOFAR channel that enables long-range acoustic propagation (Dera, 1992).

4.3 Theoretical Framework

4.3.1 Ocean Currents and Circulation

The large-scale circulation of the ocean is driven by wind stress at the surface and density differences in the interior (Gill, 1982). Both are modulated by the Earth's rotation through the Coriolis effect. The Coriolis acceleration for a fluid parcel moving with velocity $\mathbf{v}$ at latitude φ is (Dera, 1992, Eq. 1.2.31):

Equation 12.8 — Coriolis acceleration:

$$\mathbf{a}_C = 2\,\boldsymbol{\omega} \times \mathbf{v} \tag{4.8}$$

where $\boldsymbol{\omega}$ is the angular velocity of the Earth ($\omega = 7.292 \times 10^{-5}\,\mathrm{rad\,s^{-1}}$). For horizontal motion, the dominant vertical component of the Coriolis force acts perpendicular to the velocity with magnitude $f = 2\omega \sin\varphi$, where f is the Coriolis parameter (Dera, 1992, Eq. 1.2.33).

The complete equation of motion for ocean water, including the Coriolis force, pressure gradient, gravity, and friction, is (Dera, 1992, Eq. 1.2.44):

Equation 12.9 — Equation of motion for ocean water:

$$\rho \left[\frac{\partial \mathbf{v}}{\partial t} + (\mathbf{v} \cdot \nabla)\mathbf{v} + 2\,\boldsymbol{\omega} \times \mathbf{v} \right] = -\nabla p + \eta\,\nabla^2 \mathbf{v} + \rho\,\mathbf{g} + \mathbf{F}_i \tag{4.9}$$

where η is the dynamic viscosity, ∇p the pressure gradient, $\rho\,\mathbf{g}$ the gravitational body force, and $\mathbf{F}_i$ represents additional external forces (Dera, 1992). This equation is the oceanic form of the Navier–Stokes equation and is the starting point for all circulation theory.

Ekman Layer Dynamics

The direct response of the ocean to wind stress occurs within a thin surface boundary layer known as the *Ekman layer* (Cushman-Roisin & Beckers, 2011). Apel (1988) derives the Ekman layer structure from the linearised, incompressible momentum equations with constant vertical eddy viscosity A_v:

$$\frac{\partial u}{\partial t} - f v = -\frac{1}{\rho}\frac{\partial p'}{\partial x} + \frac{A_v}{\rho}\frac{\partial^2 u}{\partial z^2} \tag{4.10}$$

$$\frac{\partial v}{\partial t} + f u = -\frac{1}{\rho}\frac{\partial p'}{\partial y} + \frac{A_v}{\rho}\frac{\partial^2 v}{\partial z^2} \tag{4.11}$$

where $f = 2\omega\sin\varphi$ is the Coriolis parameter, p' is the perturbation pressure, and A_v is the vertical eddy viscosity (Apel, 1988, Eqs. 6.2–6.3).

In the steady state, the balance between Coriolis force and eddy friction within the boundary layer yields solutions of the form (Apel, 1988, Eqs. 6.11–

6.12):

$$u(z) = u_g \left[1 - e^{-z/\delta_E} \cos\left(\frac{z}{\delta_E} \right) \right] \tag{4.12}$$

$$v(z) = u_g \, e^{-z/\delta_E} \sin\left(\frac{z}{\delta_E} \right) \tag{4.13}$$

where u_g is the geostrophic interior velocity and δ_E is the *Ekman layer thickness*:

Equation 12.14 — Ekman layer thickness:

$$\delta_E = \sqrt{\frac{2A_v}{f}} \tag{4.14}$$

The velocity vector rotates and attenuates exponentially with depth, tracing the characteristic *Ekman spiral*: at the surface, the drift velocity is directed at approximately $45°$ to the right of the wind (in the Northern Hemisphere), and it gradually veers and diminishes until merging with the geostrophic interior flow at a depth of several δ_E (Apel, 1988). For typical oceanic values of $A_v \approx 10^{-2}\,\mathrm{m^2\,s^{-1}}$ and mid-latitude $f \approx 10^{-4}\,\mathrm{s^{-1}}$, the surface Ekman layer thickness is $\delta_E \approx 20\text{–}40\,\mathrm{m}$, approximately coinciding with the mixed layer depth (Apel, 1988).

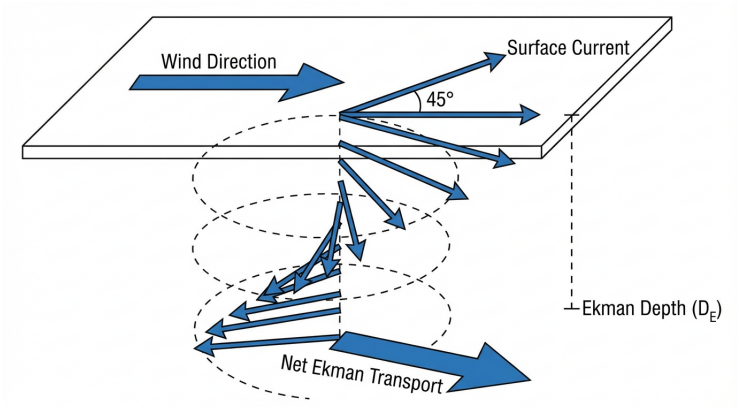

Figure 4.2: The Ekman spiral in the Northern Hemisphere. Current vectors (blue arrows) rotate clockwise and decay exponentially with depth, traced at intervals of the Ekman depth $\delta_E = \sqrt{2A_v/f}$ (Equation 4.14). The surface current is directed approximately $45°$ to the right of the wind. The depth-integrated net Ekman transport (red arrow) is directed $90°$ to the right of the wind (Equation 4.15).

Ekman Transport

A result of fundamental importance in physical oceanography is the depth-integrated mass transport within the Ekman layer. Vertically integrating the

steady-state momentum equations and applying the surface stress boundary condition yields the *Ekman transport* per unit width (Apel, 1988, Eqs. 6.22a–b):

Equation 12.15 — Ekman transport:

$$M_{xE} = \frac{\tau_y}{f}, \qquad M_{yE} = -\frac{\tau_x}{f} \tag{4.15}$$

where τ_x and τ_y are the components of the surface wind stress. In vector form, $\mathbf{M}_E = \boldsymbol{\tau} \times \hat{\mathbf{k}}/f$, so that the net Ekman transport is directed at $90°$ to the right of the wind in the Northern Hemisphere (Apel, 1988). This transport is independent of the eddy viscosity and depends only on the wind stress and the Coriolis parameter—a remarkable result first obtained by Ekman (1905), as cited in Apel (1988).

The Ekman transport drives surface convergence in the subtropical gyres (producing downwelling) and surface divergence in equatorial and coastal upwelling regions. These convergence and divergence patterns are the essential link between the local wind forcing and the basin-scale circulation (Apel, 1988).

Sverdrup Balance and Interior Transport

The vertical velocity at the base of the Ekman layer, caused by convergence or divergence of the Ekman transport, drives the interior ocean circulation through conservation of potential vorticity. Apel (1988) shows that for the interior of the ocean, removed from boundary layers, the meridional mass transport per unit width is determined solely by the curl of the wind stress:

Equation 12.16 — Sverdrup transport:

$$M_y = \frac{1}{\beta}\left(\nabla \times \boldsymbol{\tau}\right)_z \tag{4.16}$$

where $\beta = \mathrm{d}f/\mathrm{d}y = (2\omega/R_E)\cos\varphi$ is the meridional gradient of the Coriolis parameter and R_E is the Earth's radius (Apel, 1988, Eq. 6.80). This is the *Sverdrup relation*: the interior oceanic meridional transport is established entirely by the horizontal derivatives of the surface wind stress. In the subtropical gyres, negative wind stress curl (anticyclonic wind pattern) drives an equatorward (southward, in the Northern Hemisphere) interior flow known as the Sverdrup transport (Apel, 1988).

Western Boundary Currents

The southward Sverdrup transport must be balanced by a return flow to satisfy mass continuity. This return flow is concentrated in a narrow, intense current along the western boundary of the ocean basin—a *western boundary current* (Apel, 1988). The reason for western intensification lies in the requirement for an overall vorticity balance across the gyre: the frictional dissipation needed

to close the vorticity budget can only be achieved in a narrow, high-velocity boundary layer on the western side (Apel, 1988).

The Gulf Stream (North Atlantic), the Kuroshio (North Pacific), the Agulhas Current (Indian Ocean), and the Brazil Current (South Atlantic) are prominent examples (Talley et al., 2011). Typical parameters for the Gulf Stream include a core velocity exceeding $2\,\mathrm{m\,s^{-1}}$, a volume transport of approximately 60×10^6 $\mathrm{m^3\,s^{-1}}$, a surface elevation difference of about $1\,\mathrm{m}$ across the front, and a characteristic width of approximately $50\,\mathrm{km}$. The level of no motion—below which the baroclinic velocity vanishes—is found at approximately $2000\,\mathrm{m}$ depth (Apel, 1988, Table 6.1).

4.3.2 Thermohaline Circulation

While the wind-driven circulation governs the upper ocean, the deep circulation is driven by density contrasts arising from differences in temperature and salinity between water masses formed at different latitudes. Stern (1975) provides the theoretical framework for understanding how these density differences generate mixing and overturning through the thermohaline convection process.

Double Diffusion and Salt Fingers

The molecular diffusivities of heat and salt in seawater are vastly different: the thermal diffusivity is $\kappa_T \approx 1.4 \times 10^{-7}\,\mathrm{m^2\,s^{-1}}$, whereas the salt diffusivity is $\kappa_S \approx 1.5 \times 10^{-9}\,\mathrm{m^2\,s^{-1}}$, giving a ratio $\kappa_S/\kappa_T \approx 1/100$ (Stern, 1975). This disparity produces a class of convective instabilities—termed *double diffusion*—that are absent in fluids with a single diffusing quantity (Stern, 1975).

Consider a resting ocean in which both temperature and salinity decrease with depth ($T_z > 0$, $S_z > 0$), but the overall density increases downward ($\beta S_z - \alpha T_z < 0$, where α is the thermal expansion coefficient and β the haline contraction coefficient), so that the fluid is statically stable. A small parcel displaced upward will, because $\kappa_T \gg \kappa_S$, rapidly equilibrate its temperature with the surroundings while retaining its lower salinity. The resulting salinity deficit makes the parcel buoyant, accelerating it further upward. This is the *salt finger instability* (Stern, 1975).

Stern (1975) showed that the critical condition for the onset of the thermohaline instability in a layer of depth H is governed by a modified Rayleigh number:

Equation 12.21 — Thermohaline instability criterion:

$$\frac{g H^4}{\nu}\left(\frac{\beta S_z}{\kappa_S} - \frac{\alpha T_z}{\kappa_T}\right) = \frac{27\pi^4}{4} \tag{4.17}$$

where g is gravitational acceleration and ν is kinematic viscosity (Stern, 1975). For a deep ocean (H large), the instability condition reduces to $\beta S_z/\kappa_S > \alpha T_z/\kappa_T$, which requires only that the stabilising salinity gradient

exceeds a threshold set by the diffusivity ratio—not that the overall density gradient be destabilising (Stern, 1975).

The characteristic horizontal width of the resulting salt fingers is determined by the wavenumber of maximum growth rate (Stern, 1975):

Equation 12.22 — Salt finger width scale:

$$k_{\max}^{-1} = \left(\frac{g \alpha T_z - g \beta S_z}{\nu \, \kappa_T} \right)^{-1/4} \tag{4.18}$$

For typical subtropical thermocline conditions, this yields finger widths of order $1\,\mathrm{cm}$, consistent with laboratory experiments and oceanic microstructure observations (Stern, 1975). The flux ratio between heat and salt transported by the fingers approaches $\alpha \overline{w'T'} / (\beta \overline{w'S'}) \to 1/2$ when the density ratio $N = \alpha T_z / (\beta S_z)$ is large (Stern, 1975). This preferential transport of salt relative to heat is the mechanism by which double diffusion systematically modifies the temperature–salinity relationship of ocean water masses over decadal timescales (Stern, 1975).

Oceanic Mixing Timescale and the Thermocline

Stern (1975) demonstrated that the oceanic mixing timescale is of order decades to centuries by a simple scaling argument: a basin of depth $H = 1000\,\mathrm{m}$ subject to surface evaporation of $1\,\mathrm{m/yr}$ requires several decades to re-establish the observed salinity contrast of $\Delta S \approx 1$ ‰ between the upper kilometre and the deep ocean, since $\Delta S / S_0 \approx \Delta H / H$ (Stern, 1975). This is two to three orders of magnitude longer than the atmospheric mixing time (approximately two weeks), reflecting the fundamental asymmetry between oceanic and atmospheric adjustment rates.

The vertical temperature structure of the ocean—the thermocline—is maintained by the balance between downward diffusion of heat and the upwelling of cold deep water. Stern (1975) analysed the thermocline scaling for a differentially heated basin (warm at one end, cold at the other) and showed that the thermocline depth h scales with the Rayleigh number:

Equation 12.23 — Thermocline Rayleigh number:

$$Ra = \frac{g \, \alpha \, \Delta T \, L^3}{\kappa_T \, \nu} \tag{4.19}$$

where ΔT is the horizontal temperature difference and L is the basin width (Stern, 1975). In the high-Rayleigh-number regime appropriate to the ocean ($Ra \gg 1$), the thermocline depth becomes a small fraction of the total depth, with cold water filling the abyss beneath a thin warm surface layer—precisely the three-layer vertical structure (mixed layer, thermocline, deep ocean) described in Section 4.2.2 (Stern, 1975).

Conservation of Potential Vorticity and the Sverdrup Interior

The theoretical connection between wind forcing and interior ocean circulation rests on the conservation of potential vorticity. Stern (1975) derived the Sverdrup relation by showing that the downward Ekman suction velocity w_e caused by wind stress curl compresses the water column beneath the turbulent boundary layer. Conservation of potential vorticity requires that this compression be compensated by an equatorward movement of the column (towards decreasing f), yielding (Stern, 1975):

Equation 12.24 — Sverdrup transport (detailed form):

$$v\,h = -\frac{f}{\beta}\,\frac{\partial}{\partial y}\left(\frac{\tau}{f}\right) = -\beta^{-1}\,\frac{\partial \tau}{\partial y} + \frac{\tau}{f} \tag{4.20}$$

where v is the meridional velocity beneath the Ekman layer, h is the upper-layer thickness, $\tau(y)$ is the zonal wind stress, and $\beta = \mathrm{d}f/\mathrm{d}y$ (Stern, 1975). This result decomposes the total meridional transport into the Sverdrup interior component and the Ekman component (cf. Equation 4.15), confirming that the basin-scale circulation is set by the curl of the wind stress, with the return flow concentrated in an intense western boundary current required by vorticity balance (Cushman-Roisin & Beckers, 2011; Stern, 1975).

4.3.3 Tidal Physics

Tides are the periodic rise and fall of sea level caused by the gravitational attraction of the Moon and Sun on the Earth's ocean. The physics of tidal forcing was placed on a rigorous mathematical foundation through the concept of the *tide-generating potential*.

Tide-Generating Potential

Apel (1988) derives the tidal potential by resolving the gravitational and centrifugal forces acting on a unit mass of ocean water at the Earth's surface. At a point P with spherical coordinates (r, θ, ϕ), the tidal potential due to an astronomical body j (Moon or Sun) at distance R_j from the Earth's centre is (Apel, 1988, Eq. 5.123):

Equation 12.17 — Tide-generating potential:

$$\Phi_{tj}(r, \gamma) = \Phi_{0j}\left(\frac{r}{R_j}\right)^2 \frac{1}{2}\left(3\cos^2\gamma - 1\right) \tag{4.21}$$

where $\Phi_{0j} = -Gm_j/R_j$ is the mean geopotential at distance R_j, G is the gravitational constant, m_j is the mass of the attracting body, and γ is the angle between the directions from the Earth's centre to the point P and to the astronomical body (Apel, 1988). The ratio of the lunar to solar tidal forcing is $\Phi_{0m}R_s/(\Phi_{0s}R_m) \approx 2.18$, confirming the Moon's dominant role in tide generation (Apel, 1988).

Tidal Species and Constituents

By expressing $\cos\gamma$ in terms of the declination and hour angle of the astronomical body, the tidal potential separates into three distinct frequency groupings called *tidal species* (Apel, 1988, Eq. 5.125):

- **Semidiurnal** ($\nu = 2$): oscillations with periods near 12 h, with a latitude factor $\sin^2\theta$, maximum at the equator.
- **Diurnal** ($\nu = 1$): oscillations with periods near 24 h, with a latitude factor $\sin 2\theta$, maximum at $\theta = 45°$.
- **Long-period** ($\nu = 0$): oscillations at fortnightly to annual periods from variations in the lunar and solar declinations.

The frequency of any tidal constituent can be expressed as a linear combination of six fundamental astronomical frequencies using the *Doodson numbers* n_d (Apel, 1988, Eq. 5.126):

$$\omega_i = n_1\omega_l + n_2\omega_m + n_3\omega_y + n_4\omega_p + n_5\omega_n + n_6\omega_{p'} \tag{4.22}$$

where ω_l, ω_m, ω_y correspond to the lunar day, lunar sidereal month, and tropical year, respectively, and ω_p, ω_n, $\omega_{p'}$ arise from orbital variations with periods of 8.84, 18.6, and $20{,}940$ years (Apel, 1988). Up to 400 distinct tidal constituents have been identified, but the dominant ones are few. The principal lunar semidiurnal constituent M_2 has a period of 12.421 h and an equilibrium amplitude of 0.242 m; the principal solar semidiurnal constituent S_2 has a period of 12.000 h and an equilibrium amplitude of 0.113 m (Apel, 1988, Table 5.1).

Spring and Neap Tides

When the Moon and Sun are aligned (new and full Moon), their tidal forces add constructively, producing the larger *spring tides*. When they are at right angles (first and third quarter), the forces partially cancel, producing the smaller *neap tides*. The ratio of spring to neap tidal range is approximately $(A_{M_2} + A_{S_2})/(A_{M_2} - A_{S_2}) \approx 2.7$ (Apel, 1988).

Dynamic Tide Theory

The equilibrium theory assumes the ocean response is instantaneous and global, but the actual ocean tides are governed by the shallow-water hydrodynamic equations forced by the tidal potential. Apel (1988) writes the linearised tidal equations in spherical coordinates as a forced shallow-water system (Apel, 1988, Eqs. 5.128–5.130), where the shallow-water phase speed $c_h = \sqrt{gH}$ (H being the ocean depth) limits the speed of tidal wave propagation to approximately 220 m s^{-1}—slower than the ~ 330 m s^{-1} speed at which the tidal forcing moves at mid-latitudes (Apel, 1988). This mismatch between forcing speed and natural wave speed means the oceanic tides

cannot follow the equilibrium prediction; instead, the response is organised around *amphidromic points*—nodes where the tidal amplitude is zero and around which the co-phase lines rotate. Each tidal constituent produces its own amphidromic system (Apel, 1988).

Local amplification of tides occurs when basin geometries produce near-resonant conditions. The Bay of Fundy (Canada), for example, has a natural oscillation period close to the M_2 semidiurnal period, resulting in tidal ranges exceeding 10 m. Frobisher Bay on Baffin Island exhibits similar resonant amplification (Apel, 1988).

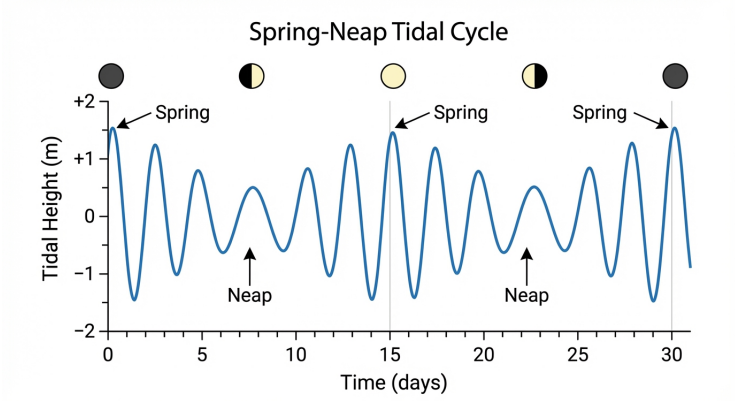

Figure 4.3: Spring–neap tidal cycle generated by the superposition of the principal lunar (M_2, period 12.421 h) and solar (S_2, period 12.000 h) semidiurnal constituents (Equation 4.21). Spring tides (maximum range) occur when the Moon and Sun are aligned; neap tides (minimum range) occur at quadrature. The dashed envelope shows the fortnightly modulation period of approximately 14.8 days.

4.3.4 Tidal Currents and Streams

The periodic rise and fall of tidal water levels (Section 4.3.3) is accompanied by horizontal water movements—*tidal currents*—whose spatial and temporal patterns depend on the local geometry of the coastline and seabed. Two fundamental types of tidal current are distinguished (National Geospatial-Intelligence Agency, 2019).

Reversing currents occur in confined waterways (straits, estuaries, harbour approaches) where the flood and ebb streams are constrained to flow along the channel axis, reversing direction approximately every half tidal period. The current speed varies approximately sinusoidally between zero (*slack water*) and a maximum that depends on the tidal range and the cross-sectional geometry of the channel. In such settings, the times of slack water and maximum current are the critical navigational data, because a vessel entering a narrow channel against a strong tidal stream may be unable to maintain

steerage way or may experience excessive fuel consumption (National Geospatial-Intelligence Agency, 2019).

Rotary currents occur in open water where there are no lateral boundaries to constrain the flow direction. The current vector rotates through all compass directions over a full tidal cycle, tracing an approximately elliptical path (the *current ellipse*). In the Northern Hemisphere, the rotation is typically clockwise for the semidiurnal constituents (Apel, 1988). The shape and orientation of the current ellipse depend on the relative magnitudes and phases of the tidal constituents, and the ellipse degenerates into a line (reversing current) when one constituent dominates in a laterally confined geometry (National Geospatial-Intelligence Agency, 2019).

Tidal current predictions are published by hydrographic authorities in the form of *tidal stream atlases* and *tidal diamonds* on navigational charts. A tidal diamond is a reference station at which the direction and rate of the tidal current are tabulated for each hour relative to the time of high water at a reference port. The navigator uses these tables in conjunction with the tide table predictions (Section 4.4.2) to estimate the set and drift of the current at any time during the tidal cycle, enabling computation of the course to steer and the estimated time of arrival (National Geospatial-Intelligence Agency, 2019).

4.3.5 Geostrophic Currents and Sea Surface Topography

In the ocean interior, away from the Ekman boundary layers, the dominant balance in the horizontal momentum equations is between the Coriolis force and the pressure gradient force. This is the *geostrophic balance*, identical in principle to the atmospheric case (Chapter 3) (Gill, 1982). Apel (1988) shows that the geostrophic velocity components are:

$$u_g = -\frac{1}{\rho f}\frac{\partial p}{\partial y} = -\frac{g}{f}\frac{\partial \zeta}{\partial y} \tag{4.23}$$

$$v_g = \frac{1}{\rho f}\frac{\partial p}{\partial x} = \frac{g}{f}\frac{\partial \zeta}{\partial x} \tag{4.24}$$

where ζ is the sea surface elevation (Apel, 1988, Eqs. 3.85–3.86). The sea surface is not exactly level; it has a topography—called the *dynamic topography*—maintained by the wind-driven and thermohaline circulation. The slope of the dynamic topography is directly proportional to the surface geostrophic current velocity.

For the Gulf Stream, the sea surface elevation difference across the current front is approximately $\zeta_0 \approx 1\,\text{m}$ over a transverse scale of $\ell \approx 50\,\text{km}$, giving a surface slope of order 10^{-5} (Apel, 1988, Table 6.1). This slope, though minute, sustains the intense western boundary current through geostrophic balance. Below the surface, the velocity is inferred from the slope of isopycnal (constant density) surfaces relative to isobars—the *dynamic method*—which remains a standard technique for determining geostrophic current profiles. Typical subsurface isopycnal slopes in the Gulf Stream are of order 5×10^{-3} (Apel,

1988). Satellite altimetry now provides direct measurements of the absolute dynamic topography with centimetre-level precision, enabling global monitoring of geostrophic surface currents.

4.3.6 Upwelling and Downwelling

The convergence and divergence of Ekman transport (Equation 4.15) directly produce vertical motions in the water column. Apel (1988) describes two principal mechanisms:

Coastal upwelling occurs when wind blows parallel to a coastline with the coast on the left (in the Northern Hemisphere). The Ekman transport is directed offshore, and mass conservation requires cold, nutrient-rich subsurface water to rise and replace the water transported away. This mechanism is responsible for the major eastern boundary upwelling systems (California, Peru/Chile, Canary, Benguela), which support some of the world's most productive fisheries (Apel, 1988).

Ekman pumping is the vertical velocity induced at the base of the Ekman layer by spatial gradients in the wind stress. In the subtropical gyres, the anticyclonic wind pattern produces Ekman convergence and *downwelling* (Ekman pumping into the ocean interior), which depresses the thermocline and creates the warm, deep lens of water characteristic of the gyre centres. Conversely, cyclonic wind stress curl in the subpolar gyres produces Ekman *suction* (upwelling) (Apel, 1988). The vertical Ekman pumping velocity w_E at the base of the surface Ekman layer is given by the divergence of the Ekman transport (Apel, 1988):

Equation 12.25 — Ekman pumping velocity:

$$w_E = \frac{1}{\rho} \nabla \times \left(\frac{\boldsymbol{\tau}}{f} \right) \approx \frac{1}{\rho f} \left(\nabla \times \boldsymbol{\tau} \right)_z \tag{4.25}$$

where the approximation holds when β-effects on the Ekman transport are neglected. This Ekman pumping velocity links the surface wind forcing to the interior Sverdrup transport (Equation 4.16) and is the fundamental dynamical connection between atmospheric forcing and oceanic circulation (Apel, 1988).

4.4 Applications in Maritime Systems

4.4.1 Ocean Currents and Ship Routing

The western boundary currents described in Section 4.3.1—the Gulf Stream, Kuroshio, Agulhas, and Brazil currents—represent the most energetic features of the surface ocean circulation and have direct consequences for ship routing. A vessel sailing from the eastern seaboard of the United States to Europe can gain a speed advantage of 1–$2\ \mathrm{m\ s^{-1}}$ by riding within the Gulf Stream core,

whereas a westbound crossing must route south of the stream to avoid opposing currents exceeding $2\ \mathrm{m\ s^{-1}}$ (Apel, 1988).

The Sverdrup transport theory (Equation 4.16) and the geostrophic balance (Equations 4.23–4.24) provide the physical basis for these current patterns. In practice, operational ship routing services combine satellite altimetry (from which geostrophic surface currents are derived via the dynamic topography slope), global ocean circulation forecasts, and weather routing algorithms to select the minimum-time or minimum-fuel track. National Geospatial-Intelligence Agency (2019) emphasises that knowledge of major ocean current systems determines effective voyage planning: favourable currents reduce transit time and fuel consumption, whereas adverse currents increase both. This principle extends to the equatorial current systems—the North and South Equatorial Currents (westward) and the Equatorial Countercurrent (eastward)—which affect trans-Pacific and trans-Indian-Ocean routing (Talley et al., 2011).

The Ekman transport (Equation 4.15) also has operational relevance in coastal navigation: alongshore winds drive surface water offshore (or onshore), and the navigator must account for the resulting set when making coastal passages. In upwelling regions (Section 4.3.6), the offshore Ekman transport is accompanied by cold, nutrient-rich water at the surface, which can be detected by sea surface temperature measurements and serves as an indicator of the current regime (Apel, 1988).

4.4.2 Tidal Navigation

The prediction of tides at any location and time is achieved by *harmonic analysis*: the observed tidal record is decomposed into a sum of sinusoidal constituents (each characterised by a known astronomical frequency, Equation 4.22) with empirically determined amplitudes and phases. The predicted tide height at time t is then (Apel, 1988):

$$\zeta(t) = Z_0 + \sum_{n=1}^{N} A_n \cos\!\left(\omega_n\, t - \phi_n\right) \tag{4.26}$$

where Z_0 is the mean water level, A_n and ϕ_n are the amplitude and phase of the nth constituent, and ω_n is its angular frequency determined from the Doodson classification (Apel, 1988). This harmonic method, with typically 30–60 constituents, forms the basis of the published *tide tables* issued by national hydrographic offices (National Geospatial-Intelligence Agency, 2019).

The navigator uses tide table predictions to compute the *under-keel clearance* (UKC)—the vertical distance between the vessel's keel and the seabed—at all points along the intended route. The predicted water depth at time t is the sum of the charted depth (referenced to chart datum, usually the lowest astronomical tide, LAT) and the tidal height $\zeta(t)$. The UKC is then (National

Geospatial-Intelligence Agency, 2019):

$$\text{UKC} = d_{\text{chart}} + \zeta(t) - T_{\text{ship}}$$

where d_{chart} is the charted depth and T_{ship} is the static draft of the vessel, corrected for squat (speed-dependent sinkage), heel, and density effects (Section 4.4.3). Port authorities specify minimum UKC requirements, typically 10–15% of the vessel's draft for deep-draught vessels, and entry into shallow-water ports is restricted to *tidal windows*—periods when the predicted tide provides sufficient depth for safe passage (National Geospatial-Intelligence Agency, 2019).

The accuracy of harmonic tide predictions is limited by meteorological effects (storm surge, atmospheric pressure anomalies) and river discharge, which can cause the observed water level to deviate from the predicted astronomical tide by 0.5–2 m during extreme weather events. Real-time tide gauge data and weather surge forecasts are therefore used to supplement the harmonic predictions for critical port approach operations (National Geospatial-Intelligence Agency, 2019).

4.4.3 Density Effects on Ship Draft and Stability

The density of seawater varies with temperature, salinity, and pressure (see the *Thermodynamics in Marine Engineering* chapter of the companion volume), and this variation has direct operational significance for ships. When a vessel transits from oceanic water ($S \approx 35\,‰$, $\rho \approx 1025\,\text{kg m}^{-3}$) to fresh water ($\rho \approx 1000\,\text{kg m}^{-3}$), the reduction in buoyancy causes an increase in draft known as the *fresh water allowance*. The EOS-80 equation of state, derived in the companion volume, provides the quantitative basis for computing this effect.

Conversely, in hypersaline environments (e.g. the Suez Canal, the Red Sea, or tropical ports), seawater density may exceed $1030\,\text{kg m}^{-3}$, reducing the vessel's draft. Accurate density data from CTD measurements and the Practical Salinity Scale (Equation 4.3) are essential for computing under-keel clearances (Dera, 1992).

4.4.4 Ice Physics and Polar Navigation

Sea ice forms when the surface temperature of the ocean falls to the freezing point, which for seawater of salinity 35 ‰ is approximately $-1.8\,^{\circ}\text{C}$ (Cornish & Ives, 2009). The formation process begins with *frazil ice*—small needle-like crystals suspended in the water column—which coalesce into *grease ice* (a soupy layer) and then into *pancake ice* (circular discs 0.3 m to 3 m in diameter with raised rims formed by collisions). Under calm conditions, pancakes freeze together into *nilas*—a thin, elastic sheet that bends with the swell. Continued growth thickens the ice into *young ice* (10 cm to 30 cm) and eventually *first-year ice* (>30 cm) (Cornish & Ives, 2009).

Fast ice is sea ice that has frozen to the coast or between grounded icebergs; it does not move with the wind or currents. *Pack ice* consists of floating ice driven by wind and ocean currents; its concentration is expressed as a fraction of the sea surface (tenths), with $10/10$ indicating complete coverage (Cornish & Ives, 2009). Multi-year ice that has survived at least one summer melt season is harder, less saline (as brine pockets gradually drain), and has a distinctive blue hue. It presents a greater hazard to navigation than first-year ice due to its greater strength (Cornish & Ives, 2009).

For vessels navigating in ice, the compressive strength of sea ice (of order $0.5\,\text{MPa}$ to $5\,\text{MPa}$ depending on temperature, salinity, and crystal structure) determines the resistance experienced by the hull and the ice loads on the ship's structure. Classification society ice class notations (e.g. Finnish–Swedish Ice Classes, IACS Polar Class) specify the minimum structural scantlings and engine power required for operation in various ice conditions (Cornish & Ives, 2009).

4.5 Discussion

The physical oceanographic framework presented in this chapter highlights the central role of the three state variables—temperature, salinity, and pressure—in determining the behaviour of the ocean. Through the equation of state (Chapter 8), these variables control density, which in turn governs vertical stability (Equation 4.6), circulation (Equation 4.9), light penetration (Equation 4.7), and sound propagation (Chapter 14). The salinity measurement system has evolved from chemical titration (Equations 4.1–4.2) to the conductivity-based PSS-78 (Equation 4.3), enabling routine high-resolution profiling.

The Ekman layer theory (Apel, 1988) provides the essential dynamical link between atmospheric forcing and oceanic response. The result that the depth-integrated Ekman transport is directed at $90°$ to the wind (Equation 4.15) and is independent of the eddy viscosity is both elegant and practically powerful: it means the net wind-driven transport can be computed from wind stress observations alone, without requiring knowledge of the turbulent mixing processes within the boundary layer. The Sverdrup relation (Equation 4.16) extends this insight to the ocean interior, showing that the meridional transport is determined entirely by the wind stress curl. Together, Ekman transport and Sverdrup balance constitute the basis of wind-driven circulation theory.

The tidal physics framework (Apel, 1988) demonstrates that the oceanic tides are far more complex than the simple bulge model of equilibrium theory. The expansion of the tide-generating potential into hundreds of constituents (Equation 4.22), the formation of amphidromic systems, and the resonant amplification of tides in semi-enclosed basins all illustrate the rich dynamics that arise when a periodic forcing function acts on a bounded, rotating, stratified fluid.

The thermohaline convection theory of Stern (1975) completes the circulation framework by explaining the physics of deep ocean mixing. While the Ekman–Sverdrup theory (Equations 4.14–4.16) governs the wind-driven upper circulation, it is the double-diffusive instability (Equation 4.17) that drives the slow vertical mixing of heat and salt through the thermocline. The salt finger mechanism—arising from the hundredfold difference between thermal and haline diffusivities—demonstrates that a statically stable water column can nevertheless be convectively unstable, a result with no analogue in single-component fluids. The thermocline scaling (Equation 4.19) connects the observed vertical temperature structure to the basin-scale Rayleigh number, providing a first-principles explanation for why the deep ocean is cold and nearly isothermal while the warm layer is confined to the upper few hundred metres. The derivation of the Sverdrup relation from potential vorticity conservation (Equation 4.20) connects the wind-forced Ekman layer to the geostrophic interior, completing the theoretical chain from atmospheric forcing to basin-scale circulation (Stern, 1975).

The observational framework underpinning physical oceanography has expanded significantly beyond the ship-based hydrographic surveys that produced the classical water mass descriptions. Talley et al. (2011) describe how the modern ocean observing system combines satellite remote sensing (altimetry for sea surface height, scatterometry for wind stress, radiometry for sea surface temperature and salinity), autonomous profiling floats (the Argo array, providing temperature and salinity profiles to $2000\,\mathrm{m}$ depth across the global ocean), and moored and drifting buoys. These observation systems provide the spatial and temporal coverage needed to validate the Ekman–Sverdrup circulation theory (Equations 4.14–4.16) and to monitor the thermohaline circulation at basin scales (Talley et al., 2011).

The sea ice formation sequence described by Cornish and Ives (2009)—from frazil through grease, pancake, nilas, and first-year ice to multi-year pack—demonstrates how the thermodynamics of phase change, the salinity-dependent freezing point (see the *Thermodynamics in Marine Engineering* chapter of the companion volume), and the mechanical forcing of wind and waves together govern the ice environment that polar-navigating vessels encounter. The compressive strength of sea ice introduces a structural loading regime entirely absent from temperate-water operations, requiring specific ice class structural reinforcement and propulsion power.

4.6 Conclusion

The ocean's physical behaviour is governed by the interplay of three state variables—temperature, salinity, and pressure—through the equation of state (see the *Thermodynamics in Marine Engineering* chapter of the companion volume). Salinity, operationally defined by the conductivity-based Practical Salinity Scale 1978 (Equation 4.3), replaces the older chemical chlorinity

method (Dera, 1992). The Brunt–Väisälä frequency $N^2 = -(g/\rho)\,\mathrm{d}\rho/\mathrm{d}z$ (Equation 4.6) measures the vertical stability of the water column, while the three-layer vertical structure—mixed layer, thermocline, and deep ocean—is maintained by the competition between wind-driven turbulent mixing and the thermocline-scale Rayleigh-number balance (Equation 4.19) (Dera, 1992; Stern, 1975). The thermohaline instability criterion (Equation 4.17) demonstrates that a statically stable column can be convectively unstable when $\beta S_z/\kappa_S > \alpha T_z/\kappa_T$, producing salt fingers of centimetre-scale width (Equation 4.18) that drive the slow vertical mixing on decadal timescales (Stern, 1975).

Wind-driven circulation rests on the Ekman–Sverdrup framework: the Ekman spiral (Equations 4.12–4.13) describes the rotation and exponential decay of current with depth within a boundary layer of thickness $\delta_E = \sqrt{2A_v/f}$ (Equation 4.14), and the depth-integrated Ekman transport is directed 90° to the right of the wind in the Northern Hemisphere (Equation 4.15) (Apel, 1988). The Sverdrup relation $M_y = (1/\beta)(\nabla \times \boldsymbol{\tau})_z$ (Equation 4.16) establishes that interior meridional transport is determined entirely by the wind stress curl, with the return flow concentrated in intense western boundary currents (Gulf Stream, Kuroshio) required by vorticity balance (Apel, 1988; Stern, 1975). Tidal dynamics add a periodic forcing described by the tide-generating potential (Equation 4.21), whose expansion into hundreds of constituents (Equation 4.22) produces the observed amphidromic systems and the spring–neap modulation governed by the dominant M_2 and S_2 harmonics (Apel, 1988). The geostrophic balance (Equations 4.23–4.24) relates sea surface slope to current velocity, while operational consequences—fresh water allowance, under-keel clearance, and the ice formation sequence from frazil through multi-year pack (Cornish & Ives, 2009)—translate the underlying physics into direct maritime significance.

References

Apel, J. R. (1988). *Principles of ocean physics* (Vol. 38). Academic Press.

Cornish, M. M., & Ives, E. E. (2009). *Reeds maritime meteorology* (3rd ed.). Adlard Coles Nautical.

Cushman-Roisin, B., & Beckers, J.-M. (2011). *Introduction to geophysical fluid dynamics: Physical and numerical aspects* (2nd ed.). Academic Press.

Dera, J. (1992). *Marine physics* (P. Senn, Trans.) [Translated from Polish. Original: *Fizyka morza*, 1983]. Elsevier.

Fischer-Cripps, A. C. (2014). *The physics companion* (2nd ed.). CRC Press. https://doi.org/10.1201/b17356

Gill, A. E. (1982). *Atmosphere-ocean dynamics* (Vol. 30). Academic Press.

National Geospatial-Intelligence Agency. (2019). *The American practical navigator (Bowditch)* [Bicentennial edition; originally published 1802 by Nathaniel Bowditch].

Stern, M. E. (1975). *Ocean circulation physics*. Academic Press.
Talley, L. D., Pickard, G. L., Emery, W. J., & Swift, J. H. (2011). *Descriptive physical oceanography: An introduction* (6th ed.). Academic Press.

Chapter 5

Structural Mechanics of Ships

5.1 Introduction

The structural integrity of a marine vessel governs its safety, performance, and longevity. Every structural component—hull plating, frames, bulkheads, decks, and masts—must withstand the forces imposed by the sea, cargo, propulsion system, and environmental loads (Hughes & Paik, 2010).
A fundamental example of structural analysis in a maritime context is the bending of a mast under wind loading. Bejan et al. (2020) analysed this problem as a beam in pure bending, demonstrating how the aerodynamic force on the sail translates into structural requirements for the mast diameter and material strength.

5.2 Scientific Background

5.2.1 Fundamentals of Stress and Strain

The elastic behaviour of structural materials is governed by *Hooke's law*, which states that the restoring force exerted by a deformed material is proportional to its displacement from the equilibrium (unstressed) configuration. Campbell (2025) writes Hooke's law as (for a conceptual introduction, see also (Hewitt et al., 2012)):

Equation 13.7 — Hooke's law:

$$F_{\text{sp}} = -k\,(\Delta x) \tag{5.1}$$

where k is the spring constant (stiffness) of the material in N m^{-1} and Δx is the displacement from the natural (unloaded) length (Campbell, 2025). The negative sign indicates a restoring force: the material resists both extension and compression.

For a solid structural element of cross-sectional area A and length L, Campbell (2025) relates the spring constant to the intrinsic material property *Young's modulus* Y:

Equation 13.8 — Young's modulus:

$$Y = \frac{k\,L}{A} \tag{5.2}$$

so that $k = YA/L$ (Campbell, 2025). Substituting into Equation (5.1) and dividing both sides by A yields the engineering stress–strain relationship:

$$\sigma = Y\,\varepsilon$$

where $\sigma = F/A$ is the normal stress and $\varepsilon = \Delta x/L$ is the engineering strain. This linear relationship holds within the elastic region; beyond the yield point the material deforms plastically, and Hooke's law no longer applies (Campbell, 2025).

For shipbuilding steel ($Y \approx 200$ GPa), even moderate stresses produce very small strains: a stress of 200 MPa (typical yield strength) corresponds to a strain of only 0.1%. This justifies the small-displacement assumption used in linear structural analysis.

Russell et al. (2015) extend this framework to the three fundamental types of stress encountered in marine structures. *Direct stress* (tensile or compressive) acts normal to the cross-section, as described above. *Shear stress* $\tau = F/A$ acts tangentially when the applied force is parallel to the cross-section; in ship structures, shear forces arise from the distribution of weight and buoyancy along the hull (Section 5.3.2). *Torsional shear stress* arises when a torque is applied to a shaft or structural member, producing a shear stress that varies linearly from zero at the centre to a maximum at the outer surface. For a solid circular shaft of radius r subjected to a torque T, the relationship between torque, shear stress τ, and angle of twist θ is given by (Russell et al., 2015):

$$\frac{T}{J} = \frac{\tau}{r} = \frac{G\theta}{l}$$

where $J = \pi d^4/32$ is the polar second moment of area, G is the shear modulus (modulus of rigidity), and l is the shaft length (Russell et al., 2015). This torsion equation is directly applicable to the design of propeller shafts, where the shaft must transmit the full engine torque from the gearbox to the propeller without exceeding the permissible shear stress of the material.

5.2.2 Material Properties of Shipbuilding Materials

Bejan et al. (2020) introduced the concept of allowable stress σ as the governing material property for structural design. In their mast bending analysis, σ represents the maximum permissible tensile and compressive stress in the mast material. A key evolutionary insight is that stronger materials (higher σ) permit more slender structural elements, which reduce weight and improve performance.

The principal shipbuilding materials are mild steel, high-tensile steel, aluminium alloys, and fibre-reinforced composites. Rawson and Tupper (2001) provide the following mechanical properties relevant to structural design:

- **Mild steel** (Lloyd's Grade A): yield stress $\sigma_y = 235\,\text{MPa}$, Young's modulus $E = 200\,\text{GPa}$, density $\rho = 7850\,\text{kg m}^{-3}$. The standard material for merchant vessel construction; the permissible bending stress under IACS rules is $175\,\text{MPa}$ (Rawson & Tupper, 2001).

- **High-tensile steel** (e.g. AH32, AH36): yield stress $\sigma_y = 315\,\text{MPa}$–$355\,\text{MPa}$. Used in highly stressed regions (deck, bottom shell amidships) to reduce plate thickness and structural weight, with a corresponding reduction in deadweight capacity penalty (Rawson & Tupper, 2001).

- **Aluminium alloy** (marine grade 5083): yield stress $\sigma_y \approx 125\,\text{MPa}$, $E \approx 70\,\text{GPa}$, $\rho \approx 2700\,\text{kg m}^{-3}$. The density is one-third that of steel, but the lower modulus means that aluminium structures must be proportionally stiffer (deeper sections) to achieve the same bending rigidity. Used primarily for superstructures and high-speed craft (Molland, 2008; Rawson & Tupper, 2001).

The choice of material is governed by the specific strength ratio σ_y/ρ: high-tensile steel offers the best strength-to-weight ratio among ferrous materials, while aluminium and composites become advantageous when total structural weight is the dominant design driver (Rawson & Tupper, 2001).

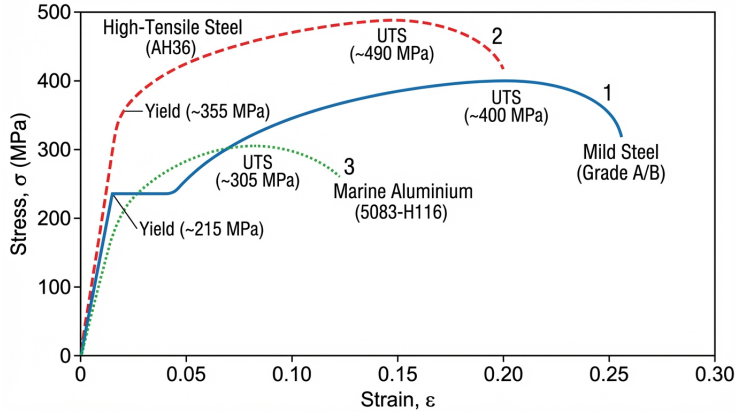

Figure 5.1: Engineering stress–strain curves for the three principal shipbuilding materials. Mild steel (Grade A, $\sigma_y = 235$ MPa) and high-tensile steel (AH36, $\sigma_y = 355$ MPa) share the same Young's modulus ($E = 200$ GPa) but differ in yield strength. Marine-grade aluminium 5083 ($\sigma_y \approx 125$ MPa, $E \approx 70$ GPa) has one-third the density of steel, making it advantageous for superstructures and high-speed craft despite its lower modulus (Rawson & Tupper, 2001).

5.2.3 Beam Theory and Bending

Bejan et al. (2020) modelled the mast of a sailing vessel as a slender elastic beam (slenderness $H/d > 50$, where H is height and d is diameter) subjected to a transverse force at its tip. This is a classical beam bending problem.

The mast receives the horizontal aerodynamic force F_a from the sail at its top. The maximum bending moment occurs at the base of the mast and has an order of magnitude:

Equation 13.1 — Maximum bending moment at mast base:

$$M_{\text{max}} \sim F_a \cdot H \tag{5.3}$$

This moment is balanced by the internal stress distribution in the mast cross-section. The bending creates tension on the forward (convex) side and compression on the aft (concave) side. The bending couple in the circular cross-section has an order of magnitude:

Equation 13.2 — Resisting moment from material stress:

$$M_{\text{resist}} \sim \sigma \cdot d^2 \cdot d = \sigma\, d^3 \tag{5.4}$$

where $\sigma\, d^2$ represents the forces of the couple (tensile and compressive, both aligned with the mast axis) and d is the arm of the couple (transverse to the mast). The rotational equilibrium condition requires:

Equation 13.3 — Structural equilibrium:

$$F_a \cdot H \sim \sigma\, d^3 \tag{5.5}$$

Substituting the aerodynamic drag force derived in the *Marine Propulsion Physics* chapter of the companion volume yields the relationship between mast diameter, height, material strength, and loading:

Equation 13.4 — Mast diameter from structural equilibrium:

$$\frac{d^3}{H} \sim \frac{\rho_a\, V_a^2\, L}{\sigma} \tag{5.6}$$

which, combined with the optimal sail proportion $H \sim L$, gives the mast slenderness ratio (Bejan et al., 2020):

Equation 13.5 — Mast slenderness ratio:

$$\frac{d}{H} \sim \left(\frac{\rho_a\, V_a^2}{\sigma}\right)^{1/3} \left(\frac{V_a}{V_w}\right)^{2/3} \tag{5.7}$$

This single formula, Equation 5.7, governs the evolutionary design of the mast structure. It encapsulates three physical effects (Bejan et al., 2020):

1. **Material strength effect:** A stronger material (larger σ) permits a more slender mast (smaller d/H).

2. **Wind loading effect:** Higher wind speeds (larger V_a) require a thicker mast (larger d/H).

3. **Performance coupling:** A thinner mast reduces dead weight, decreases the submerged hull volume, reduces hull friction, and increases boat speed.

5.3 Theoretical Framework

5.3.1 Hull Girder Bending

The hull of a ship functions as a girder subjected to vertical bending moments arising from the distribution of weight and buoyancy along its length (Hughes & Paik, 2010; Lewis, 1988). When the wave crest is amidships (hogging), the deck is in tension and the bottom in compression; when the wave trough is amidships (sagging), the loading reverses. The ultimate strength of this girder determines the vessel's ability to survive extreme wave loads.

Guedes Soares and Santos (2015) present experimental and analytical results on hull girder bending. In a series of four-point bending tests on box girder specimens, a model designated M3-150 (cross-section 800×600 mm, frame spacing 400 mm, plate thickness 1.5 mm) was tested to collapse. The ultimate bending moment was measured at 170 kN m, corresponding to a collapse load of 328 kN (Guedes Soares & Santos, 2015).

The structural tangent modulus in the post-yield region was approximately 240 MN m^2, indicating significant stiffness degradation as the plating entered the post-buckling regime. The effective column length of the stiffened panels between frames was found to be 460 mm, approximately 15% greater than the frame spacing, reflecting the partial rotational restraint provided by the transverse frames (Guedes Soares & Santos, 2015).

For the assessment of damaged hull girders, Guedes Soares and Santos (2015) describe the application of the Smith method, in which the cross-section is discretized into plate–stiffener elements, each assigned a load–shortening curve. The ultimate moment is determined incrementally by applying curvature in steps and summing the contributions of all elements. This progressive collapse methodology was applied to AFRAMAX tanker damage scenarios, providing residual strength estimates for use in structural safety assessment (Guedes Soares & Santos, 2015).

5.3.2 Shear Force and Bending Moment Distribution

Attwood (1917) established the classical procedure for determining the longitudinal bending loads on a ship hull. The hull is treated as a non-uniform beam, and the *curve of loads* along its length is obtained as the difference between the buoyancy distribution and the weight distribution at each station. Where the buoyancy exceeds the weight, the ordinate is positive (upward); where the

weight exceeds the buoyancy, the ordinate is negative. The sections at which these two curves intersect are termed *water-borne* sections (Attwood, 1917).

The *shearing force* at any section is the running integral of the curve of loads from one end of the vessel:

$$\mathrm{SF}(x) = \int_0^x q(\xi)\,\mathrm{d}\xi$$

where $q(x)$ is the net load intensity (buoyancy minus weight per unit length) at station x. The *bending moment* at any section is, in turn, the running integral of the shearing force curve (Attwood, 1917):

$$\mathrm{BM}(x) = \int_0^x \mathrm{SF}(\xi)\,\mathrm{d}\xi$$

Both the shearing force and the bending moment must return to zero at the ends of the vessel, providing an effective check on the accuracy of the calculation. The maximum bending moment typically occurs near the midship section (Attwood, 1917).

Two extreme loading conditions are considered for design purposes (Attwood, 1917):

1. **Hogging:** The wave crest is amidships. There is an excess of buoyancy amidships and an excess of weight at the ends. The deck is in tension and the bottom in compression.

2. **Sagging:** The wave trough is amidships. There is an excess of weight amidships and an excess of buoyancy at the ends. The deck is in compression and the bottom in tension.

The wave used for these calculations is assumed to have a trochoidal profile with length equal to the ship length and height taken as a fraction of the length (commonly $L/20$) (Attwood, 1917).

Bending Stress in the Hull Girder

The stress at any point in the ship's cross-section is determined from the beam bending formula (Attwood, 1917):

Equation 13.9 — Beam bending formula:

$$\frac{f}{y} = \frac{M}{I} \tag{5.8}$$

where f is the stress at a distance y from the neutral axis, M is the bending moment at the section, and I is the second moment of area (moment of inertia) of the cross-section about its neutral axis (Attwood, 1917); for a concise treatment, see (Fischer-Cripps, 2014). This formula connects the external loading (M, from the shearing force and bending moment curves) to the internal stress (f), and is the fundamental design equation for the hull girder.

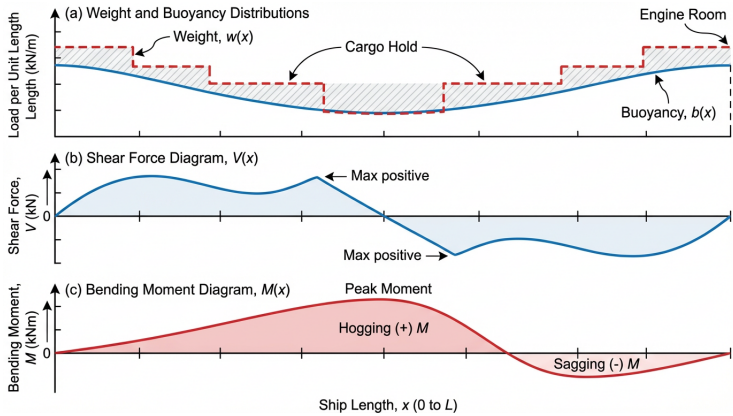

Figure 5.2: Hull girder load, shear force, and bending moment distributions for the hogging and sagging conditions. The net load curve (top panel) is the difference between the buoyancy and weight distributions along the ship's length. Integration yields the shear force (middle) and bending moment (bottom) curves; the maximum bending moment occurs near amidships in both cases. In hogging (wave crest amidships) the deck is in tension; in sagging (wave trough amidships) the deck is in compression (Attwood, 1917).

The neutral axis passes through the centroid of the cross-section, and material disposed far from the neutral axis contributes most to the section's bending resistance. Attwood (1917) illustrated this with four beams of identical cross-sectional area ($103\ \text{cm}^2$ ($16\ \text{in}^2$)) but different depth-to-width ratios: the bending resistances compared as $1 : 2 : 4 : 6\frac{2}{3}$, demonstrating that deep sections with flanges (analogous to ship decks and bottom plating) are far more effective than shallow, wide sections (Attwood, 1917).

Foster King's Approximation

Attwood (1917) reported an empirical formula, attributed to Foster King (I.N.A., 1915), for estimating the maximum bending moment without constructing the full curves of loads, shearing force, and bending moment:

Equation 13.10 — Foster King's maximum bending moment:

$$M_{\max} \approx \frac{L^2\, B\, D_w}{35} \tag{5.9}$$

where L is the ship length, B is the breadth, and D_w is the winter draught, all in consistent units (feet and foot-tons in the original) (Attwood, 1917). Twenty years of application showed agreement within approximately 5% with detailed calculations for vessels of widely dissimilar character and dimensions, confirming its utility as a preliminary design guide (Attwood, 1917).

5.3.3 Transverse Strength and Racking

In addition to longitudinal bending, a ship is subjected to strains that tend to change its transverse cross-sectional form. Attwood (1917) described this phenomenon by analogy with a square framework: when moved rapidly back and forth (as a ship does when rolling), the framework distorts into a parallelogram shape. This tendency toward transverse distortion is termed *racking* (Attwood, 1917).

The connections of beams to the ship's sides, and the transverse structural elements (frames, brackets, and deep floors), must be sufficiently strong to resist racking. Transverse watertight bulkheads are particularly valuable in this regard, as they provide rigid diaphragms that maintain the ship's cross-sectional shape. A ship when docked, especially with heavy weights such as coal or armour on board, is also subjected to severe racking strains because the support conditions differ fundamentally from the hydrostatic support provided by the surrounding water (Attwood, 1917).

The international Association of Classification Societies (IACS) provides rule-based formulae for wave-induced loads. Rawson and Tupper (2001) present the IACS standard wave bending moments:

Equation 13.16 — IACS wave-induced hogging bending moment:

$$M_{WH} = +0.19\,C\,L^{2}\,B\,C_b \quad \text{[kN m]} \tag{5.10}$$

Equation 13.17 — IACS wave-induced sagging bending moment:

$$M_{WS} = -0.11\,C\,L^{2}\,B\,(C_b + 0.7) \quad \text{[kN m]} \tag{5.11}$$

where L is the rule length in metres, B is the moulded breadth, C_b is the block coefficient, and C is a wave coefficient given by (Rawson & Tupper, 2001):

$$C = 10.75 - \left(\frac{300 - L}{100}\right)^{1.5} \qquad \text{for } 90 < L < 300\,\text{m}$$

The sagging moment is larger than the hogging moment for the same ship because the $(C_b + 0.7)$ factor exceeds C_b alone, reflecting the greater severity of the trough-amidships condition.

The corresponding IACS wave-induced shearing forces are (Rawson & Tupper, 2001):

Equation 13.18 — IACS wave-induced shearing forces:

$$S_{WH} = +0.3\,F_1\,C\,L\,B\,(C_b + 0.7), \qquad S_{WS} = -0.3\,F_2\,C\,L\,B\,(C_b + 0.7) \tag{5.12}$$

where F_1 and F_2 are distribution factors that account for the variation of shearing force along the ship's length (Rawson & Tupper, 2001). The permissible bending stress is 175 MPa and the permissible shear stress is 110 MPa for mild steel (Rawson & Tupper, 2001).

The quantitative analysis of transverse strength begins with the loading on individual frames. Each transverse frame carries the lateral pressure exerted by the sea on the shell plating over a strip of hull equal to the frame spacing s. At a depth z below the waterline, the hydrostatic component of this pressure is $p = \rho g z$, and the total lateral load on the frame at that depth is $q(z) = p \cdot s = \rho g z\, s$ per unit length of frame (Rawson & Tupper, 2001). In heavy weather the total pressure includes a hydrodynamic component from wave impacts, which classification societies account for through minimum design pressure heads that exceed the static waterline depth (Hughes & Paik, 2010).

Each side frame is a structural beam spanning from the double bottom to the deck, supported at its ends by the bottom structure and the deck beam. The bending moment in the frame depends on the end-fixity conditions: if assumed simply supported, the maximum bending moment at mid-span under a triangular (hydrostatic) load is $M = q_{\max}\, l^2/15$, where $q_{\max}$ is the load intensity at the lower support and l is the span; if assumed fully fixed at both ends, the support moments are larger but the mid-span moment is reduced. In practice, the boundary conditions are intermediate, and classification society rules provide effective span corrections (Rawson & Tupper, 2001). The required section modulus of the frame is then obtained from the beam bending formula (Equation 5.8) as $Z = M/\sigma_{\text{perm}}$, where σ_{perm} is the permissible bending stress for the material (Rawson & Tupper, 2001).

Deep web frames, spaced at intervals of three to five ordinary frame spacings, provide additional transverse rigidity by acting as deep beams with high bending stiffness. Together with transverse watertight bulkheads, which function as rigid diaphragms, they form a transverse support system that resists the racking deformation described by Attwood (1917). United States Naval Academy (2021) distinguish the two principal framing arrangements: *transverse framing*, in which closely spaced frames run athwartship and provide natural racking resistance, and *longitudinal framing*, in which the primary stiffeners run fore-and-aft (improving longitudinal buckling resistance at the cost of reduced inherent transverse stiffness). In longitudinally framed vessels, the transverse web frames and cross-ties must be proportionally heavier to compensate for the absence of closely spaced transverse members (Hughes & Paik, 2010; United States Naval Academy, 2021).

5.3.4 Local Structural Loading

Vertical Loads from Shipping Water Events

Local structural loading on ship decks includes the vertical forces generated by water shipping (green water) events. Hernández-Fontes et al. (2020) measured the quasi-static vertical loads over the deck of a rectangular fixed structure subjected to different types of shipping water events, generated using the wet dam-break method. A force balance of four S-type axial load cells,

with a sampling rate of 500 Hz and a 100 Hz low-pass filter, was synchronised with wave probes and a high-speed camera to capture the relationship between flow patterns and structural loading.

The non-dimensional vertical force on the deck was defined as:

Equation 13.6 — Non-dimensional vertical force from shipping water:

$$F^* = \frac{F}{\rho\, g\, h_1\, L^2} \tag{5.13}$$

where F is the measured vertical force, $\rho = 1000\,\mathrm{kg\,m^{-3}}$ is the water density, $g = 9.81\,\mathrm{m\,s^{-2}}$ is gravitational acceleration, h_1 is the upstream water depth (reference depth), and $L = 0.195\,\mathrm{m}$ is the deck length of the structure (Hernández-Fontes et al., 2020).

Forward and Backflow Loading Trends

Two distinct loading phases were defined (Hernández-Fontes et al., 2020):

- **Forward loading:** Generated by water propagating from the bow over the deck until the shipped water reached its maximum displacement on the vertical wall during run-up. The forward peak load is denoted M_1.
- **Backflow loading:** Generated after the maximum wall run-up, including loads from water returning toward the reservoir. The backflow peak load is denoted M_2.

The mean maximum forward loads varied strongly with the type of shipping water event:

Table 5.1: Forward peak loads by event type (Hernández-Fontes et al., 2020).

Event type	Bore steepness ε	Mean max. F^* (M_1)
DB	0.12	≈ 0.082
PDBSC ($r_d \approx 0.6$)	0.21	≈ 0.24
PDBSC ($r_d \approx 0.5$)	0.33	≈ 0.424
PDBLC ($r_d \approx 0.4$)	0.55	≈ 0.529

The forward peak load for the most severe event (PDBLC) was approximately 6.4 times larger than for the mildest event (DB). The PDBSC events showed intermediate loading, with the peak load increasing by approximately 176% and 517% relative to the moderate and mild events, respectively, for the $\varepsilon \approx 0.33$ case (Hernández-Fontes et al., 2020).

Significance of Backflow Loads

A key structural design finding from Hernández-Fontes et al. (2020) is that backflow loads are of the same order as forward loads. The ratio of backflow

peak to forward peak, M_2/M_1, ranged between 0.64 and 0.86 for all cases tested. For longer (less steep) bores, the forward and backflow peak loads were very similar. The difference between M_1 and M_2 remained almost constant for bore steepnesses between 0.2 and 0.35, with M_2 less than approximately 38% of M_1 in each case. However, this difference increased for the steepest bore ($\varepsilon \approx 0.55$), where the forward peak load exceeded the backflow peak load by approximately 40% (Hernández-Fontes et al., 2020).

This finding has direct implications for the structural design of marine decks and superstructures. For configurations where shipping water interacts with vertical walls or structures located on the deck, backflow loads should be considered alongside forward loads in the design process (Hernández-Fontes et al., 2020).

Influence of Freeboard and Installation Dimensions

The experiments with two different freeboards ($f_b = 0.030\,\text{m}$ and $0.042\,\text{m}$) confirmed that the highest peak loads occurred for the lowest freeboard. Furthermore, Hernández-Fontes et al. (2020) compared their results with those from a larger installation and found that the vertical loads over the deck were lower in the larger facility, attributed to the longer distance for bore development and wall friction effects. This indicates that shipping water patterns and loading are sensitive to the dimensions of the experimental installation, and any systematic evaluation should use a consistent setup (Hernández-Fontes et al., 2020).

5.3.5 Buckling and Instability

Buckling is the dominant failure mode for the compressed plating and stiffened panels that constitute the hull envelope. The box girder experiments of Guedes Soares and Santos (2015) (Section 5.3.1) demonstrated that the collapse of the compressed flange (deck or bottom plating, depending on the loading sense) governs the ultimate bending capacity of the hull girder.

The effective column length measured in the box girder tests—$460\,\text{mm}$ against a $400\,\text{mm}$ frame spacing—indicates that the boundary conditions at the frames are intermediate between simply supported and clamped. This finding has practical implications for design: assuming simply supported boundaries underestimates the buckling strength, while assuming clamped boundaries overestimates it. The experiments provide calibration data for finite element and analytical buckling models (Guedes Soares & Santos, 2015).

A slender column of length l subjected to an axial compressive load will buckle when the load reaches the Euler critical load. Rawson and Tupper (2001) present the Euler formula for the critical buckling stress:

Equation 13.19 — Euler column buckling stress:

$$\sigma_E = \frac{\pi^2 E}{\left(l/k\right)^2} \tag{5.14}$$

where E is Young's modulus and l/k is the slenderness ratio (column length divided by the radius of gyration of the cross-section) (Rawson & Tupper, 2001). The Euler formula applies strictly to perfect, elastic columns; real ship structural members have initial imperfections and residual welding stresses that reduce the critical load.

For flat rectangular plates under uniaxial compression, Rawson and Tupper (2001) give the Bryan critical buckling stress:

Equation 13.20 — Bryan plate buckling stress:

$$\sigma_{cr} = K_c \frac{\pi^2 E}{12\left(1-\nu^2\right)} \left(\frac{t}{b}\right)^2 \tag{5.15}$$

where K_c is a buckling coefficient that depends on the plate aspect ratio and boundary conditions (a minimum of $K_c = 4.0$ for a simply supported plate with aspect ratio ≥ 1), ν is Poisson's ratio (≈ 0.3 for steel), t is the plate thickness, and b is the shorter plate dimension (typically the frame spacing) (Rawson & Tupper, 2001). Equation (5.15) shows that the buckling stress is proportional to the square of the thickness-to-width ratio, explaining why thin, wide panels are most susceptible to buckling failure.

For intermediate slenderness ratios where inelastic buckling occurs, the Johnson–Ostenfeld correction modifies the Euler stress to account for material yielding (Hughes & Paik, 2010; Rawson & Tupper, 2001):

$$\sigma_{JO} = \sigma_y \left(1 - \frac{\sigma_y}{4\,\sigma_E}\right) \quad \text{for } \sigma_E > \sigma_y/2$$

This correction ensures a smooth transition from the elastic buckling regime (Euler) to the yield-limited regime, where the column squashes rather than buckles (Rawson & Tupper, 2001).

5.3.6 Fatigue Damage Mechanics

The fatigue life of structural steel is characterised by the S–N curve, which relates the applied stress range $\Delta\sigma$ to the number of cycles to failure N. For a given material and weld detail category, the S–N relationship takes the power-law form (Li et al., 2013):

Equation 13.11 — S–N fatigue life relation:

$$\log N = \log \bar{a} - m \log \Delta\sigma \tag{5.16}$$

where $\bar{a}$ is the intercept parameter (dependent on the detail category and probability of survival) and m is the inverse slope of the S–N curve. For welded ship structural details, classification society rules typically specify $m = 3$ for the high-cycle regime (Li et al., 2013).

When a structural detail is subjected to a variable-amplitude loading history, the cumulative fatigue damage is assessed using the Palmgren–Miner linear accumulation rule (Li et al., 2013):

Equation 13.12 — Palmgren–Miner cumulative damage rule:

$$D = \sum_{i=1}^{k} \frac{n_i}{N_i} \tag{5.17}$$

where n_i is the number of stress cycles at stress range $\Delta\sigma_i$ and N_i is the number of cycles to failure at that stress range from the S–N curve. Failure is predicted when $D \geq 1$. Despite its simplicity and the neglect of load-sequence effects, this rule remains the standard for ship structural fatigue assessment (Li et al., 2013).

For a narrow-band Gaussian stress process, the short-term stress range follows a Rayleigh distribution. Li et al. (2013) express the short-term fatigue damage in sea state j as:

Equation 13.13 — Narrow-band short-term fatigue damage:

$$D_j = \frac{\nu_j \, T_j}{\bar{a}} \, (2\sqrt{2}\,\sqrt{m_{0,j}})^m \, \Gamma\!\left(1 + \frac{m}{2}\right) \tag{5.18}$$

where ν_j is the zero-crossing frequency, T_j is the duration of sea state j, $m_{0,j}$ is the zeroth spectral moment (variance) of the stress response in that sea state, and $\Gamma(\cdot)$ is the gamma function (Li et al., 2013). This closed-form expression is the basis of the spectral fatigue method, in which the stress response spectrum is computed from the wave spectrum and the ship's structural transfer functions.

The long-term fatigue damage over the vessel's operational lifetime is accumulated by summing the contributions from all encountered sea states, weighted by their probability of occurrence (Li et al., 2013):

Equation 13.14 — Long-term fatigue damage accumulation:

$$D_{\text{total}} = \sum_{i=1}^{n} p_i \, D_i \tag{5.19}$$

where p_i is the fraction of the vessel's lifetime spent in sea state i and D_i is the fatigue damage accumulated in that sea state (Li et al., 2013). The design criterion requires $D_{\text{total}} < 1$ for the target service life, typically 20–25 years for merchant vessels.

The nominal stress obtained from beam theory or global finite element analysis does not account for stress concentrations at structural discontinuities. The stress concentration factor (SCF) relates the local hotspot stress to the nominal stress (Li et al., 2013):

Equation 13.15 — Stress concentration factor:

$$K = \frac{\sigma_{\text{hs}}}{\sigma_{\text{nom}}} \tag{5.20}$$

where σ_{hs} is the hotspot stress at the weld toe (or other critical location) and σ_{nom} is the nominal stress from global analysis (Li et al., 2013). The hotspot

stress is typically determined by surface stress extrapolation from fine-mesh finite element models, following the procedures specified by classification societies.

Li et al. (2013) applied both spectral and time-domain fatigue methods to the side-shell structure of a Panamax container vessel ($L_{pp} = 281\,\text{m}$, $B = 32.26\,\text{m}$, $C_b = 0.68$) operating on a North Atlantic trade route. The time-domain method employed nonlinear hydrodynamic analysis to capture intermittent wetting in the splash zone near the waterline, where the alternating submergence and emergence of the hull introduces asymmetric pressure loading that cannot be captured by linear (spectral) methods. Full-scale strain measurements from an onboard monitoring system over two years of operation provided validation data for both methods (Li et al., 2013).

The computed fatigue life at a critical side-shell longitudinal connection was 6.7 years by the time-domain method and 7.1 years by the spectral method—both well below the 20-year design target, confirming the fatigue vulnerability of the splash-zone region. The moderate-to-severe sea states ($H_s = 3.5$–$9.5\,\text{m}$) contributed approximately 80% of the total fatigue damage despite accounting for less than 20% of the operational time, demonstrating the disproportionate influence of heavy weather on fatigue accumulation (Li et al., 2013).

5.3.7 Ship Vibration and Resonance

The hull girder vibrates as a free–free beam, with natural frequencies determined by its bending stiffness EI, mass distribution, and length. Rawson and Tupper (2001) present the two-node vertical vibration frequency (the lowest natural mode) using the empirical Schlick formula:

Equation 13.21 — Schlick formula for two-node vibration:

$$N_2 = c_1 \sqrt{\frac{I}{L^3\,\Delta}} \tag{5.21}$$

where N_2 is the two-node frequency in cycles per minute, I is the amidships second moment of area in m^4, L is the ship length in metres, Δ is the displacement in tonnes, and c_1 is an empirical constant ($c_1 \approx 200{,}000$–$280{,}000$ depending on ship type) (Rawson & Tupper, 2001). This frequency typically falls in the range 0.5–1.5 Hz for merchant ships, which can coincide with the blade-rate frequency $f_z = z \cdot n$ (derived in the *Marine Propulsion Physics* chapter of the companion volume) of the main propeller, creating a potential resonance condition.

The structural designer must ensure that the two-node frequency does not coincide with the propeller blade-rate frequency or its principal harmonics. If resonance cannot be avoided by adjusting the propeller speed or blade number, the vibration amplitude must be controlled through stiffening of the aft body structure, increasing the hull girder moment of inertia, or installing vibration neutralisers (Rawson & Tupper, 2001).

5.3.8 Structural Reliability and Limit States

The deterministic approach to structural design—in which the applied loads must not exceed the permissible stresses (Section 5.4.1)—does not explicitly account for the uncertainties inherent in loading predictions, material properties, geometric tolerances, and modelling assumptions. *Structural reliability* methods formalise these uncertainties within a probabilistic framework, expressing the safety of the hull girder in terms of the probability of failure P_f and the associated reliability index β (Decò et al., 2012).

Corrosion and Time-Variant Hull Thickness

The net hull girder capacity diminishes over the vessel's lifetime due to corrosion wastage. Decò et al. (2012) model the time-variant thickness of a structural plate as:

Equation 13.22 — Time-variant plate thickness with corrosion:

$$d(t) = d_0 - r(t) \tag{5.22}$$

where d_0 is the original as-built plate thickness and $r(t)$ is the corrosion depth at time t. Corrosion is assumed to commence after the protective coating breaks down at time T_c (typically 5–10 years for marine coatings), and the subsequent wastage follows a power-law model (Decò et al., 2012):

$$r(t) = C_1 \, (t - T_c)^{C_2} \quad \text{for } t > T_c$$

where C_1 and C_2 are empirical parameters that depend on the location and type of structural member. As the plate thickness decreases, the section modulus of the hull girder decreases, and the ultimate bending capacity declines accordingly. This time-variant degradation means that the structural reliability is not constant but decreases monotonically after the onset of corrosion (Decò et al., 2012).

Limit State Equations for Hull Girder Failure

The structural safety of the hull girder is assessed by defining a *limit state function* g that represents the margin between the structural capacity (resistance) and the applied load (demand). Failure occurs when $g \leq 0$. Decò et al. (2012) define limit state functions for both the ultimate collapse and the first failure of the hull girder.

The limit state for ultimate sagging failure at time t is (Decò et al., 2012):

Equation 13.23 — Limit state for ultimate sagging:

$$g_{\text{US}}(t) = \chi_u \, M_u(t) - \left[\chi_{\text{sw}} \, M_{\text{sw}} + \chi_w \, M_w\right] \tag{5.23}$$

where $M_u(t)$ is the time-variant ultimate sagging bending moment capacity of the hull cross-section, M_{sw} is the still water bending moment, M_w is the

wave-induced vertical bending moment, and χ_u, χ_{sw}, and χ_w are model uncertainty factors for the ultimate strength, still water load, and wave-induced load, respectively. The corresponding limit state for ultimate hogging is (Decò et al., 2012):

Equation 13.24 — Limit state for ultimate hogging:

$$g_{\text{UH}}(t) = \chi_u \, M_u(t) - \left[\chi_{\text{sw}} \, M_{\text{sw}} + \chi_w \, M_w\right] \tag{5.24}$$

where $M_u(t)$ now refers to the ultimate hogging capacity.

The first failure limit states replace the ultimate capacity M_u with the initial yielding moment M_y, which represents the bending moment at which the extreme fibre of the cross-section reaches yield stress (Decò et al., 2012):

$$g_{\text{FS}}(t) = \chi_y \, M_y(t) - \left[\chi_{\text{sw}} \, M_{\text{sw}} + \chi_w \, M_w\right]$$

The ultimate capacity M_u accounts for the post-yield reserve strength due to progressive collapse of stiffened panels: as individual plate-stiffener combinations buckle or yield, load is redistributed to the remaining intact elements until the cross-section can no longer sustain additional moment (Decò et al., 2012). This incremental procedure, developed by Smith (1977) and adopted by IACS as the standard method for ultimate hull girder strength assessment, typically yields $M_u > M_y$ by a factor of 1.1–1.3 depending on the structural arrangement (Decò et al., 2012).

Reliability Index

Given the limit state function g, the probability of failure is (Decò et al., 2012):

$$P_f = P(g \leq 0)$$

The structural reliability is conventionally expressed through the *reliability index*:

Equation 13.25 — Reliability index:

$$\beta = \Phi^{-1}(1 - P_f) \tag{5.25}$$

where Φ^{-1} is the inverse of the standard normal cumulative distribution function (Decò et al., 2012). A higher β corresponds to a lower probability of failure; typical target values for naval vessel hull girders are $\beta = 3.0$–4.0, corresponding to $P_f \approx 10^{-3}$–10^{-5} (Decò et al., 2012).

Decò et al. (2012) computed the reliability index using the First-Order Reliability Method (FORM), which linearises the limit state surface in the space of standard normal variables and computes β as the minimum distance from the origin to the failure surface. For a joint high-speed sealift vessel ($L = 290$ m, $B = 32$ m), the initial reliability index was $\beta \approx 5.3$ for ultimate sagging, declining to $\beta \approx 3.1$ after 25 years of corrosion-induced degradation—a reduction of over 40% (Decò et al., 2012).

Redundancy Assessment

A structural system is *redundant* if it can sustain loads after the failure of one or more of its components. Decò et al. (2012) quantify structural redundancy through two indices. The first redundancy index measures the reserve capacity of the intact system relative to first component failure:

Equation 13.26 — Redundancy index (intact reserve):

$$RI_1 = \frac{\beta_{\text{intact}} - \beta_{\text{first}}}{\beta_{\text{intact}}} \tag{5.26}$$

where β_{intact} is the reliability index for ultimate system failure and β_{first} is the reliability index for first component failure (Decò et al., 2012). A value of $RI_1 = 0$ indicates a non-redundant (series) system in which the failure of any single element causes system collapse; positive values indicate reserve capacity beyond first failure.

The second redundancy index measures the residual capacity of the damaged system:

Equation 13.27 — Redundancy index (residual capacity):

$$RI_2 = \frac{\beta_{\text{damaged}} - \beta_{\text{first}}}{\beta_{\text{damaged}}} \tag{5.27}$$

where β_{damaged} is the reliability index for the system with one component failed (Decò et al., 2012). Both indices vary with time as corrosion reduces the structural capacity, and their polar representations across all headings and sea states provide a comprehensive map of the vessel's operational safety envelope (Decò et al., 2012).

5.4 Applications in Maritime Systems

5.4.1 Classification Society Rules and Standards

Classification societies (Lloyd's Register, DNV, Bureau Veritas, ABS, etc.) establish the minimum structural scantlings for hull construction. Rawson and Tupper (2001) describe the rule-based design framework: the IACS Unified Requirements specify the still-water and wave-induced load components (Equations 5.10–5.12), define the permissible stress levels for mild steel ($\sigma_{\text{max}} = 175\,\text{MPa}$, $\tau_{\text{max}} = 110\,\text{MPa}$), and require that the midship section modulus $Z = I/y_{\text{max}}$ is sufficient to keep the bending stress within these limits under the combined still-water and wave-induced moments (Rawson & Tupper, 2001).

Modern classification rules have evolved from purely prescriptive requirements to goal-based standards that permit rational analysis (direct calculation of loads and structural response) as an alternative to tabulated scantlings. Rawson and Tupper (2001) note that the direct calculation

approach—combining hydrodynamic load analysis, finite element stress analysis, and fatigue assessment—is now required for all large ships ($L > 150\,\text{m}$) and is increasingly used for smaller vessels where novel structural arrangements fall outside the scope of tabulated rules.

5.4.2 Finite Element Analysis (FEA) in Ship Structures

Li et al. (2013) describe a hierarchical finite element methodology for ship structural fatigue assessment. Three modelling levels are employed in sequence: (1) a global model of the entire hull structure, which provides the overall structural response under wave loading; (2) a local model of the region of interest (e.g., a side-shell frame space), refined from the global model using sub-modelling techniques with displacement boundary conditions; and (3) a hotspot model with fine mesh at the critical structural detail (e.g., the connection between a longitudinal stiffener and a transverse web frame), from which the hotspot stress is extracted by surface stress extrapolation (Li et al., 2013).

This sub-modelling approach allows the accurate determination of local stress fields without the computational cost of applying a fine mesh to the entire hull. The global model captures the wave-induced load distribution, the local model captures the structural geometry of the frame space, and the hotspot model captures the stress concentration at the weld toe. For the Panamax container vessel analysed by Li et al. (2013), this three-level approach was applied to the side-shell longitudinal connections in the splash zone, where nonlinear hydrodynamic pressures from intermittent wetting produce the most severe fatigue loading (Li et al., 2013).

5.4.3 Structural Health Monitoring

Li et al. (2013) utilised full-scale strain measurements from an onboard hull monitoring system installed on a Panamax container vessel to validate computational fatigue predictions. Strain gauges mounted on side-shell longitudinal stiffeners recorded the stress history over approximately two years of North Atlantic operation. The measured strain data were processed using the rainflow counting method to extract the stress range histogram, which was then compared with the computed stress ranges from both spectral and time-domain analyses (Li et al., 2013).

The measured stress ranges were correlated with hindcast wave data to reconstruct the environmental conditions encountered during each voyage leg. This combination of onboard strain measurement and hindcast environmental data enabled a direct comparison between measured and predicted fatigue damage, providing a rigorous validation framework. The agreement between measured and computed fatigue damage confirmed the reliability of both the hydrodynamic loading models and the structural finite element models (Li et al., 2013).

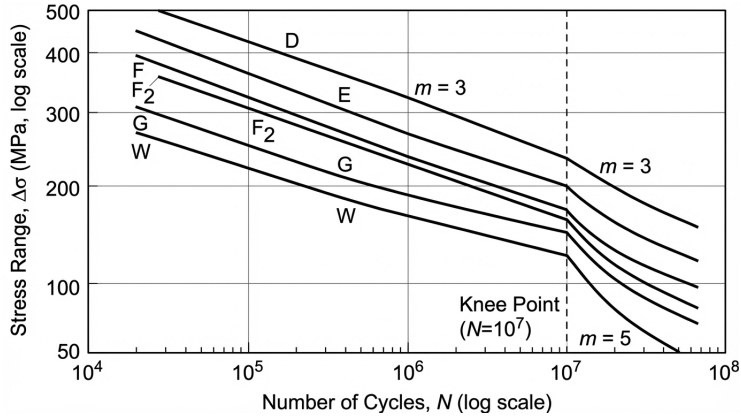

Figure 5.3: S–N fatigue curves for welded ship structural detail categories D through W, plotted with an inverse slope of $m = 3$ (Equation 5.16). Higher detail categories (e.g. D) correspond to less severe stress concentrations and longer fatigue lives. The dashed vertical line marks the approximate 25-year design life ($\sim 10^8$ cycles). For the side-shell splash zone of a Panamax container vessel, Li et al. (2013) computed fatigue lives of only 6.7–7.1 years at Category F2, well below the design target.

5.4.4 Collision and Grounding Structural Response

The structural response to collision involves both external mechanics (the global dynamics of the striking and struck vessels) and internal mechanics (the local deformation and energy absorption of the hull structure). Rawson and Tupper (2001) describe the external problem: the kinetic energy of the collision is determined by the masses, speeds, and approach angle of the two vessels, with the hydrodynamic added mass increasing the effective striking mass by 10–40% depending on the direction of motion.

The internal mechanics of collision determine how the kinetic energy is absorbed by structural deformation. Rawson and Tupper (2001) note that Minorsky's empirical correlation—relating the volume of damaged structure to the absorbed energy—provides a first estimate, but finite element analysis is required for detailed assessment of specific structural arrangements such as double-hull tankers and side-shell frames (Rawson & Tupper, 2001).

For grounding, two distinct scenarios are considered: *stranding* (the ship comes to rest on a shoal or reef) and *bottom raking* (the ship moves forward over a rock or reef, opening the bottom structure along a considerable length). Rawson and Tupper (2001) explain that in bottom raking, the structural resistance is provided by the double-bottom floors, inner bottom plating, and longitudinal girders; the energy absorption depends on the depth of penetration and the longitudinal extent of the contact. Modern double-hull requirements (MARPOL Annex I) increase the structural energy absorption capacity by providing an additional barrier between the outer shell and the

cargo spaces (Rawson & Tupper, 2001).

5.5 Discussion

The mast bending analysis of Bejan et al. (2020) demonstrates a general principle of structural design in maritime systems: structural dimensions are not arbitrary but are determined by the balance between external loading (aerodynamic, hydrodynamic, wave-induced) and material strength. The engineering consequence is direct—advances in material science (higher σ) directly translate to lighter, more efficient vessels with improved performance.

This principle extends to every structural element of a ship: hull plating thickness is determined by hydrostatic and wave pressures; frame spacing is determined by plate buckling criteria; and longitudinal strength members are sized by the hull girder bending moment. In each case, the structural design is a physics problem involving force balance and material limits.

The shipping water loading data of Hernández-Fontes et al. (2020) add a further dimension to local structural design. Their experiments demonstrate that the type of incoming wave—characterised by bore steepness—determines not only the magnitude of the vertical load on the deck but also the loading pattern over time. The finding that backflow loads are 64–86% of forward loads has direct design implications: structural assessments that consider only the forward (impact) loading phase underestimate the total loading cycle. Moreover, the sensitivity of shipping water loads to freeboard and installation dimensions highlights the need for consistent experimental setups when deriving design loads from laboratory data.

The reliability-based approach of Decò et al. (2012) represents a further evolution in structural assessment methodology. Whereas deterministic design compares a single load value against a single capacity value with prescribed safety factors, the probabilistic framework captures the full distributions of both. The resulting reliability index β provides a unified measure of structural safety that integrates all sources of uncertainty—loading randomness, material variability, modelling error, and progressive corrosion. The monotonic decline in β with time (from 5.3 to 3.1 over 25 years for the case study vessel) demonstrates that static safety factors cannot guarantee adequate safety over the vessel's entire operational life, and that time-variant reassessment is necessary. The redundancy indices RI_1 and RI_2 add a systems perspective: even when the system reliability index is acceptable, a low redundancy index signals that the cross-section is operating close to its first-failure threshold and has limited capacity to redistribute loads after local component buckling or yielding.

The torsion analysis introduced by Russell et al. (2015) addresses a distinct aspect of the structural loading picture. While the hull girder analysis treats longitudinal bending and shear, the propulsion system introduces significant torsional loads through the propeller shaft, intermediate shafts, and stern

tube. The classical relationship $T/J = \tau/r = G\theta/l$ enables direct calculation of these torsional stresses from the engine torque, ensuring that the shaft diameter is sufficient to transmit full power without exceeding the material's shear strength.

The shaft-line vibration studies compiled in Sutulo and Guedes Soares (2023) extend this torsional picture to coupled lateral–torsional dynamics. When the propeller operates in a non-uniform wake, the fluctuating torque at blade-rate frequency excites not only torsional shaft modes but also lateral whirl modes through gyroscopic coupling. If a whirl natural frequency coincides with a structural resonance of the stern bearing support or the engine-room double bottom, the vibration amplitude can exceed the levels predicted by the uncoupled Schlick formula (Equation 5.21) or the simple torsion equation alone. Finite element models that include the shaft, bearings, stern tube, and local hull structure as a coupled system are therefore necessary for vibration predictions in the aft body (Sutulo & Guedes Soares, 2023).

The engineering course notes of United States Naval Academy (2021) provide a complementary pedagogical perspective on ship structural design. The USNA treatment distinguishes transverse framing (frames running athwartship at close spacing, typical of older cargo vessels) from longitudinal framing (longitudinal stiffeners supported by widely spaced transverse web frames, standard for large tankers and bulk carriers), and explains the structural rationale: longitudinal framing increases the critical buckling stress of the deck and bottom plating by reducing the unsupported panel width in the direction of the dominant compressive stress. Laboratory exercises on section modulus calculation—measuring the moment of inertia of an idealised midship section and verifying the bending stress formula (Equation 5.8)—reinforce the theoretical link between geometry, material distribution, and structural capacity (United States Naval Academy, 2021).

5.6 Conclusion

The structural behaviour of a ship is governed by the hierarchy of load paths—from global hull girder bending to local plate and stiffener response—each analysed by the classical mechanics of beams, plates, and columns. The mast bending analysis of Bejan et al. (2020) encapsulates this hierarchy in miniature: the structural equilibrium $F_a H \sim \sigma d^3$ (Equation 5.5) directly links external aerodynamic loading to internal material stress, and the resulting slenderness ratio (Equation 5.7) shows that stronger materials permit lighter, more efficient structures. At the hull girder scale, the same beam-bending principle appears in the formula $f/y = M/I$ (Equation 5.8), where the bending moment—approximated by Foster King's $M_{\max} \approx L^2 B D_w/35$ (Equation 5.9) or computed from IACS wave-induced loads (Equations 5.10–5.12)—determines the required section modulus (Attwood, 1917; Rawson &

Tupper, 2001). Hooke's law ($\sigma = Y\varepsilon$), extended through the buckling formulae of Euler (Equation 5.14) and Bryan (Equation 5.15), governs the slenderness limits of compressed plating, while the Johnson–Ostenfeld correction bridges the elastic and inelastic buckling regimes (Campbell, 2025; Rawson & Tupper, 2001).

Local and dynamic loading phenomena complete the structural picture. Shipping water events impose quasi-static vertical deck loads that scale with bore steepness ($F^* \approx 0.08$–0.53), and the backflow phase generates loads 64–86% as large as the forward impact, demanding consideration in design (Hernández-Fontes et al., 2020). Fatigue, assessed through the S–N relation (Equation 5.16) and the Palmgren–Miner accumulation rule (Equation 5.17), is the life-limiting failure mode for welded connections in the splash zone: spectral and time-domain analyses for a Panamax container vessel both predicted fatigue lives of only 6.7–7.1 years, well below the 20-year design target, with moderate-to-severe sea states contributing 80% of the total damage despite less than 20% of the operational exposure (Li et al., 2013). The torsion equation $T/J = \tau/r = G\theta/l$ sizes the propeller shaft, and coupled lateral–torsional shaft dynamics can amplify aft-body vibration when blade-rate excitation coincides with structural resonances (Russell et al., 2015; Sutulo & Guedes Soares, 2023).

The probabilistic framework of structural reliability introduces the reliability index $\beta = \Phi^{-1}(1 - P_f)$ (Equation 5.25) and the redundancy indices RI_1 and RI_2 (Equations 5.26–5.27) as unified measures of safety and damage tolerance. Corrosion wastage, modelled by the power law $r(t) = C_1(t - T_c)^{C_2}$ (Equation 5.22), drives a monotonic decline in hull girder capacity—from $\beta \approx 5.3$ at new-build to $\beta \approx 3.1$ after 25 years for the case study vessel—demonstrating that static safety factors alone cannot guarantee adequate safety over the vessel's lifetime (Decò et al., 2012). Longitudinal framing, adopted in large tankers and bulk carriers, increases the critical buckling stress by reducing unsupported panel widths in the direction of dominant compression, a principle validated by section modulus measurement and the bending stress formula (United States Naval Academy, 2021).

References

Attwood, E. L. (1917). *A text-book of theoretical naval architecture* (7th ed.) [First published 1899; seventh edition revised 1916, reprinted 1917]. Longmans, Green; Co.

Bejan, A., Ferber, L., & Lorente, S. (2020). Convergent evolution of boats with sails. *Scientific Reports*, *10*, Article 2703. https://doi.org/10.1038/s41598-020-58940-5

Campbell, C. (2025). *Physics: A focused introduction*. CRC Press. https://doi.org/10.1201/9781003571568

Decò, A., Frangopol, D. M., & Zhu, B. (2012). Reliability and redundancy assessment of ships under different operational conditions. *Engineering Structures*, *42*, 457–471. https://doi.org/10.1016/j.engstruct.2012.04.017

Fischer-Cripps, A. C. (2014). *The physics companion* (2nd ed.). CRC Press. https://doi.org/10.1201/b17356

Guedes Soares, C., & Santos, T. A. (Eds.). (2015). *Maritime technology and engineering: Proceedings of MARTECH 2014*. CRC Press.

Hernández-Fontes, J. V., Vitola, M. A., Esperança, P. T. T., Sphaier, S. H., & Silva, R. (2020). Patterns and vertical loads in water shipping in systematic wet dam-break experiments. *Ocean Engineering*, *197*, 106891. https://doi.org/10.1016/j.oceaneng.2019.106891

Hewitt, P. G., Suchocki, J. A., & Hewitt, L. A. (2012). *Conceptual physical science* (5th ed.). Pearson.

Hughes, O. F., & Paik, J. K. (2010). *Ship structural analysis and design*. The Society of Naval Architects; Marine Engineers.

Lewis, E. V. (Ed.). (1988). *Principles of naval architecture* (2nd ed.) [Three volumes]. The Society of Naval Architects; Marine Engineers.

Li, Z., Ringsberg, J. W., & Storhaug, G. (2013). Time-domain fatigue assessment of ship side-shell structures. *International Journal of Fatigue*, *55*, 276–290. https://doi.org/10.1016/j.ijfatigue.2013.07.007

Molland, A. F. (Ed.). (2008). *The maritime engineering reference book: A guide to ship design, construction and operation*. Butterworth-Heinemann. https://doi.org/10.1016/B978-0-7506-8987-8.X0001-7

Rawson, K. J., & Tupper, E. C. (2001). *Basic ship theory* (5th ed.). Butterworth-Heinemann.

Russell, P. A., Jackson, L., & Embleton, W. (2015). *Applied mechanics for marine engineers* (6th ed., Vol. 2). Thomas Reed.

Sutulo, S., & Guedes Soares, C. (2023). Ship dynamics and hydrodynamics. *Journal of Marine Science and Engineering*, *11*(5), 911. https://doi.org/10.3390/jmse11050911

United States Naval Academy. (2021). En400: Principles of ship performance [Course notes, Fall AY2021].

Chapter 6

Acoustics and Underwater Sound

6.1 Introduction

Sound is the primary means of remote sensing, communication, and navigation in the ocean (Urick, 1983). Electromagnetic radiation is rapidly absorbed in seawater (Chapter 2), making optical and radar methods effective only over short distances. Acoustic waves, by contrast, can propagate over hundreds or even thousands of kilometres under favourable conditions, making underwater acoustics the foundation of echo sounding, sonar, submarine communication, and current measurement.

As Dera (1992) demonstrated, the acoustic properties of seawater are governed by its thermodynamic state: the speed of sound depends on temperature, salinity, and pressure, while absorption involves molecular relaxation processes specific to the dissolved salts in seawater.

6.2 Scientific Background

6.2.1 Fundamentals of Sound and Acoustic Waves

Sound in the ocean is a longitudinal pressure disturbance propagating through the seawater medium (Hewitt et al., 2012; Medwin & Clay, 1998). The linearised equation of motion for a small acoustic perturbation is (Dera, 1992, Eq. 8.0.5b):

Equation 14.1 — Acoustic equation of motion:

$$\rho_0 \frac{\partial u_i}{\partial t} = -\frac{\partial p}{\partial x_i} \tag{6.1}$$

where ρ_0 is the undisturbed density, u_i is the acoustic particle velocity component, and p is the acoustic pressure perturbation. The acoustic pressure and density perturbation are related by the elastic law (Dera, 1992, Eq. 8.0.7):

Equation 14.2 — Acoustic law of elasticity:

$$p = c^2 \, \delta\rho \tag{6.2}$$

where c is the speed of sound and $\delta\rho$ is the small density perturbation from the equilibrium value.

Combining the equation of motion with the continuity equation and the elastic law yields the fundamental acoustic wave equation for a non-attenuating medium (Dera, 1992, Eq. 8.0.15):

Equation 14.3 — Acoustic wave equation:

$$\frac{\partial^2 p}{\partial t^2} = c^2 \, \nabla^2 p \tag{6.3}$$

A simple solution is the plane harmonic wave $p = p_a \cos(\omega t - kx)$, where p_a is the pressure amplitude, $\omega = 2\pi f$ is the angular frequency, and $k = 2\pi/\lambda$ is the wavenumber (Dera, 1992, Eq. 8.0.23).

The intensity of a harmonic plane wave is (Dera, 1992, Eq. 8.0.27):

Equation 14.4 — Effective sound intensity:

$$I_{\text{eff}} = \frac{p_a^2}{2\rho_0 c} \tag{6.4}$$

where the product $\rho_0 c$ is the *specific acoustic impedance* of the medium (Section 6.2.3).

Sound intensity is measured on a logarithmic scale (Dera, 1992, Eq. 8.0.28):

Equation 14.5 — Sound intensity level:

$$J = 10 \log_{10} \frac{I}{I_0} = 20 \log_{10} \frac{p}{p_0} \quad \text{[dB]} \tag{6.5}$$

where the modern hydroacoustic reference pressure is $p_0 = 1$ µPa.

6.2.2 Speed of Sound in Seawater

The speed of sound is the single most important acoustic parameter in the ocean. Dera (1992) derived it from fundamentals using the Newton–Laplace equation:

Equation 14.6 — Newton–Laplace equation for sound speed:

$$c = \frac{1}{\sqrt{k_{p,\sigma} \cdot \rho_0}} = \sqrt{\left(\frac{\partial p}{\partial \rho}\right)_{\sigma}} \tag{6.6}$$

where $k_{p,\sigma}$ is the adiabatic compressibility and ρ_0 is the undisturbed density (Dera, 1992, Eq. 8.0.14); for a concise treatment, see (Fischer-Cripps, 2014). Since both compressibility and density depend on temperature, salinity, and pressure, $c = c(S, T, p)$.

For practical computation, Dera (1992) presented Wilson's empirical formula:

Equation 14.7 — Wilson's sound speed formula (1960):

$$c(S,T,P) = 1449.14 + \Delta c_S + \Delta c_T + \Delta c_P + \Delta c_{S,T,P} \tag{6.7}$$

where the individual terms are (Dera, 1992, Eq. 8.1.3):

$$\Delta c_T = 4.5721\,T - 4.4532\times10^{-2}\,T^2 - 2.6045\times10^{-4}\,T^3 + 7.985\times10^{-6}\,T^4$$
$$\Delta c_S = 1.3980\,(S-35) + 1.692\times10^{-3}\,(S-35)^2$$
$$\Delta c_P = 1.60272\times10^{-1}\,P + 1.0268\times10^{-5}\,P^2 + 3.5216\times10^{-9}\,P^3 - 3.3603\times10^{-12}\,P^4$$

with cross-terms $\Delta c_{S,T,P}$; T in °C, S in ‰, P in kG/cm^2. The formula is accurate to ±0.3 m s^{-1} (Dera, 1992, Eq. 8.1.3).

A simpler expression due to Medwin is also given by Dera (1992, Eq. 8.1.4):

Equation 14.8 — Medwin's simplified sound speed formula (1975):

$$c = 1449.2 + 4.6\,T - 0.055\,T^2 + 0.00029\,T^3 + (1.34 - 0.010\,T)(S-35) + 0.016\,z \tag{6.8}$$

where c is in m s^{-1}, T in °C, S in ‰, and z is the depth in metres.

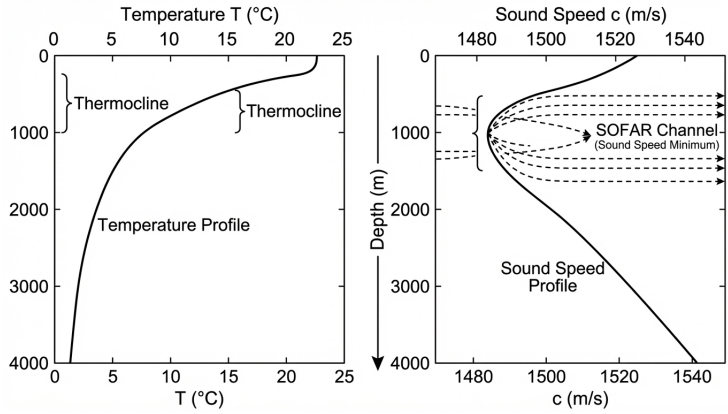

Figure 6.1: Vertical profiles of temperature (left) and sound speed (right) in the deep ocean. The speed of sound decreases through the thermocline as temperature falls (temperature-dominated regime), reaches a minimum at the SOFAR channel axis (~ 800 m), and then increases monotonically with depth as hydrostatic pressure dominates (Equation 6.8). The SOFAR channel traps sound by continuous refraction, enabling propagation over thousands of kilometres (Dera, 1992; Urick, 1983).

The sensitivity of speed to each variable is approximately (Dera, 1992): $+3.5$ m s^{-1} per 1 °C rise in temperature, $+1.3$ m s^{-1} per 1 ‰ increase in salinity, and $+1.6$–1.8 m s^{-1} per 100 m increase in depth.

6.2.3 Acoustic Impedance and Reflection

The specific acoustic impedance of a medium is defined as (Dera, 1992, Eq. 8.0.27):

Equation 14.9 — Acoustic impedance:

$$Z = \rho_0 \, c \quad [\mathrm{kg\,m^{-2}\,s^{-1}}] \tag{6.9}$$

For seawater with $\rho_0 \approx 1025\,\mathrm{kg\,m^{-3}}$ and $c \approx 1500\,\mathrm{m\,s^{-1}}$, the acoustic impedance is $Z \approx 1.54 \times 10^{6}$ Pa s m^{-1}. For air, $Z \approx 415$ Pa s m^{-1} (Dera, 1992). This enormous impedance mismatch means that more than 99.9% of acoustic energy is reflected at the air–sea interface, effectively confining underwater sound to the ocean and airborne sound to the atmosphere.

When a sound wave strikes a boundary between two media of different acoustic impedances $Z_1 = \rho_1 c_1$ and $Z_2 = \rho_2 c_2$, part of the energy is reflected and part is transmitted. For normal incidence, the pressure reflection coefficient is (Urick, 1983):

$$R = \frac{Z_2 - Z_1}{Z_2 + Z_1} \tag{6.10}$$

and the intensity reflection and transmission coefficients are $R_I = R^2$ and $T_I = 1 - R^2$ respectively (Medwin & Clay, 1998). At the sea surface, $Z_{\mathrm{air}}/Z_{\mathrm{sea}} \approx 2.7 \times 10^{-4}$, giving $R \approx -1$ and nearly total reflection with a phase reversal; the sea surface therefore acts as a pressure-release boundary for underwater sound (Urick, 1983).

At the seabed, the impedance ratio depends on the bottom material. Soft sediments (mud, silt) have impedances close to that of seawater ($Z_{\mathrm{sed}}/Z_{\mathrm{sea}} \approx 1.1$–$1.4$), yielding moderate reflection ($R_I \approx 0.01$–0.05). Hard substrates (rock, gravel) have much higher impedances ($Z_{\mathrm{sed}}/Z_{\mathrm{sea}} > 2$), producing strong reflections ($R_I > 0.1$) (Medwin & Clay, 1998). For oblique incidence at angle θ_1, the generalised reflection coefficient involves the acoustic impedance ratio and Snell's law, and a critical angle exists beyond which total internal reflection occurs if $c_2 > c_1$ (Jensen et al., 2011).

6.3 Theoretical Framework

6.3.1 Sonar Equation

The performance of any sonar system—whether active or passive—is assessed through the *sonar equation*, which compares the received signal level to the background noise or reverberation (Urick, 1983).

For an *active sonar* that transmits a pulse and listens for the echo, the sonar equation in decibels is (Urick, 1983):

$$\mathrm{SL} - 2\mathrm{TL} + \mathrm{TS} - (\mathrm{NL} - \mathrm{DI}) = \mathrm{DT} \tag{6.11}$$

where SL is the source level (intensity of the transmitted signal at 1 m from the source, in dB re 1 µPa at 1 m), TL is the one-way transmission loss (spreading plus absorption), TS is the target strength (the ratio of the intensity of the reflected signal at 1 m from the target to the incident intensity, in dB), NL is the

ambient noise level, DI is the receiving array directivity index (the improvement in signal-to-noise ratio achieved by the directional receiver over an omnidirectional hydrophone), and DT is the detection threshold (the minimum signal-to-noise ratio required for the operator or processor to detect the target) (Urick, 1983). Detection occurs when the left side equals or exceeds the right side. The factor of 2 on TL accounts for the two-way path (source to target and back).

For a *passive sonar* that listens for sound radiated by the target, the sonar equation reduces to (Urick, 1983):

$$\mathrm{SL} - \mathrm{TL} - (\mathrm{NL} - \mathrm{DI}) = \mathrm{DT} \tag{6.12}$$

where there is no target strength term (no transmitted pulse) and only one-way transmission loss. In this case SL refers to the source level of the target's own radiated noise (Urick, 1983).

6.3.2 Sound Propagation in the Ocean

The vertical sound speed profile creates refracting paths for acoustic rays. In much of the deep ocean, the speed of sound decreases with depth from the surface (due to cooling) down to a minimum at approximately 400–1200 m depth, and then increases again due to the dominant effect of hydrostatic pressure (Dera, 1992). This minimum defines the axis of the SOFAR (Sound Fixing and Ranging) channel, where sound is trapped by continuous refraction and can propagate over thousands of kilometres with low attenuation (Urick, 1983).

Acoustic ray theory provides the geometrical description of sound propagation in a range-dependent ocean. In a horizontally stratified medium where $c = c(z)$, the ray path is governed by Snell's law (Jensen et al., 2011):

$$\frac{\cos\theta(z)}{c(z)} = \frac{\cos\theta_0}{c_0} = \text{const.} \tag{6.13}$$

where $\theta(z)$ is the grazing angle (measured from the horizontal) at depth z, and θ_0, c_0 are the initial grazing angle and sound speed at the source depth. A ray launched at a small grazing angle is continuously bent toward the region of lower sound speed: in the thermocline, where c decreases with depth, the ray curves upward; below the SOFAR channel axis, where c increases with depth, the ray curves downward. The result is an oscillatory path that confines the ray to the sound channel (Jensen et al., 2011; Urick, 1983).

Several characteristic propagation features arise from this refraction (Urick, 1983):

- **Shadow zone:** A region beneath the thermocline into which rays from a shallow source cannot penetrate by direct refraction. The shadow boundary is defined by the limiting ray whose grazing angle at the source is zero.

- **Convergence zone:** At ranges of approximately 50–65 km (and at multiples thereof), refracted rays that have dived deep and curved back to the surface converge, producing a narrow annular zone of anomalously high intensity. Convergence zone propagation enables detection at long range with relatively modest source levels.

- **Surface and bottom bounce:** Rays that strike the sea surface or seabed are reflected and continue propagating. Each surface reflection involves a phase reversal (pressure-release boundary), while bottom reflections depend on the seabed impedance (Section 6.2.3). Bottom-bounce paths provide a useful propagation mode over intermediate ranges in shallow water (Urick, 1983).

For environments where ray theory is inadequate (low frequencies, shallow water), *normal mode theory* decomposes the acoustic field into a sum of discrete modes, each satisfying the depth-dependent wave equation with the boundary conditions at the surface and seabed. The nth mode propagates horizontally with a phase velocity $c_n > c_{\min}$ and a group velocity $v_{gn} < c_{\min}$, producing modal dispersion. The *parabolic equation* (PE) method provides an efficient numerical solution to the full-wave propagation problem, handling range-dependent bathymetry, sound speed, and sediment properties (Jensen et al., 2011).

6.3.3 Transmission Loss

Transmission loss in the ocean has two principal components: geometric spreading and absorption (Urick, 1983).

Absorption of sound intensity follows exponential decay along the propagation path (Dera, 1992, Eq. 8.2.1):

Equation 14.10 — Exponential absorption of sound:

$$I = I_0 \, e^{-\alpha_I r} \tag{6.14}$$

where I_0 is the initial intensity, r is the propagation distance, and α_I is the energetic absorption coefficient in m^{-1}.

In practice, absorption is more commonly expressed in decibels per metre. The conversions are (Dera, 1992, Eq. 8.2.5):

$$\alpha \ [\mathrm{dB/m}] = 8.686 \, \alpha_e \ [\mathrm{Np/m}] \tag{6.15}$$

Sound absorption in seawater arises from three distinct mechanisms (Dera, 1992):

1. **Molecular viscosity** (Stokes absorption): $\alpha_I \propto \eta \omega^2 / (\rho \, c^3)$, where η is the dynamic viscosity and ω the angular frequency. This produces a frequency-squared dependence (Dera, 1992, Eq. 8.2.6).

2. **Thermal conductivity** (Kirchhoff absorption): approximately $1/1000$ of viscous absorption in seawater (Dera, 1992, Eq. 8.2.7).

3. **Chemical relaxation**: the dominant mechanism at frequencies below approximately 100 kHz, involving structural relaxation of water molecule clusters ($\tau \sim 10^{-12}$ s), ionic relaxation of $MgSO_4$ ($\tau \sim 10^{-8}$ s, relaxation frequency ~ 100 kHz), and relaxation of boric acid $B(OH)_3$ ($\tau \sim 10^{-3}$ s, relaxation frequency ~ 1 kHz) (Dera, 1992).

The total absorption due to all relaxation processes is (Dera, 1992, Eq. 8.2.20):

Equation 14.12 — Total relaxation absorption coefficient:

$$\alpha_e = \sum_j \frac{A_j \, \omega^2 \, \tau_j}{1 + \omega^2 \, \tau_j^2} \tag{6.16}$$

where A_j is the participation fraction and τ_j is the relaxation time for each chemical process j.

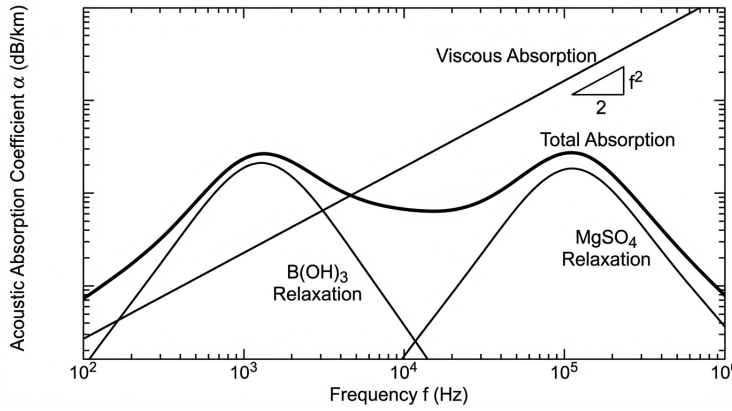

Figure 6.2: Frequency dependence of sound absorption in seawater at $T \approx 10\,^{\circ}\text{C}$, $S = 35$ ‰. Three mechanisms contribute: boric acid relaxation (dominant below ~ 1 kHz), magnesium sulphate relaxation (dominant at ~ 1–100 kHz), and viscous absorption (dominant above ~ 100 kHz). The total absorption coefficient (Equation 6.16) varies over many orders of magnitude across the frequency spectrum (Dera, 1992).

For transmission loss calculations, the total one-way transmission loss in decibels combines geometric spreading and absorption (Urick, 1983):

$$\text{TL} = n \, \log_{10}\!\left(\frac{r}{r_0}\right) + \alpha \, r \quad [\text{dB}] \tag{6.17}$$

where $n = 20$ for spherical spreading or $n = 10$ for cylindrical spreading (appropriate when sound is trapped in a waveguide such as the SOFAR channel

and spreads only in the horizontal plane), $r_0 = 1$ m is the reference distance, and α is the absorption coefficient in dB m^{-1} (Urick, 1983). At low frequencies ($f < 1$ kHz), the absorption term is small and geometric spreading dominates, permitting long-range propagation. At high frequencies ($f > 100$ kHz), absorption increases steeply ($\alpha \propto f^2$ in the viscous regime) and limits the useful range to a few hundred metres (Urick, 1983).

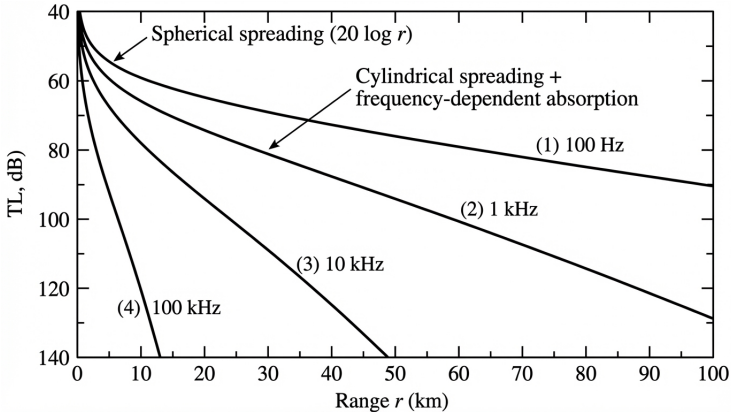

Figure 6.3: Transmission loss as a function of range for four representative frequencies, showing the combined effect of geometric spreading and frequency-dependent absorption (Equation 6.17). At low frequencies (0.1 kHz) absorption is negligible and sound can propagate over tens of kilometres; at high frequencies (100 kHz) absorption dominates and limits the effective range to a few kilometres (Campbell, 2025; Dera, 1992).

6.3.4 Ambient Noise in the Ocean

Urick (1983) identified three principal frequency bands dominated by different noise sources:

- **Below** 10 Hz: Microseisms, turbulent pressure fluctuations, and tidal currents. The spectral level decreases approximately as f^{-2} with increasing frequency.

- 10–500 Hz: Dominated by distant shipping noise, with spectral levels that depend on shipping density and range. In heavily trafficked waters, mean levels of 60–80 dB re 1 µPa^2 Hz^{-1} are typical; in remote ocean basins, levels are 10–20 dB lower (Urick, 1983).

- **Above** 500 Hz: Wind-generated surface noise, caused by breaking waves and spray, becomes the dominant source. The spectral level increases with wind speed: at sea state 6 (Beaufort 8), levels exceed those at sea state 1 by approximately 30 dB at 5 kHz. Rain and biological

sources (snapping shrimp in tropical and subtropical shallow waters) add further contributions at specific frequencies (Urick, 1983).

The composite spectral description of deep-water ambient noise, first compiled empirically as the *Wenz curves* (Urick, 1983), remains the standard reference for sonar system design. The ambient noise level NL appears directly in the sonar equations (Equations 6.11–6.12): higher noise levels require either higher source levels, greater directivity, or lower detection thresholds to achieve detection (Medwin & Clay, 1998; Urick, 1983).

6.3.5 Acoustic Doppler Effect

When a sound source and an observer are in relative motion, the observed frequency differs from the emitted frequency. Campbell (2025) gives the general Doppler equation:

Equation 14.14 — Doppler effect:

$$f_o = f_s \left(\frac{v \pm v_o}{v \mp v_s} \right) \tag{6.18}$$

where f_o is the observed frequency, f_s the source frequency, v the speed of sound in the medium, v_o the observer speed, and v_s the source speed. The upper signs apply when the source and observer approach each other; the lower signs when they recede (Campbell, 2025).

The Doppler effect is the operating principle of the *Acoustic Doppler Current Profiler* (ADCP). The instrument emits acoustic pulses at a known frequency and measures the frequency shift of signals backscattered by particles suspended in the water column. The velocity component along the beam axis is obtained from the fractional frequency shift:

$$v_{\text{current}} = \frac{\Delta f}{2 f_s}\, c$$

where the factor of 2 accounts for the two-way (transmit–receive) path. By transmitting along multiple beam directions, the three-dimensional current profile is reconstructed.

For a ship-mounted echo sounder pinging a seabed target while the vessel moves at speed v_s, the Doppler shift is typically negligible because $v_s \ll c_{\text{water}} \approx 1500\,\text{m s}^{-1}$. However, for submarine sonar tracking a torpedo moving at $v_s \approx 50\,\text{m s}^{-1}$, the shift is measurable and provides target speed information.

In multipath environments such as shallow water, the received signal consists of multiple delayed and Doppler-shifted copies of the transmitted signal, producing *Doppler spread* that broadens the received spectrum and complicates target velocity estimation. Modern sonar systems employ broadband waveforms and matched-filter processing to resolve the Doppler spread and extract velocity information from individual multipath arrivals (Jensen et al., 2011; Urick, 1983).

6.3.6 Reverberation

Reverberation is the unwanted return of acoustic energy scattered by the ocean boundaries and volume inhomogeneities, which can mask the target echo in an active sonar system. Urick (1983) distinguished three components:

- **Surface reverberation:** Scattering from the rough sea surface, whose strength increases with wind speed and sea state. The surface scattering strength S_s is expressed in dB per unit area and depends on the grazing angle and frequency.
- **Bottom reverberation:** Scattering from the seabed, governed by bottom roughness and the impedance contrast. Hard, rough bottoms (rock, gravel) produce strong reverberation; soft, smooth bottoms (mud) produce weak reverberation.
- **Volume reverberation:** Scattering from organisms, bubbles, and temperature microstructure distributed throughout the water column. The *deep scattering layer* (DSL), composed primarily of small fish and zooplankton, produces a prominent volume reverberation feature at depths of 300–$700\,\mathrm{m}$ during the day, migrating toward the surface at night (Urick, 1983).

The reverberation level at the receiver is a function of the source level, the scattering strength, the area (or volume) ensonified by the pulse, and the transmission loss to and from the scattering patch. When reverberation exceeds the ambient noise, the detection problem becomes *reverberation-limited* rather than noise-limited, and increasing the source level does not improve detection because both the echo and the reverberation increase proportionally (Urick, 1983).

6.4 Applications in Maritime Systems

6.4.1 Echo Sounding and Bathymetry

The echo sounder is the most fundamental acoustic instrument on a ship. It measures the water depth by emitting a short acoustic pulse vertically downward and measuring the two-way travel time t_{tw} to the seabed echo. The depth is (Medwin & Clay, 1998):

$$d = \frac{c\, t_{\mathrm{tw}}}{2} \tag{6.19}$$

where c is the mean sound speed over the water column and the factor of 2 accounts for the round trip. A *single-beam echo sounder* (SBES) measures depth at a single point beneath the vessel; typical operating frequencies are 12–$200\,\mathrm{kHz}$, with lower frequencies providing greater range (deep water) and

higher frequencies providing better resolution (shallow water) (Medwin & Clay, 1998).

A *multi-beam echo sounder* (MBES) emits a fan-shaped pulse and forms multiple receive beams across the swath, measuring depths simultaneously at many points on the seabed (Medwin & Clay, 1998). Typical swath widths are 3–6 times the water depth, enabling efficient full-coverage bathymetric surveys. The accuracy of multi-beam systems depends on the quality of the sound velocity profile used to correct for ray bending (Snell's law, Equation 6.13), the accuracy of the vessel's attitude (roll, pitch, heave) sensors, and the timing precision of the receiver electronics (Medwin & Clay, 1998).

6.4.2 Acoustic Doppler Current Profiler (ADCP)

The ADCP uses the Doppler effect (Equation 6.18) to measure the velocity of water currents at multiple depths simultaneously (Medwin & Clay, 1998). The instrument transmits acoustic pulses along three or four beams inclined at a fixed angle (typically $20°$–$30°$) from the vertical. Backscattered returns from suspended particles (plankton, sediment, bubbles) at each depth *bin* are Doppler-shifted in proportion to the radial velocity component along the beam. By combining the radial velocities from multiple beams, the three-dimensional current vector is reconstructed at each depth bin.

Ship-mounted (hull-mounted or lowered) ADCPs measure the current profile relative to the vessel; bottom-tracking or GPS integration provides the absolute current. *Bottom-mounted* (upward-looking) ADCPs are deployed as moored instruments for long-term current monitoring at fixed locations. Typical operating frequencies range from $38\,\text{kHz}$ (profiling range $> 1000\,\text{m}$, vertical resolution $\sim 16\,\text{m}$) to $1200\,\text{kHz}$ (profiling range $\sim 20\,\text{m}$, vertical resolution $\sim 0.5\,\text{m}$) (Medwin & Clay, 1998).

6.4.3 Sonar for Navigation and Obstacle Detection

Forward-looking sonar (FLS) transmits acoustic beams ahead of the vessel to detect obstacles (rocks, shoals, ice, other vessels) in the ship's path. Detection range depends on frequency, source level, and environmental conditions; typical ranges are 200–$500\,\text{m}$ at $200\,\text{kHz}$. FLS is particularly valuable in poorly charted waters and for vessels operating near grounding depths (Medwin & Clay, 1998).

Side-scan sonar (SSS) produces acoustic images of the seabed by transmitting narrow beams to port and starboard, perpendicular to the vessel's track. The backscattered intensity at each range position depends on the seabed material and roughness, producing a high-resolution acoustic photograph of the bottom. Side-scan imagery is used for wreck location, pipeline and cable surveys, mine detection, and habitat mapping. Typical operating frequencies are 100–$500\,\text{kHz}$, with higher frequencies giving finer along-track resolution at the cost of reduced range (Medwin & Clay, 1998).

Sub-bottom profilers transmit lower-frequency pulses (1–20 kHz) that penetrate the seabed and are partially reflected at interfaces between sediment layers of different acoustic impedance (Section 6.2.3). The resulting profile reveals the sub-surface geological structure, information essential for cable and pipeline routing, foundation design, and geotechnical site investigation (Jensen et al., 2011).

6.4.4 Underwater Communication

Underwater acoustic communication is the only practical means of wireless data transmission through the ocean over distances exceeding a few tens of metres (Medwin & Clay, 1998). The acoustic channel is, however, far more challenging than terrestrial radio: the available bandwidth is severely limited by frequency-dependent absorption (Equation 6.16), multipath propagation produces time-spread signals with delay spreads of 10–100 ms in shallow water, and relative motion between transmitter and receiver introduces Doppler shifts that distort the signal (Jensen et al., 2011).

Typical acoustic modem systems operate at carrier frequencies of 8–30 kHz with bandwidths of 1–10 kHz, achieving data rates of 0.1–10 kbit s^{-1} (orders of magnitude below terrestrial radio) over ranges up to 10 km. At shorter ranges ($<$ 100 m), higher carrier frequencies (100–200 kHz) permit higher data rates. Applications include diver-to-diver communication, ROV and AUV telemetry, sensor data retrieval from seabed instruments, and submarine communication (Medwin & Clay, 1998).

6.4.5 Underwater Radiated Noise (URN) and Environmental Impact

Ships radiate underwater noise through three principal mechanisms: propeller cavitation (the dominant source at most operating speeds), machinery vibration transmitted through the hull, and hydrodynamic flow noise over the hull surface (Urick, 1983). The radiated noise spectrum of a merchant vessel typically shows a broadband continuum with source levels of 170–190 dB re 1 µPa at 1 m and spectral peaks at the blade-rate frequency and its harmonics (Urick, 1983).

The environmental implications of ship-radiated noise are significant. Elevated ambient noise from shipping (the 10–500 Hz band described in Section 6.3.4) can mask the communication signals of marine mammals whose vocalisation frequencies overlap this band. Baleen whales, which use low-frequency calls (10–500 Hz) for long-range communication, are particularly affected; the increasing density of global shipping traffic has been shown to raise background noise levels in this band by 10–15 dB over the past half century (Medwin & Clay, 1998; Urick, 1983).

Noise reduction measures include propeller design modifications to delay the onset of cavitation, vibration isolation of main engines (resilient mounting), and hull fairing to reduce flow noise. The regulatory framework

linking these physics to environmental protection is treated in Chapter 8, and the propeller cavitation mechanism is analysed in the *Marine Propulsion Physics* chapter of the companion volume.

6.5 Discussion

The acoustic framework established in this chapter demonstrates the direct dependence of underwater sound on seawater thermodynamics: the speed of sound (Equation 6.6) depends on the same state variables—temperature, salinity, and pressure—that govern seawater density (Chapter 8). The three chemical relaxation mechanisms in seawater produce a complex frequency-dependent absorption that differs fundamentally from the simple viscous absorption of pure water.

The enormous acoustic impedance mismatch at the air–sea interface ($Z_{\text{sea}}/Z_{\text{air}} \approx 3700$) explains why acoustic and electromagnetic methods occupy complementary niches in ocean science: sound for long-range subsurface observation, and electromagnetic radiation for atmospheric and near-surface remote sensing (Medwin & Clay, 1998; Urick, 1983).

The sonar equations (Equations 6.11–6.12) distil the entire detection problem into a balance sheet of decibels, yet each term encapsulates substantial physics: the source level depends on transducer efficiency and electrical drive power; the transmission loss integrates the ray-bending effects of Snell's law (Equation 6.13), the frequency-dependent chemical relaxation absorption (Equation 6.16), and the geometric spreading regime (spherical at short range, cylindrical in waveguide propagation); the ambient noise level is set by the composite contributions of shipping, wind, and biology (the Wenz curves); and the target strength depends on the geometry, size, and material properties of the reflecting object (Urick, 1983).

The computational ocean acoustics framework of Jensen et al. (2011)—ray tracing, normal modes, and the parabolic equation method—provides the numerical tools to solve the propagation problem in realistic, range-dependent environments where analytic solutions are unavailable. These methods are essential for predicting sonar performance in complex environments such as continental shelf regions with variable bathymetry, sound speed fronts, and layered sediments. The continued increase in computational power has made full three-dimensional acoustic modelling feasible for operational sonar prediction, a development that would have been impractical with the two-dimensional methods available when Urick (1983) wrote the foundational text.

6.6 Conclusion

Underwater acoustics is governed by the dependence of sound speed on the thermodynamic state of seawater: the Newton–Laplace equation (Equa-

tion 6.6) and Wilson's empirical formula (Equation 6.7) yield typical ocean values of 1430–$1580\,\mathrm{m\,s^{-1}}$, with temperature the dominant variable ($+3.5\,\mathrm{m\,s^{-1}}$ per °C) (Dera, 1992). The resulting vertical sound speed profile—decreasing through the thermocline and increasing under hydrostatic pressure—creates the SOFAR channel at approximately 400–$1200\,\mathrm{m}$ depth, where continuous refraction traps acoustic energy and enables propagation over thousands of kilometres (Urick, 1983). The enormous acoustic impedance mismatch at the air–sea interface ($Z_{\text{sea}}/Z_{\text{air}} \approx 3700$, Equation 6.9) effectively confines underwater sound to the ocean.

Transmission loss combines geometric spreading—spherical divergence yields -6 dB per doubling of distance—with frequency-dependent absorption arising from three chemical relaxation processes: boric acid ($f_r \sim 1\,\mathrm{kHz}$), magnesium sulphate ($f_r \sim 100\,\mathrm{kHz}$), and viscous losses at higher frequencies (Equations 6.16 and 6.17) (Campbell, 2025; Dera, 1992). The Doppler effect (Equation 6.18) underpins the Acoustic Doppler Current Profiler (ADCP), in which the fractional frequency shift of backscattered signals yields current velocity profiles throughout the water column (Campbell, 2025).

References

Campbell, C. (2025). *Physics: A focused introduction*. CRC Press. https://doi.org/10.1201/9781003571568

Dera, J. (1992). *Marine physics* (P. Senn, Trans.) [Translated from Polish. Original: *Fizyka morza*, 1983]. Elsevier.

Fischer-Cripps, A. C. (2014). *The physics companion* (2nd ed.). CRC Press. https://doi.org/10.1201/b17356

Hewitt, P. G., Suchocki, J. A., & Hewitt, L. A. (2012). *Conceptual physical science* (5th ed.). Pearson.

Jensen, F. B., Kuperman, W. A., Porter, M. B., & Schmidt, H. (2011). *Computational ocean acoustics* (2nd ed.). Springer. https://doi.org/10.1007/978-1-4419-8678-8

Medwin, H., & Clay, C. S. (1998). *Fundamentals of acoustical oceanography*. Academic Press.

Urick, R. J. (1983). *Principles of underwater sound* (3rd ed.). McGraw-Hill.

Chapter 7

Maritime Safety and Risk Physics

7.1 Introduction

Maritime safety engineering rests on the application of physical principles—mechanics, thermodynamics, fluid dynamics, and probability theory—to the prevention and mitigation of accidents at sea (Kristiansen, 2005). The International Convention for the Safety of Life at Sea (SOLAS) provides the regulatory framework, which has evolved from prescriptive rules based on lessons learned from individual disasters to goal-based standards rooted in quantitative risk assessment.

A comprehensive statistical analysis of ship accidents in the period 1990–2012, covering 10,841 serious casualty records across all major ship types, reveals that hull and machinery damage accounts for approximately 37% of all incidents, followed by wrecked/stranded events (21%) and collisions (20%) (Guedes Soares & Santos, 2015). The total losses during this period amounted to 940 vessels, with 6,569 persons lost. These figures highlight the practical importance of understanding the physics of structural failure, flooding, fire, and collision—the subjects of this chapter.

The regulatory philosophy underlying SOLAS has evolved from *prescriptive* rules—which specify exact structural scantlings, subdivision arrangements, and equipment lists—to *goal-based standards* (GBS), which define the safety objective and let the designer choose the means of compliance (Kristiansen, 2005). In a GBS framework, the designer demonstrates that the risk associated with a proposed design is below an acceptable level, using quantitative tools such as fault tree analysis, event tree analysis, and probabilistic damage stability assessment. This approach encourages innovation and permits optimisation of the safety solution for each vessel type (Kristiansen, 2005).

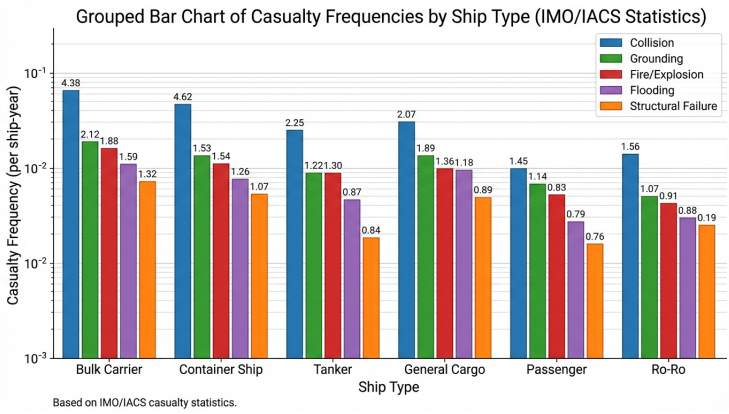

Figure 7.1: Serious casualty frequencies by ship type for the period 1990–2012, based on 10,841 records across 602,998 cumulative ship-years (Equation 7.1). Cruise ships exhibit the highest frequency among all types ($f = 4.23 \times 10^{-2}$ per ship-year), while Ro-Ro cargo ships and car carriers dominate the cargo vessel categories (Guedes Soares & Santos, 2015).

7.2 Scientific Background

7.2.1 Risk Concepts and Probability Theory

In the maritime context, risk is defined as the product of the probability of an accident and the severity of its consequences (Kristiansen, 2005; Rausand, 2014). Guedes Soares and Santos (2015) present frequency-based risk measures derived from the analysis of 10,841 serious accidents over 602,998 cumulative ship-years of exposure for 13 ship types.

The accident frequency is computed as:

Equation 15.1 — Accident frequency:

$$f = \frac{N_{\text{accidents}}}{N_{\text{ship-years}}} \tag{7.1}$$

where $N_{\text{accidents}}$ is the number of serious casualty events for a given ship type and $N_{\text{ship-years}}$ is the cumulative operational fleet exposure in ship-years (Guedes Soares & Santos, 2015).

For cargo vessels, the highest overall accident frequencies were observed for Ro-Ro cargo ships ($f = 2.93 \times 10^{-2}$ per ship-year) and car carriers ($f = 2.68 \times 10^{-2}$), while for passenger vessels, cruise ships exhibited the highest frequency ($f = 4.23 \times 10^{-2}$ per ship-year) (Guedes Soares & Santos, 2015).

A critical consequence metric is the Potential Loss of Life (PLL), defined as the number of fatalities per ship-year. Passenger Ro-Ro cargo vessels showed the highest PLL at 1.24×10^{-1} fatalities per ship-year, reflecting

the catastrophic potential of flooding events involving ships carrying large numbers of persons (Guedes Soares & Santos, 2015).

The cumulative risk to a population exposed to a hazard is represented by the *FN curve*, which plots the annual frequency F of accidents causing N or more fatalities against N on logarithmic axes (Rausand, 2014). A risk acceptance criterion is then a boundary line on the FN diagram: activities whose FN curve lies entirely below the boundary are deemed tolerable. For the maritime industry, Kristiansen (2005) reports that the individual risk acceptance level applied in IMO Formal Safety Assessment studies is approximately 10^{-4} per year for crew members and 10^{-5} per year for passengers, reflecting the principle that people who do not choose the hazard (passengers) should be exposed to lower risk than those who do (seafarers).

Between the clearly acceptable and clearly unacceptable risk regions lies the *ALARP* (As Low As Reasonably Practicable) zone. Within this zone, further risk reduction measures are required unless the cost of implementing them is *grossly disproportionate* to the safety benefit gained (Kristiansen, 2005; Rausand, 2014). The ALARP principle is central to the IMO's Formal Safety Assessment methodology (Section 7.4.5).

7.2.2 Fire Physics Fundamentals

Fire requires three elements: a combustible material (fuel), an oxidiser (oxygen), and an ignition source of sufficient energy to initiate combustion. The *fire triangle* provides the conceptual basis for all fire prevention and suppression strategies: remove any one element and the fire cannot be sustained (Kristiansen, 2005).

In an enclosed ship compartment, a fire develops through distinct phases: ignition, growth, flashover, fully developed fire, and decay (Molland, 2008). During the growth phase, the rate of heat release increases as the fire spreads across the fuel surface. *Flashover* occurs when the upper layer of hot gases radiates sufficient thermal flux ($\sim 20\,\mathrm{kW\,m^{-2}}$) to ignite all exposed combustible surfaces simultaneously, transitioning the fire from localised burning to fully involved compartment fire (Molland, 2008). After flashover, compartment temperatures may exceed $1000\,^{\circ}\mathrm{C}$, and the fire becomes ventilation-controlled: the rate of combustion is limited by the supply of fresh air through openings rather than by the fuel surface area (Kristiansen, 2005).

Smoke stratification in ship compartments follows the physics of buoyant plumes. The hot combustion products rise to the ceiling, forming a layer that descends as the fire progresses. In a corridor or stairwell, smoke can travel horizontally and descend through vertical openings, reducing visibility and producing toxic conditions far from the fire origin. The fundamental combustion thermodynamics—heat release rate, flame temperature, and heat transfer mechanisms—are developed in the *Thermodynamics in Marine Engineering*

chapter of the companion volume; this chapter focuses on the safety engineering implications.

7.2.3 Explosion Mechanics Fundamentals

An explosion is a rapid release of energy that produces a pressure wave. Two regimes are distinguished by the propagation speed of the combustion front (Kristiansen, 2005). In a *deflagration*, the flame front propagates through the unburnt mixture at a velocity below the speed of sound (subsonic), driven by thermal conduction and molecular diffusion. In a *detonation*, the combustion front couples with a shock wave and propagates at supersonic velocity, producing overpressures an order of magnitude greater than those from a deflagration of the same fuel–air mixture.

The peak overpressure Δp and its duration t_d determine the structural response. At distances far from the explosion centre, the blast wave approximates a decaying exponential pressure–time history superimposed on the ambient pressure (Kristiansen, 2005). For shipboard enclosed spaces—engine rooms, cargo holds, void spaces where flammable vapours may accumulate—the confinement amplifies the overpressure because the expanding combustion products cannot vent freely. Hydrocarbon vapour–air mixtures (e.g. cargo tank atmospheres) are explosive within a flammability range that, for methane, lies between approximately 5% and 15% by volume in air (Kristiansen, 2005). Inerting systems that maintain the oxygen concentration below the *limiting oxygen concentration* (LOC) prevent ignition regardless of the fuel concentration.

7.3 Theoretical Framework

7.3.1 Flooding and Damage Stability

The probabilistic approach to damage stability, now mandated by SOLAS Chapter II-1, replaces the earlier deterministic methodology with a framework that accounts for the statistical distribution of damage extent and the probability of survival in the damaged condition.

Guedes Soares and Santos (2015) describe the methodology in which the ship must achieve an attained subdivision index A that exceeds a required index R. The attained index aggregates partial indices evaluated at three loading draughts—deepest subdivision, partial, and light service—through a weighted sum (as formulated in the *Ship Stability and Hydrostatics* chapter of the companion volume). Each partial index sums the products of a probability factor $p_{i,j}$ (derived from the statistical distribution of damage length, penetration, and longitudinal location) and a survival factor $s_{i,j}$ (based on the residual GZ curve) over all feasible damage scenarios (Guedes Soares & Santos, 2015).

The survival factor $s_{i,j}$ captures the physics of damaged floating body equilibrium: a ship survives if the residual stability provides sufficient

righting moment to resist external heeling moments from wind, passenger crowding, and lifeboat launching. The minimum of the intermediate-stage and final-stage survival factors is selected for each damage case (Guedes Soares & Santos, 2015).

The deterministic damage stability methods described in the following subsections provide the physical foundation for understanding flooding consequences.

Lost Buoyancy Method

The classical deterministic approach to damage stability is the *lost buoyancy* method, described by Attwood (1917) and further developed by Rawson and Tupper (2001). When a compartment is bilged (opened to the sea), the buoyancy provided by that compartment is lost. The vessel sinks bodily until the remaining intact waterplane area provides sufficient displaced volume to restore equilibrium.

For a box-shaped vessel of length L, breadth B, and constant draught T, bilging a compartment of length l over half the breadth gives a volume of lost buoyancy $v_{\text{lost}} = l \times T \times (B/2)$. The bodily sinkage is (Attwood, 1917):

$$\delta T = \frac{v_{\text{lost}}}{A_{\text{intact}}}$$

where A_{intact} is the area of the intact waterplane after damage. If the damage is asymmetric (e.g. one side of a centreline bulkhead), the centroid of the intact waterplane shifts laterally and the vessel heels until the centre of gravity and the new metacentre are in the same vertical line (Attwood, 1917).

Rawson and Tupper (2001) formalise the lost buoyancy method by computing the new metacentric height after damage:

$$\text{GM}_{\text{damaged}} = \frac{\rho\,(I_{\text{intact}} - i_{\text{fs}})}{\Delta} - \overline{BG} + \delta BG$$

where I_{intact} is the second moment of the intact waterplane about the centreline, i_{fs} is the free-surface moment of the floodwater in the damaged compartment, Δ is the displacement (unchanged in the lost buoyancy approach), and δBG accounts for the change in the vertical distance between buoyancy centre and gravity (Rawson & Tupper, 2001). The permeability μ of the damaged compartment—the fraction of the compartment volume available for flooding—modifies the effective lost buoyancy: typical values are 0.95–0.97 for empty watertight spaces, 0.85 for machinery spaces, and 0.60–0.70 for cargo holds (Attwood, 1917; Rawson & Tupper, 2001).

Added Weight Method

The alternative deterministic approach treats the floodwater as an added weight rather than as lost buoyancy. Rawson and Tupper (2001) describe

the procedure: the weight of floodwater w at its centre of gravity is added to the ship's displacement, producing a new displacement $\Delta + w$, a new centre of gravity, and a new waterline. The added weight method is numerically equivalent to the lost buoyancy method but can be more convenient when the floodwater weight is known directly (e.g. from the volume of the compartment and its permeability) (Rawson & Tupper, 2001).

Floodable Length and Margin Line

Biran (2003) formalise the concept of *floodable length*: the maximum length of compartment, centred at any point along the ship's length, that may be flooded without the vessel sinking below the *margin line*—a line drawn 76 mm below the upper surface of the bulkhead deck at the ship's side. For a given permeability μ, the floodable length at each longitudinal position is obtained by trial: damaged waterlines are computed for progressively longer compartments until the margin line is just reached. Plotting the floodable length along the ship produces a *floodable-length curve* whose minima indicate the most critical positions for subdivision. The required number of watertight bulkheads is determined by dividing the ship into compartments whose lengths do not exceed the permissible length—the floodable length reduced by a *factor of subdivision* F ($F \leq 1$), which is a function of the ship's length and the nature of its service (Biran, 2003). This deterministic subdivision design procedure, although now supplemented by the probabilistic attained index (as formulated in the *Ship Stability and Hydrostatics* chapter of the companion volume), remains the basis for understanding how watertight bulkhead spacing is established.

7.3.2 Fire Dynamics on Ships

Fire development in ship compartments is modelled at two levels of complexity (Molland, 2008). *Zone models* divide the compartment into a small number of control volumes—typically a hot upper layer and a cooler lower layer—and solve conservation equations for mass, energy, and chemical species within each zone. Zone models are computationally efficient and provide estimates of layer temperature, smoke depth, and toxic gas concentrations that are adequate for design-stage safety assessment.

Field models (CFD) solve the full Navier–Stokes equations with turbulence and combustion sub-models on a three-dimensional computational grid. They capture the detailed flow patterns, recirculation zones, and local temperature gradients that zone models cannot resolve—for example, the interaction of a fire plume with the ship's ventilation system or the flow of smoke through partially open watertight doors. The computational cost is substantially higher, but CFD is increasingly used for performance-based fire safety design (Molland, 2008).

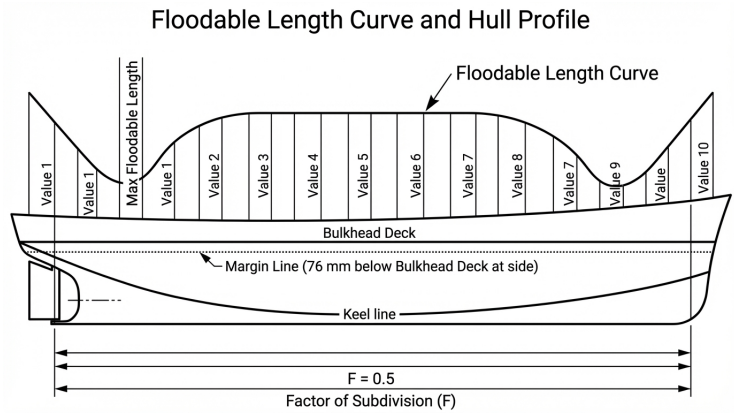

Figure 7.2: Schematic floodable length curve showing the maximum compartment length that may be flooded at each longitudinal position without exceeding the margin line. The permissible length (dashed) is the floodable length reduced by the factor of subdivision F. Watertight bulkheads (green lines) must be spaced so that no compartment exceeds the permissible length; the most critical region is near amidships where the floodable length reaches its minimum (Biran, 2003).

The thermal response of the steel structure surrounding a fire determines whether the structural integrity of decks and bulkheads is maintained. Steel loses approximately half its yield strength at $550\,^{\circ}\mathrm{C}$ (Hughes & Paik, 2010). Fire insulation (A-class divisions per SOLAS) is designed to keep the unexposed face temperature below $140\,^{\circ}\mathrm{C}$ rise after $60\,\mathrm{min}$ of standard fire exposure, providing time for firefighting and evacuation (Kristiansen, 2005). The underlying heat transfer physics—conduction through insulation and steel, radiation from the hot gas layer—draws on the principles developed in the *Thermodynamics in Marine Engineering* chapter of the companion volume.

7.3.3 Explosion and Blast Loading

The accumulation of flammable gas in enclosed shipboard spaces is a prerequisite for a vapour cloud explosion. Gases heavier than air (e.g. hydrocarbon vapours, hydrogen sulphide) accumulate in the lower parts of compartments, while lighter gases (e.g. methane, hydrogen) rise and collect below deckheads (Kristiansen, 2005). Adequate ventilation—natural or mechanical—must ensure that the gas concentration remains below the Lower Explosive Limit (LEL) at all points within the space.

If an explosive mixture is ignited in a partially confined space (e.g. a cargo pump room or an enclosed section of a product tanker), the pressure generated depends on the degree of confinement, the fuel–air stoichiometry, the presence of turbulence-generating obstacles, and the ignition location. Turbulence produced by flow past structural members (piping, gratings, equipment)

can accelerate the flame front, increasing the overpressure above that of a laminar deflagration by a factor of 5–10 (Kristiansen, 2005).

The structural response to blast loading is governed by the *pressure–impulse* (P–I) interaction: a thin panel may survive a high overpressure of very short duration (impulse-controlled regime) or a moderate overpressure of long duration (quasi-static regime), but fails when both pressure and impulse exceed the panel's resistance (Hughes & Paik, 2010). Blast-resistant bulkheads on offshore vessels and FPSOs are designed to withstand specified overpressure–duration combinations derived from explosion consequence analysis.

7.3.4 Collision Mechanics

Guedes Soares and Santos (2015) present a systematic analysis of collision events using the Technique for the Retrospective and predictive Analysis of Cognitive Errors in maritime transportation (TRACEr-MAR). Of 12 collision cases analysed from official investigation reports, 99% of the bridge team errors involved the "execution" cognitive domain—that is, errors in carrying out planned actions rather than in situational awareness or decision-making per se (Guedes Soares & Santos, 2015).

The leading error-producing conditions for collisions were traffic monitoring failures (27%), inappropriate lookout method (15%), and inadequate lookout technique (15%). These results indicate that the physics of collision prevention—radar target detection, visual observation geometry, and the kinematics of relative motion between vessels—are critical factors in the accident causal chain (Guedes Soares & Santos, 2015).

The collision event is conventionally divided into *external mechanics* (the rigid-body dynamics of the two vessels before and during contact) and *internal mechanics* (the structural deformation and energy absorption at the contact zone) (Rawson & Tupper, 2001).

In the external mechanics phase, the kinetic energy available for structural damage is $E_k = \tfrac{1}{2}(1 + C_a)\, m\, V^2$ (as given above), where the added mass coefficient C_a accounts for the entrained water that moves with the vessel. The collision angle determines how the kinetic energy is partitioned between the striking and struck vessels: a right-angle collision transfers the maximum energy to the struck vessel's side shell, while a glancing blow dissipates energy in sliding friction and the vessels' rotational kinetic energy (Rawson & Tupper, 2001).

In the internal mechanics phase, the striking vessel's bow crushes into the struck vessel's side structure. The energy absorbed by structural deformation depends on the resistance of the side shell, frames, and inner barriers (double hull). Molland (2008) note that the classical method of Rawson and Tupper (2001) estimates the volume of damaged material and correlates it empirically with the absorbed energy. Modern finite element analysis models the progressive collapse of the structure under the indenting bow, capturing the sequence of membrane stretching, folding, and rupture of

individual structural members. The critical outcome is whether the inner hull (if present) is breached, leading to cargo outflow or flooding of internal compartments (Rawson & Tupper, 2001).

The structural mechanics of collision are also treated in Section 5.4.4. Rawson and Tupper (2001) note that the kinetic energy available for structural damage is:

$$E_k = \tfrac{1}{2}\,(1 + C_a)\,m\,V^2$$

where m is the striking vessel's displacement, V is the speed at contact, and C_a is the added mass coefficient ($C_a \approx 0.1$ for longitudinal motion, $C_a \approx 0.4$ for lateral motion) (Rawson & Tupper, 2001). The added mass increases the effective kinetic energy by 10–40% above the value computed from the vessel's physical mass alone.

7.3.5 Grounding Mechanics

Grounding events involve the interaction between a ship's bottom structure and the seabed. The TRACEr-MAR analysis of 17 grounding cases reported in Guedes Soares and Santos (2015) identified that 35% of the errors contributing to groundings occurred in the "supervision" cognitive domain, indicating failures in monitoring the vessel's navigational progress and verifying compliance with the planned track. A further 23% of errors were attributed to the "situation assessment" domain—failures to correctly interpret available navigational information (Guedes Soares & Santos, 2015).

These cognitive error patterns have direct physical implications: inaccurate position estimation leads to insufficient under-keel clearance, while failures in monitoring tidal height and bathymetric data result in contact with charted hazards. The physics of the ship–seabed interaction then determines the structural consequences.

Rawson and Tupper (2001) distinguish two grounding scenarios with different structural consequences. In *stranding*, the ship grounds over a large area and comes to rest; the hull girder experiences a change in the shearing force and bending moment distributions because the ground reaction replaces the buoyancy lost by the grounded region. In *bottom raking*, the ship moves forward over a sharp obstruction (rock, reef, or wreck), opening the bottom shell along a considerable length. The energy absorbed by the double-bottom structure—floors, inner bottom, and longitudinal girders—determines the extent of penetration. Modern double-hull requirements (MARPOL Annex I) provide an additional structural barrier that increases the energy absorption capacity and reduces the probability of cargo outflow (Rawson & Tupper, 2001).

7.4 Applications in Maritime Systems

7.4.1 Life-Saving Appliance Physics

The physics of life-saving appliances encompasses the dynamics of lifeboat launching, the mechanics of recovery systems, and the thermophysiology of cold-water survival. A gravity davit operates by releasing the lifeboat from its stowed position and allowing it to swing outboard under gravity along a curved track. The lifeboat must clear the ship's side at any list up to 20° and at any trim (Kristiansen, 2005). During free-fall launch, the lifeboat slides down a ramp and enters the water at a speed determined by the ramp angle and height: for a ramp height of 15 m at 35° inclination, the entry speed is approximately 10–12 m s^{-1}, and the occupants experience deceleration loads of 6–$9\,g$ on water entry (Molland, 2008).

Man-overboard recovery time is a critical safety metric. A person immersed in seawater at $5\,^\circ$C can lose consciousness due to hypothermia within 30–60 min and survive no more than 1–3 h without thermal protection, because the thermal conductivity of water (~ 0.6 W m^{-1} K^{-1}) is approximately 25 times that of still air, producing rapid core cooling (Molland, 2008); for a concise treatment, see (Fischer-Cripps, 2014). Lifejackets provide flotation but minimal thermal insulation; immersion suits extend survival time by reducing convective heat loss. The Williamson turn manoeuvre (Section 7.5) enables the vessel to return to the person's position, and the manoeuvring performance required for this evolution connects to the IMO manoeuvring standards discussed by Sutulo and Guedes Soares (2023).

7.4.2 Quantitative Risk Assessment (QRA)

A quantitative risk assessment proceeds through a structured sequence: hazard identification, frequency estimation, consequence modelling, and risk evaluation (Kristiansen, 2005).

Fault tree analysis (FTA) is a top-down deductive method that models the causal pathways leading to a defined *top event* (e.g. engine room fire). The top event is decomposed through logic gates (AND, OR) into intermediate and basic events. The probability of the top event is computed from the basic event probabilities using Boolean algebra (Rausand, 2014). For example, an engine room fire requires both an ignition source AND a flammable atmosphere; the latter requires a fuel leak AND inadequate ventilation.

Event tree analysis (ETA) is a forward-looking inductive method that traces the sequence of events following an initiating event (e.g. loss of propulsion). At each branching node, the system either succeeds or fails in executing a safety barrier (e.g. anchor deployment, tug assistance). The end states of the event tree represent the possible outcomes (safe recovery, grounding, collision), each with an associated probability (Kristiansen, 2005; Rausand, 2014).

The combination of FTA (for frequency estimation) and ETA (for consequence propagation) provides the quantitative basis for computing the risk metrics described in Section 7.2.1: the expected annual frequency of each outcome, the PLL, and the FN curve (Kristiansen, 2005).

Quantitative risk assessment extends beyond event-frequency analysis (Equation 7.1) to encompass the *structural* dimension of safety: the probability that the hull girder will sustain the loads imposed during its operational lifetime. Decò et al. (2012) developed a probabilistic framework that combines wave load analysis, time-variant structural degradation, and reliability theory to compute the probability of hull girder failure under different operational conditions (headings, speeds, and sea states).

Structural Reliability as a Safety Metric

The structural reliability index β, defined as (Decò et al., 2012):

Equation 15.2 — Structural reliability index:

$$\beta = \Phi^{-1}(1 - P_f) \tag{7.2}$$

where Φ^{-1} is the inverse standard normal cumulative distribution function and P_f is the probability of structural failure, provides a single scalar measure that integrates all sources of uncertainty: loading randomness, material variability, geometric imperfections, and modelling error (Decò et al., 2012). A reliability index of $\beta = 3.0$ corresponds to $P_f \approx 1.35 \times 10^{-3}$; $\beta = 4.0$ corresponds to $P_f \approx 3.17 \times 10^{-5}$.

The failure probability is evaluated from the limit state function $g = R - S$, where R is the structural resistance (ultimate hull girder capacity) and S is the total applied load (still water plus wave-induced bending moment). The First-Order Reliability Method (FORM) linearises the failure surface $g = 0$ in standard normal space and computes β as the shortest distance from the origin to this surface (Decò et al., 2012).

Redundancy as a Safety Measure

A safety-critical structure should not only have adequate reliability against ultimate failure but should also possess *redundancy*—the ability to sustain loads after partial component failure. Decò et al. (2012) define two redundancy indices:

Equation 15.3 — Redundancy index (intact reserve):

$$RI_1 = \frac{\beta_{\text{intact}} - \beta_{\text{first}}}{\beta_{\text{intact}}} \tag{7.3}$$

Equation 15.4 — Redundancy index (residual capacity):

$$RI_2 = \frac{\beta_{\text{damaged}} - \beta_{\text{first}}}{\beta_{\text{damaged}}} \tag{7.4}$$

where β_{intact} is the reliability index for ultimate system collapse, β_{first} is the reliability index for first component failure (initial yielding or buckling), and β_{damaged} is the reliability index for the system with one failed component (Decò et al., 2012). When $RI_1 = 0$, the system is non-redundant: first element failure immediately triggers system collapse. Positive values indicate that the structure has reserve capacity to redistribute loads after local failure.

Decò et al. (2012) demonstrated these concepts for a joint high-speed sealift vessel ($L = 290\,\text{m}$, $B = 32\,\text{m}$) operating across all headings and sea states. The polar representations of β and RI showed that the lowest reliability occurred in head seas at high speed, where the wave-induced bending moments are largest. The time-variant analysis revealed that after 25 years of corrosion, the reliability index dropped from approximately 5.3 to 3.1 for the critical heading, while redundancy indices declined correspondingly, highlighting the need for inspection-based maintenance scheduling informed by reliability predictions (Decò et al., 2012).

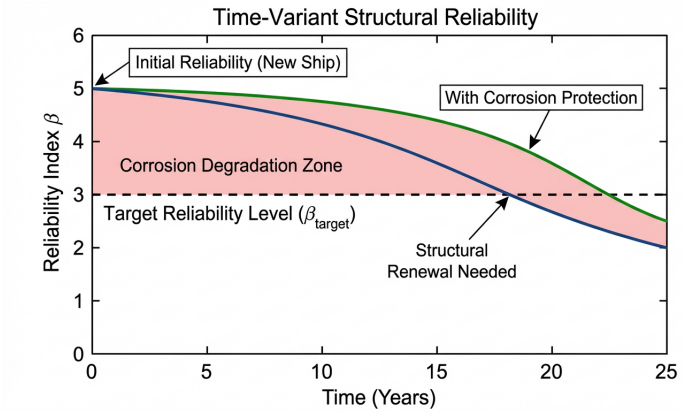

Figure 7.3: Time-variant structural reliability under corrosion. The reliability index β (Equation 7.2) declines after coating breakdown at $T_c \approx 7$ years as the corrosion depth $r(t) = C_1(t - T_c)^{C_2}$ gradually reduces plate thickness and hull girder capacity. For a high-speed sealift vessel, β falls from approximately 5.3 at commissioning to 3.1 after 25 years, approaching the minimum target $\beta = 3.0$ (Decò et al., 2012).

7.4.3 Fire Detection and Suppression Systems

Fire detection systems exploit the physical signatures of combustion: heat, smoke, and infrared/ultraviolet radiation. *Thermal detectors* respond when the local temperature exceeds a threshold (typically 57–$77\,^\circ\text{C}$) or when the rate of temperature rise exceeds a set value. *Optical smoke detectors* sense the scattering of a light beam by smoke particles (photoelectric type) or the reduction in ionisation current caused by smoke entering an ionisation chamber (Kristiansen, 2005). *Flame detectors* respond to the ultraviolet or

infrared radiation emitted by open flames. The choice of detector depends on the expected fire development rate and the compartment environment: ionisation detectors respond quickly to fast-flaming fires, while photoelectric detectors are more sensitive to slow-smouldering fires typical of cable insulation (Molland, 2008).

Sprinkler systems use fusible-link or glass-bulb nozzles that open individually when the local ceiling temperature reaches the rated activation temperature (commonly $68\,^{\circ}\text{C}$ or $79\,^{\circ}\text{C}$). The discharged water spray absorbs heat from the fire gases and wets the surrounding surfaces, controlling fire growth and preventing flashover (Kristiansen, 2005).

Water mist systems generate fine droplets ($< \quad 200\,\mu\text{m}$ diameter) that extinguish fires through a combination of evaporative cooling, oxygen displacement by steam, and radiation attenuation. Water mist is effective in enclosed machinery spaces and is increasingly adopted as an alternative to CO_2 flooding, which presents an asphyxiation risk to personnel (Molland, 2008). *High-expansion foam systems* are used in large-volume spaces (vehicle decks, cargo holds) where the foam blanket smothers the fire by separating the fuel surface from the oxygen supply (Kristiansen, 2005).

7.4.4 Watertight Integrity

The maintenance of watertight integrity is a prerequisite for both intact and damage stability. Watertight bulkheads must be capable of withstanding a head of water up to the bulkhead deck; the structural scantling requirements are determined by the hydrostatic pressure at the lowest point of the bulkhead, $p = \rho g h$, where h is the head of water (Rawson & Tupper, 2001).

Watertight doors penetrating subdivision bulkheads are potential weak points in the watertight envelope. SOLAS requires that these doors be operable from a central control station on the bridge and be capable of closing against a heel of up to 15°. Sliding watertight doors are hydraulically or electrically powered, with a closure time not exceeding 60 s and local manual override capability (Kristiansen, 2005).

Periodic hydrostatic testing of watertight boundaries—pressurising compartments with water or air and inspecting for leakage—verifies that the watertight envelope remains intact. Corrosion of the shell plating, deterioration of gaskets, and mechanical damage to door sealing surfaces are common causes of watertight integrity failure. Hull integrity monitoring systems, using strategically placed water ingress sensors in double-bottom and void spaces, provide early warning of flooding before the crew becomes aware through inclination changes (Molland, 2008).

7.4.5 Formal Safety Assessment (FSA)

The IMO Formal Safety Assessment (FSA) provides a structured methodology for evaluating the safety of shipping and for formulating regulatory propos-

als (Kristiansen, 2005). The FSA process consists of five steps:

1. **Hazard identification:** systematic identification of all relevant hazards (collision, grounding, fire, flooding, structural failure) through techniques such as HAZID workshops and analysis of accident databases.

2. **Risk analysis:** quantification of frequency and consequence for each hazard scenario, using fault tree and event tree methods (Section 7.4.2) and statistical data.

3. **Risk control options:** development of specific measures to reduce the identified risks (structural improvements, operational procedures, equipment requirements).

4. **Cost–benefit analysis:** evaluation of each risk control option using the *Cost of Averting a Fatality* (CAF) metric, defined as the net cost of the measure divided by the reduction in PLL. A measure is justified if its CAF is below the accepted threshold.

5. **Recommendations:** presentation of the analysis and the recommended risk control options to the IMO committee for consideration in rule-making.

The FSA framework embodies the ALARP principle (Section 7.2.1): measures within the ALARP region are implemented unless the CAF demonstrates that the cost is grossly disproportionate to the benefit (Kristiansen, 2005; Rausand, 2014).

7.5 Discussion

The transition from deterministic to probabilistic safety standards marks a major development in maritime safety engineering (Kristiansen, 2005). Guedes Soares and Santos (2015) demonstrate this transition through the damage stability framework (Section 7.3.1), where the deterministic approach—based on the survival of a fixed set of prescribed damage scenarios—has been replaced by the probabilistic attained subdivision index A, which integrates over all feasible damage scenarios weighted by their probability of occurrence.

The classical lost buoyancy method of Attwood (1917) provides the physical foundation that underlies both approaches: when a compartment is breached, the lost buoyancy causes bodily sinkage and, if asymmetric, heel. The modern probabilistic framework (derived in the *Ship Stability and Hydrostatics* chapter of the companion volume) generalises this deterministic calculation by weighting each damage scenario by its probability and evaluating the residual stability rather than merely the equilibrium condition.

The statistical analysis of accident data (Guedes Soares & Santos, 2015) reveals that accident frequencies have generally increased in the period 2000–2012 compared with 1990–2012, attributable to both increased traffic density and improved accident reporting practices. This finding has implications for the calibration of risk acceptance criteria and for the validation of probabilistic safety models.

The structural reliability framework of Decò et al. (2012) extends the probabilistic approach from damage stability to structural strength. The reliability index β (Equation 7.2) provides a mathematically rigorous measure of safety that integrates all relevant uncertainties into a single scalar. The time-variant decline in β due to corrosion (from 5.3 to 3.1 over 25 years) demonstrates that the margin of safety is not static: a vessel that comfortably exceeds target reliability at commissioning may approach critical thresholds within its design life. The redundancy indices RI_1 and RI_2 (Equations 7.3–7.4) complement β by measuring the structural system's tolerance to partial failure, providing an additional safety dimension that is not captured by conventional deterministic design (Decò et al., 2012).

The floodable-length methodology formalised by Biran (2003) provides the deterministic geometric basis underlying both prescriptive and probabilistic subdivision standards. By constructing the floodable-length curve for a given permeability and margin line, the naval architect identifies the longitudinal positions where subdivision is most critical; the factor of subdivision F then scales the floodable length to account for the ship type and service. Although the IMO now relies on the probabilistic attained index A (derived in the companion volume), the floodable-length concept remains necessary for the initial placement of watertight bulkheads and for understanding the physics of why certain damage locations are more dangerous than others.

The manoeuvrability review in Sutulo and Guedes Soares (2023) connects ship handling performance directly to safety outcomes. The IMO manoeuvring standards (MSC.137(76)) specify maximum advance, tactical diameter, and stopping distance as acceptance criteria for new vessels; meeting these criteria ensures that a ship can avoid collision through emergency manoeuvres or execute a Williamson turn for man-overboard recovery within a bounded sea area. The review demonstrates that overshoot angles in the zig-zag test and the steady turning radius are governed by the same hydrodynamic derivatives—Y'_r, N'_r, Y'_v, N'_v—that appear in the equations of motion developed in the *Classical Mechanics and Ship Motion* chapter of the companion volume, establishing a quantitative link between manoeuvring physics and collision-avoidance capability (Sutulo & Guedes Soares, 2023).

The engineering course notes of United States Naval Academy (2021) complement the theoretical damage stability framework with practical laboratory exercises. Students compute the damaged waterline for prescribed compartment flooding scenarios using both the lost buoyancy and added weight methods, compare the calculated heel and sinkage with model-test observations, and verify that the residual stability satisfies the applicable criteria. The USNA

programme also includes exercises on the Williamson turn—a specific turning manoeuvre designed to bring a vessel back to the reciprocal of its original track—reinforcing the connection between manoeuvring physics and the man-overboard recovery problem (United States Naval Academy, 2021).

The convergence of real-time sensor data with computational models is enabling the development of *digital twin* concepts for ship safety: a continuously updated virtual replica of the physical vessel that integrates structural monitoring, stability calculations, and environmental data to predict the vessel's safety state in real time (Molland, 2008). Such systems can alert the crew to developing hazards—progressive flooding, structural fatigue accumulation, or approaching stability limits—before they become critical. The challenge lies in the validation and certification of these predictive models against the physical phenomena described throughout this chapter: the lost buoyancy flooding mechanics of Attwood (1917), the structural reliability degradation quantified by Decò et al. (2012), and the probabilistic damage stability framework derived in the companion volume.

7.6 Conclusion

Maritime safety engineering rests on the quantification of risk as the product of accident frequency and consequence severity (Equation 7.1). Analysis of 10,841 serious casualty records over 602,998 ship-years reveals that Ro-Ro cargo ships and cruise ships have the highest accident frequencies, while passenger Ro-Ro vessels carry the highest potential loss of life (Guedes Soares & Santos, 2015). The probabilistic damage stability framework (derived in the *Ship Stability and Hydrostatics* chapter of the companion volume) supersedes the deterministic lost buoyancy and added weight methods—though these remain the physical foundation—by integrating over all feasible damage scenarios weighted by their probability of occurrence (Attwood, 1917; Guedes Soares & Santos, 2015; Rawson & Tupper, 2001). The floodable-length curve, formalised by Biran (2003), provides the geometric basis for watertight bulkhead placement by identifying the longitudinal positions where flooding is most critical.

The structural dimension of safety is captured by the reliability index $\beta = \Phi^{-1}(1 - P_f)$ (Equation 7.2), which integrates loading randomness, material variability, and modelling error into a single probabilistic measure. Time-variant analysis shows that corrosion-driven degradation reduces β from 5.3 at commissioning to 3.1 after 25 years, demonstrating that static safety factors cannot guarantee adequate safety over a vessel's lifetime (Decò et al., 2012). The redundancy indices RI_1 and RI_2 (Equations 7.3–7.4) complement β by measuring tolerance to partial component failure. Human factor analysis using TRACEr-MAR reveals that collision errors are overwhelmingly in the execution domain (99%), while grounding errors divide between supervision (35%) and situation assessment (23%), establishing the link

between cognitive failures and the physical consequences of collision kinetic energy—amplified 10–40% by hydrodynamic added mass—and bottom raking structural response (Guedes Soares & Santos, 2015; Rawson & Tupper, 2001). Ship manoeuvrability standards (advance, tactical diameter, stopping distance) translate the hydrodynamic derivatives of the equations of motion into quantitative collision-avoidance and man-overboard recovery criteria (Sutulo & Guedes Soares, 2023; United States Naval Academy, 2021).

References

Attwood, E. L. (1917). *A text-book of theoretical naval architecture* (7th ed.) [First published 1899; seventh edition revised 1916, reprinted 1917]. Longmans, Green; Co.

Biran, A. B. (2003). *Ship hydrostatics and stability*. Butterworth-Heinemann.

Decò, A., Frangopol, D. M., & Zhu, B. (2012). Reliability and redundancy assessment of ships under different operational conditions. *Engineering Structures*, *42*, 457–471. https://doi.org/10.1016/j.engstruct.2012.04.017

Fischer-Cripps, A. C. (2014). *The physics companion* (2nd ed.). CRC Press. https://doi.org/10.1201/b17356

Guedes Soares, C., & Santos, T. A. (Eds.). (2015). *Maritime technology and engineering: Proceedings of MARTECH 2014*. CRC Press.

Hughes, O. F., & Paik, J. K. (2010). *Ship structural analysis and design*. The Society of Naval Architects; Marine Engineers.

Kristiansen, S. (2005). *Maritime transportation: Safety management and risk analysis*. Elsevier Butterworth-Heinemann. https://doi.org/10.4324/9780080473369

Molland, A. F. (Ed.). (2008). *The maritime engineering reference book: A guide to ship design, construction and operation*. Butterworth-Heinemann. https://doi.org/10.1016/B978-0-7506-8987-8.X0001-7

Rausand, M. (2014). *Reliability of safety-critical systems: Theory and applications*. John Wiley & Sons. https://doi.org/10.1002/9781118776353

Rawson, K. J., & Tupper, E. C. (2001). *Basic ship theory* (5th ed.). Butterworth-Heinemann.

Sutulo, S., & Guedes Soares, C. (2023). Ship dynamics and hydrodynamics. *Journal of Marine Science and Engineering*, *11*(5), 911. https://doi.org/10.3390/jmse11050911

United States Naval Academy. (2021). En400: Principles of ship performance [Course notes, Fall AY2021].

Chapter 8

Environmental Physics in Maritime Operations

8.1 Introduction

Environmental physics in the maritime context encompasses the physical processes that govern the interaction between shipping activities and the marine environment (Clark, 2001). These include the dispersion of atmospheric emissions, the fate of oil spills, the propagation of underwater noise from ships, and the optical and acoustic effects of suspended particles in seawater. Understanding these processes requires the thermodynamic, optical, and acoustic principles established in the preceding chapters.

Dera (1992) provided essential background on the physical properties of suspended particles in seawater and their influence on the optical environment, which is directly relevant to environmental monitoring and the assessment of water quality.

8.2 Scientific Background

8.2.1 Combustion Chemistry and Emission Formation

The combustion of marine fuels—primarily heavy fuel oil (HFO) and marine diesel oil (MDO)—generates a mixture of gaseous and particulate emissions (Molland, 2008). The dominant species by mass is carbon dioxide (CO_2), with smaller but environmentally significant quantities of nitrogen oxides (NO_x), sulphur oxides (SO_x), carbon monoxide (CO), and particulate matter (PM).

Guedes Soares and Santos (2015) present a bottom-up emission estimation method in which the total emission from a voyage is calculated as the sum of contributions from each engine type, fuel type, and voyage phase:

Equation 16.2 — Trip emission estimation:

$$E_{\text{trip}} = \sum_{j,m,p} \left(EF_{i,j,m} \times FC_{j,m,p} \right) \tag{8.1}$$

where E_{trip} is the emission of pollutant i over a complete trip (tonnes), $EF_{i,j,m}$ is the emission factor for pollutant i with engine type j and fuel type m (kg/tonne of fuel), $FC_{j,m,p}$ is the fuel consumption in phase p of the voyage (tonnes), and the summation runs over engine types j (slow-, medium-, high-speed diesel, gas turbine, steam turbine), fuel types m (HFO, MDO/MGO), and voyage phases p (cruising, manoeuvring, hotelling) (Guedes Soares & Santos, 2015).

Representative emission factors for HFO-fuelled main engines are: CO_2 = 3179 kg/tonne, NO_x = 87.1 kg/tonne, SO_x = 46 kg/tonne, PM = 6.7 kg/tonne, and CO = 2.5 kg/tonne (Guedes Soares & Santos, 2015). The CO_2 factor reflects the carbon content of the fuel (≈87% for HFO) and the stoichiometry of the oxidation reaction $C + O_2 \rightarrow CO_2$.

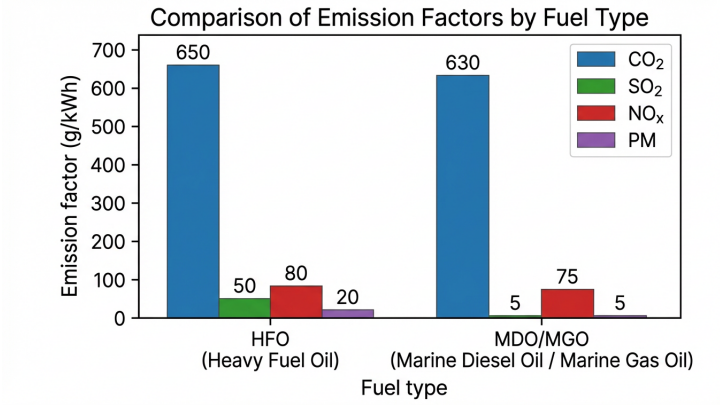

Figure 8.1: Representative emission factors for heavy fuel oil (HFO) and marine diesel/gas oil (MDO/MGO) main engines. CO_2 dominates by mass (>3100 kg/tonne fuel), reflecting the carbon content of the fuel and the stoichiometry of combustion. HFO produces substantially higher SO_x and PM emissions than MDO/MGO due to its higher sulphur and ash content (Guedes Soares & Santos, 2015).

The emission factors presented above apply to conventional petroleum fuels. Regulatory limits on sulphur content have been steadily tightened: the global sulphur cap was reduced from 3.50% to 0.50% m/m effective 1 January 2020, while in designated Emission Control Areas (ECAs) the limit is 0.10% (Guedes Soares & Santos, 2015; Molland, 2008). Compliance is achieved either by burning low-sulphur fuel (MDO/MGO) or by using exhaust gas cleaning systems (Section 8.4.1) with higher-sulphur fuels. For NO_x, the IMO Tier III standard applicable in ECAs requires an approximately 80% reduction from the Tier I baseline, typically achieved through selective catalytic reduction (SCR) or exhaust gas recirculation (EGR) (Molland, 2008).

Alternative fuels—liquefied natural gas (LNG), methanol, and ammonia—are increasingly adopted to meet these tightening emission standards. LNG (predominantly methane, CH_4) has a lower carbon-to-hydrogen ratio than

HFO, reducing CO_2 emissions per unit energy by approximately 20–25%; it also produces negligible SO_x and substantially reduced NO_x and PM (Molland, 2008). However, a complete *well-to-wake* assessment must include upstream emissions from fuel extraction, processing, and transport, as well as any unburnt methane released to the atmosphere (*methane slip*), since methane has a global warming potential approximately 28–34 times that of CO_2 over a 100-year horizon (Guedes Soares & Santos, 2015).

8.2.2 Atmospheric Dispersion of Pollutants

When pollutants are released from a ship's exhaust stack, they are transported and diluted by the ambient wind field as they disperse through the atmospheric boundary layer. The concentration field downwind of a continuous point source in a steady wind can be described by the Gaussian plume model, in which the cross-wind and vertical concentration profiles follow Gaussian distributions (Clark, 2001). The plume centreline rises initially above the physical stack height due to the buoyancy of the hot exhaust gases and the momentum of the discharge; the resulting *effective stack height* determines the initial elevation of the concentration maximum.

The rate of plume dispersion depends on the atmospheric stability: in unstable conditions (strong surface heating, convective mixing) the plume disperses rapidly and ground-level concentrations are low; in stable conditions (temperature inversions, calm winds) the plume remains concentrated and can produce elevated pollutant levels at the surface (Wallace & Hobbs, 2006). In port areas, the combination of low effective stack heights (ship funnels are lower than land-based industrial stacks), proximity to populated areas, and the concentration of many vessels in a confined waterway can produce localised SO_x, NO_x, and PM concentrations that exceed ambient air quality standards (Guedes Soares & Santos, 2015). The emission estimation framework of Equation 8.1 provides the source term for such dispersion calculations.

8.2.3 Suspended Particles in Seawater

Seawater contains significant quantities of suspended particulate matter of both organic (biological) and inorganic (mineralogical) origin. Dera (1992) reported mass concentrations ranging from $0.2\,\mathrm{mg\,dm^{-3}}$ in open ocean waters to over $18\,\mathrm{mg\,dm^{-3}}$ in coastal zones, with organic matter constituting 14–62% of the total depending on location.

The size distribution of suspended particles in seawater is well described by the Junge (hyperbolic) distribution (Dera, 1992, Eq. 2.7.2):

Equation 16.1 — Junge particle size distribution:

$$N_c(D) = k\,D^{-m} \tag{8.2}$$

where $N_c(D)$ is the cumulative number concentration of particles with diameter greater than D, k is the numerical concentration coefficient, and m is

the slope coefficient. For the Baltic Sea, typical values are $m \approx 2.8$ and $k \approx 2 \times 10^6$ for particle diameters $D > 7\,\mu\text{m}$, and $m \approx 4$ and $k \approx 6 \times 10^6$ for $D < 7\,\mu\text{m}$ (Dera, 1992). The concentration coefficient k varies by orders of magnitude (10^4–10^8) between locations and seasons, while the slope coefficient m is comparatively stable.

This particle population has direct environmental significance: it controls the optical clarity of the water column (Chapter 2) by contributing to both absorption and scattering, thereby determining the depth of the euphotic zone and the productivity of the marine ecosystem. Anthropogenic additions to the particulate load—from dredging, ballast water discharge, or land-based runoff—alter the natural particle size distribution and can degrade water quality (Clark, 2001).

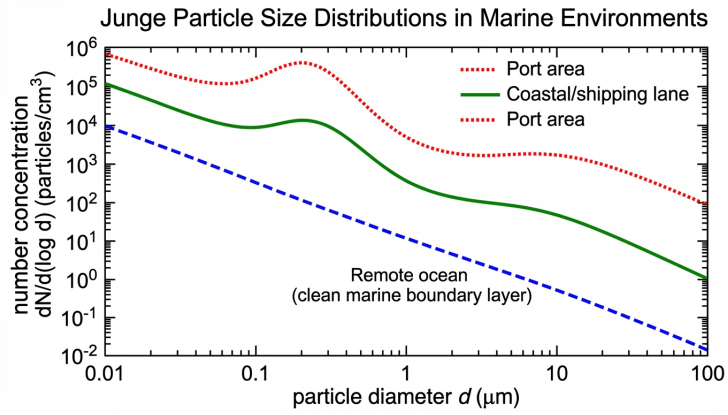

Figure 8.2: Junge (hyperbolic) particle size distributions $N_c(D) = k\,D^{-m}$ (Equation 8.2) for three representative marine environments. The concentration coefficient k spans orders of magnitude from open ocean to turbid harbour waters, while the slope coefficient m remains comparatively stable ($\sim$2.8–4.0). The particle population controls the optical properties of the water column and the depth of the euphotic zone (Dera, 1992).

8.2.4 Oil Spill Physics

When oil is released to the sea surface, it undergoes a sequence of physical and chemical *weathering* processes that determine its fate (Clark, 2001).

Spreading. The oil spreads under the influence of gravity, inertia, viscous, and surface tension forces. The initial gravity–inertia phase produces rapid radial spreading proportional to $t^{1/4}$ (Fay's scaling), transitioning to the gravity–viscous regime ($\propto t^{1/6}$) and ultimately to the surface-tension–viscous regime as the slick thins (Clark, 2001). A 1000 t spill of crude oil may spread to an area exceeding $10\,\text{km}^2$ within the first 24 hours.

Evaporation. The lighter hydrocarbon fractions (C_5–C_{12}) evaporate from the slick surface. The evaporation rate depends on the vapour pressure of the oil fractions, the wind speed, and the slick surface area. For light crude oils, 20–40% of the volume may evaporate within the first few days; for heavy fuel oils the fraction is typically less than 10% (Clark, 2001).

Dispersion and emulsification. Wave action breaks the slick into small droplets that are entrained in the water column (*natural dispersion*). Simultaneously, seawater penetrates the oil, forming a water-in-oil emulsion (*chocolate mousse*) that is more viscous and persistent than the original oil. Emulsification increases the apparent volume of the pollutant by a factor of 3–4 and greatly complicates cleanup (Clark, 2001).

Dissolution and biodegradation. The water-soluble fractions (low-molecular-weight aromatics) dissolve into the water column, contributing to toxicity. Natural microbial populations can degrade hydrocarbons through aerobic oxidation, but the rate depends on nutrient availability, temperature, and oxygen supply. Complete biodegradation of a major spill takes months to decades (Clark, 2001).

8.3 Theoretical Framework

8.3.1 Ship Energy Efficiency

The block coefficient C_B is a fundamental hull form parameter that influences both ship resistance (see the *Fluid Dynamics and Ship Resistance* chapter of the companion volume) and the energy efficiency of the vessel. Guedes Soares and Santos (2015) employ the Katsoulis formula to relate the block coefficient to the principal dimensions and service speed:

Equation 16.3 — Block coefficient (Katsoulis):

$$C_B = k \cdot f \cdot L^{\,a} \cdot B^{\,b} \cdot T^{\,c} \cdot V^{d} \tag{8.3}$$

where L is the length between perpendiculars, B the beam, T the draught, V the service speed, and k, f, a, b, c, d are empirically determined coefficients (Guedes Soares & Santos, 2015). For the three bulk carriers studied (35,364–66,533 DWT), the resulting block coefficients ranged from 0.76 to 0.82, confirming full hull forms typical of cargo vessels.

Because the emission from a voyage is directly proportional to fuel consumption (Equation 8.1), which in turn depends on the resistance and propulsive efficiency of the hull, the block coefficient provides a useful early-stage predictor of emissions (Papanikolaou, 2014). Guedes Soares and Santos (2015) derived second-order polynomial regression formulas relating annual emissions of each pollutant to C_B, enabling emission estimation even during the pre-design stage.

The IMO's regulatory framework for ship energy efficiency employs three complementary indices (Papanikolaou, 2014). The *Energy Efficiency Design*

Index (EEDI) applies to new ships and quantifies the CO_2 emitted per unit of transport work:

$$\text{EEDI} = \frac{\text{CO}_2 \text{ emission } [\text{g}]}{\text{deadweight} \times \text{speed } [\text{tonne} \cdot \text{nm}]} \tag{8.4}$$

The numerator accounts for the main and auxiliary engine power, the specific fuel consumption, and the fuel carbon factor, while the denominator uses the deadweight and the design speed as proxies for transport capacity (Papanikolaou, 2014). The required EEDI is ship-type-dependent and tightens in phases: Phase 1 required a 10% improvement over the 2013 baseline, with subsequent phases requiring 20–30% reductions.

The *Energy Efficiency Existing Ship Index* (EEXI) extends the EEDI concept to existing ships, requiring them to demonstrate compliance with an attained index calculated from the installed engine power and specific fuel consumption at a reduced reference speed. Ships whose EEXI exceeds the required value must implement technical measures such as engine power limitation, waste heat recovery, or hull and propeller optimisation (Papanikolaou, 2014).

The *Carbon Intensity Indicator* (CII) is an operational metric that rates each ship annually based on its actual fuel consumption and distance travelled. The rating scale (A–E) tightens each year, creating a continuous incentive for operational efficiency improvement. Measures that improve CII include slow steaming, weather routing, hull cleaning, and optimal trim (Guedes Soares & Santos, 2015). The underlying thermodynamic analysis of engine cycle efficiency is developed in the *Thermodynamics in Marine Engineering* chapter of the companion volume.

8.3.2 Greenhouse Gas Emissions and Carbon Accounting

The environmental impact of ship emissions is quantified through Life Cycle Assessment (LCA), a standardised methodology under ISO 14040. Guedes Soares and Santos (2015) apply this framework to the hull subsystem of an oil tanker over a 25-year life cycle, considering four stages: shipbuilding, operation, maintenance, and dismantling.

The Life Cycle Impact Assessment (LCIA) converts the emission inventory into environmental impact scores using characterisation factors. The impact score for impact category c is (Guedes Soares & Santos, 2015):

Equation 16.4 — Life cycle impact score:

$$IS_c = \sum_{x=1}^{n} CF_{x,c} \times m_x \tag{8.5}$$

where $CF_{x,c}$ is the characterisation factor of emission substance x within impact category c (for example, CO_2 equivalents for climate change), and m_x is the mass of substance x emitted as recorded in the inventory (Guedes Soares

& Santos, 2015). The nine emission species covered include CO_2, CO, SO_2, SO_x, NO_x, PM, CH_4, volatile organic compounds (VOC), and non-methane VOC.

At the damage category level, the impact scores are aggregated into three areas of protection—human health, ecosystem health, and resource availability—providing a comprehensive view of the environmental cost of the vessel across its complete life cycle (Guedes Soares & Santos, 2015).

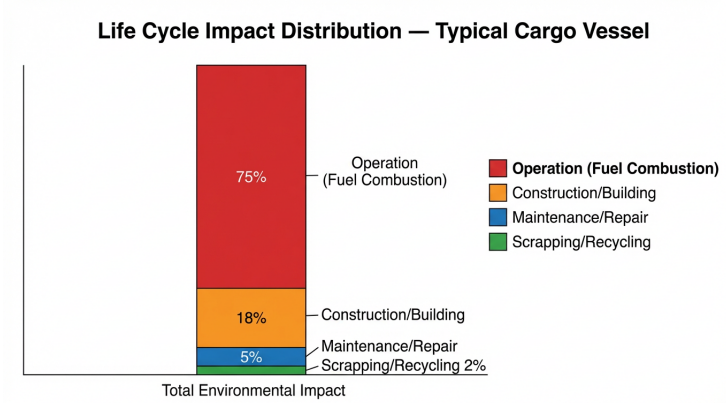

Figure 8.3: Distribution of life cycle environmental impact across the four stages of an oil tanker hull (25-year service life). The operational phase dominates all impact categories, contributing >94% of CO_2 equivalent, >96% of NO_x, and >97% of SO_x emissions (Equation 8.5). Shipbuilding, maintenance, and dismantling together account for less than 6% of the total life cycle impact (Guedes Soares & Santos, 2015).

The IMO's initial strategy on the reduction of greenhouse gas emissions from ships sets targets of at least 40% reduction in CO_2 emissions per transport work by 2030 (relative to 2008) and a 50% reduction in total annual GHG emissions by 2050 (Guedes Soares & Santos, 2015). Achieving these targets requires a combination of energy efficiency improvements (Section 8.3.1), the adoption of low- and zero-carbon fuels (Section 8.4.2), and operational measures.

The *well-to-wake* carbon accounting framework extends the tank-to-wake emissions quantified by the trip emission formula (Equation 8.1) to include the upstream (*well-to-tank*) emissions from fuel production, processing, and transport. For conventional fuels, the well-to-tank emissions are approximately 10–20% of the total; for alternative fuels, this fraction can be much larger due to the energy-intensive production processes (e.g. electrolysis for hydrogen, Haber–Bosch synthesis for ammonia) (Guedes Soares & Santos, 2015). A fuel that appears zero-carbon on a tank-to-wake basis may have substantial well-to-tank emissions if the production energy is derived from fossil sources.

8.3.3 Ballast Water Treatment Physics

Ballast water taken on in one biogeographic region and discharged in another can transfer invasive aquatic species—bacteria, algae, larvae, and small organisms—with potentially severe ecological consequences (Clark, 2001). The IMO Ballast Water Management Convention (D-2 standard) requires that discharged ballast water contain no more than 10 viable organisms per cubic metre for organisms $\geq$ 50 µm in minimum dimension, and no more than 10 per millilitre for organisms in the 10–50 µm range.

Treatment systems exploit several physical mechanisms. *UV irradiation* systems expose the ballast water to ultraviolet radiation at a wavelength of approximately 254 nm (the germicidal peak), where the photon energy ($E = hc/\lambda \approx 4.9$ eV) is sufficient to damage the DNA of microorganisms, preventing replication; for a concise treatment, see (Fischer-Cripps, 2014). The required dose depends on the target organism; typical treatment systems deliver 40–100 mJ cm^{-2} (Dera, 1992). The UV transmittance of the water—a function of the dissolved and particulate matter (Section 8.2.3)—determines the penetration depth and thus the reactor design.

Electrochlorination systems generate sodium hypochlorite by electrolysis of the seawater itself, exploiting the chloride ion content (~ 19 g L^{-1}) as a feedstock. The generated active chlorine (5–15 mg L^{-1}) oxidises and destroys microorganisms. A subsequent neutralisation step reduces the residual chlorine to below 0.1 mg L^{-1} before discharge (Clark, 2001).

Filtration systems (typically 40–50 µm mesh) physically remove the larger organisms and sediment from the ballast water before secondary treatment. The combination of filtration with UV or electrochlorination achieves the D-2 standard across a range of source water qualities (Clark, 2001).

8.3.4 Underwater Noise and Marine Ecosystem Impact

The underwater radiated noise (URN) of ships and its impact on marine ecosystems constitute a growing environmental concern that links the acoustic physics of Chapter 6 to the environmental regulatory framework of this chapter.

Ship noise is dominated by propeller cavitation, machinery vibration, and hydrodynamic flow noise, with typical broadband source levels of 170–190 dB re 1 µPa at 1 m (Urick, 1983). The cumulative effect of global shipping raises ambient noise levels in the 10–500 Hz band by 10–15 dB above natural levels, masking the communication signals of baleen whales and other marine mammals (Medwin & Clay, 1998; Urick, 1983).

The *Sound Exposure Level* (SEL) integrates the received sound pressure squared over the duration of the exposure, providing a cumulative dose metric relevant to physiological harm:

$$\mathrm{SEL} = 10\log_{10}\left(\int_0^{T} p^2(t)\,\mathrm{d}t\right) - 10\log_{10}(p_{\mathrm{ref}}^2 \cdot t_{\mathrm{ref}}) \tag{8.6}$$

where $p(t)$ is the instantaneous sound pressure, T is the exposure duration, $p_{\text{ref}} = 1\,\mu\text{Pa}$, and $t_{\text{ref}} = 1\,\text{s}$ (Medwin & Clay, 1998). Fish and invertebrates can experience behavioural changes (avoidance, altered feeding) at lower SEL thresholds than mammals, but the evidence base for sublethal effects remains incomplete (Clark, 2001).

Mitigation strategies include propeller design modifications to delay cavitation inception, vibration isolation of main engines, hull fairing, and operational measures such as speed reduction in ecologically sensitive areas—the dominant effect, since radiated noise scales approximately as V^5–V^6 with ship speed (Urick, 1983).

8.4 Applications in Maritime Systems

8.4.1 Exhaust Gas Cleaning Systems (Scrubbers)

Exhaust gas cleaning systems (*scrubbers*) enable ships burning high-sulphur fuel oil to meet the SO_x emission limits by removing sulphur oxides from the exhaust stream before discharge to the atmosphere (Molland, 2008).

In an *open-loop* scrubber, seawater—which is naturally alkaline (pH ≈ 8.1)—is sprayed through the exhaust gas in a packed-bed or spray tower. The SO_x dissolves and reacts with the seawater alkalinity, forming sulphate ions that are discharged overboard with the washwater. The chemical process is essentially an acid–base neutralisation: $\text{SO}_2 + \text{H}_2\text{O} + \tfrac{1}{2}\text{O}_2 \rightarrow \text{H}_2\text{SO}_4$, with the sulphuric acid immediately neutralised by the bicarbonate and carbonate ions in seawater. Open-loop systems achieve SO_x removal efficiencies exceeding 95% but produce large volumes of acidified washwater, raising concerns about local water quality in enclosed port areas (Molland, 2008).

In a *closed-loop* system, a recirculating alkaline solution (typically NaOH-dosed freshwater) absorbs the SO_x and is periodically cleaned and replenished. The spent sludge is stored on board for shore disposal. Closed-loop systems avoid seawater discharge but require chemical reagent supply and sludge handling.

Hybrid scrubbers can operate in either mode, switching between open-loop at sea and closed-loop in restricted waters. All configurations must also address the co-removal of particulate matter and polycyclic aromatic hydrocarbons entrained in the exhaust (Molland, 2008).

8.4.2 Alternative Fuels and Energy Sources

The transition from conventional petroleum fuels to low- and zero-carbon alternatives involves fundamental changes in fuel properties, storage, and combustion characteristics (Molland, 2008).

Liquefied Natural Gas (LNG). Methane (CH_4) is stored at $-162\,^\circ\text{C}$ and atmospheric pressure in cryogenic tanks, with a volumetric energy density

approximately 40% lower than that of HFO. Combustion produces approximately 20–25% less CO_2 per unit energy than HFO, negligible SO_x, and significantly reduced NO_x and PM due to the gaseous premixed flame. *Methane slip*—unburnt methane released through the exhaust—remains a concern because of methane's high global warming potential (Guedes Soares & Santos, 2015; Molland, 2008).

Methanol and ammonia. Methanol (CH_3OH) is a liquid at ambient conditions, simplifying storage and handling compared to LNG. It contains no sulphur and produces lower PM emissions than HFO. Ammonia (NH_3) is a zero-carbon fuel at the point of combustion but is toxic (occupational exposure limit 25 ppm), requiring stringent safety measures (Kristiansen, 2005). Both fuels have lower volumetric energy densities than HFO, requiring larger fuel tanks for equivalent range.

Wind-assisted propulsion. Rotor sails (Flettner rotors), rigid wing sails, and kite systems harness wind energy to supplement mechanical propulsion, reducing fuel consumption by an estimated 5–30% depending on the route and wind conditions (Molland, 2008). The aerodynamic lift force on a spinning Flettner rotor exploits the Magnus effect: the circulation induced by the rotating cylinder produces a force perpendicular to the apparent wind, propelling the vessel forward.

The fuel cell converts the chemical energy of a fuel (hydrogen, methanol, or ammonia) directly into electrical energy through electrochemical reactions, bypassing the Carnot limitation of heat engines. Proton exchange membrane (PEM) fuel cells operating on hydrogen achieve electrical efficiencies of 50–60%, approximately double the efficiency of a typical marine diesel engine (Molland, 2008). The thermodynamic analysis of these conversion processes is developed in the *Thermodynamics in Marine Engineering* chapter of the companion volume.

8.4.3 Oil Spill Response Physics

When an oil spill occurs, the response strategy must match the physical state and behaviour of the oil, which evolves through the weathering processes described in Section 8.2.4.

Mechanical containment. *Booms* are floating barriers deployed around the slick to prevent lateral spreading. The boom must extend sufficiently above (freeboard) and below (skirt depth) the water surface to contain the oil under the action of wind, waves, and current. In currents exceeding approximately $0.35\ \mathrm{m\,s^{-1}}$ (~ 0.7 knot), oil entrainment beneath the boom skirt causes failure of containment (Clark, 2001). *Skimmers* remove the contained oil from the water surface by adhesion (oleophilic drum or disc), suction, or weir overflow.

Chemical dispersants. Dispersants are surfactants that reduce the oil–water interfacial tension, enabling wave energy to break the slick into small droplets (10–$100\ \mu$m) that disperse naturally in the water column, greatly in-

creasing the surface area available for biodegradation (Clark, 2001). The effectiveness depends on the oil viscosity, sea state, and temperature; dispersants are less effective on weathered, emulsified oil.

In-situ burning. Controlled ignition of the oil slick can remove large volumes rapidly (evaporation rates of 1–$3\,\mathrm{mm\,min^{-1}}$ of slick thickness), but requires a minimum slick thickness (> 2–3 mm), calm seas, and fire-resistant booms to concentrate the oil. The smoke plume contains particulate matter and combustion products that must be factored into the environmental trade-off (Clark, 2001).

Bioremediation. The application of nutrients (nitrogen, phosphorus) to stimulate natural microbial hydrocarbon degradation accelerates the ultimate breakdown of the oil, particularly the aromatic fractions that are most persistent and toxic (Clark, 2001).

8.4.4 Antifouling and Hull Coatings

Marine biofouling—the colonisation of the ship's underwater hull by algae, barnacles, tubeworms, and other organisms—increases the hull surface roughness and hence the frictional resistance. A heavily fouled hull can experience a resistance increase of 30–40% relative to a freshly painted surface, with a corresponding increase in fuel consumption and emissions (Molland, 2008).

The physics of fouling attachment involves a sequence of stages: (1) adsorption of organic molecules to form a conditioning film within minutes of immersion; (2) colonisation by bacteria and diatoms forming a *biofilm* (*microfouling*) within days; (3) settlement of macrofouling organisms (barnacles, mussels, algae) within weeks. The rate and severity of fouling depend on the sea surface temperature, salinity, light availability, and the time a vessel spends in port relative to time at sea (Clark, 2001).

Antifouling coatings prevent or inhibit fouling settlement. *Biocidal coatings* release a toxic compound (typically copper-based, after the global ban on tributyltin, TBT) at a controlled rate by ablation of the paint matrix; the ablation also provides a self-polishing effect that maintains a smooth surface (Clark, 2001). *Fouling-release coatings* use low-surface-energy polymers (e.g. silicone elastomers) that form a surface to which organisms adhere weakly and are removed by the hydrodynamic shear forces at the hull boundary layer when the vessel is underway (Molland, 2008). The frictional resistance penalty from fouling is analysed quantitatively in the *Fluid Dynamics and Ship Resistance* chapter of the companion volume.

8.4.5 Waste Heat Recovery

Waste heat recovery (WHR) systems capture a portion of the thermal energy rejected in the engine exhaust gases and jacket cooling water, converting it to

useful work or electrical power. The exhaust gas temperature of a large two-stroke marine diesel engine at the turbocharger outlet is typically $240–300\,^{\circ}\text{C}$, representing approximately 25% of the fuel input energy (Woodyard, 2009).

The most common WHR arrangement uses an *exhaust gas economiser* (waste heat boiler) to generate steam, which drives a steam turbine connected to a generator. In more advanced combined-cycle configurations, a supplementary power turbine on the turbocharger shaft also generates electricity. The combined thermal efficiency of the diesel-WHR system can reach 52–55%, compared to 48–50% for the diesel engine alone (Woodyard, 2009).

The thermodynamic analysis of the Rankine steam cycle and the available exergy in the exhaust stream is developed in the *Thermodynamics in Marine Engineering* chapter of the companion volume. From the environmental perspective, WHR reduces the specific fuel consumption per unit of total power output, directly lowering CO_2, NO_x, SO_x, and PM emissions without requiring any change to the fuel type. For a typical large container ship, WHR can reduce annual CO_2 emissions by approximately 4–8% (Guedes Soares & Santos, 2015; Woodyard, 2009).

8.5 Discussion

The environmental physics of the ocean is governed by the same fundamental properties—density, optical absorption/scattering, and acoustic propagation—that determine the behaviour of seawater as a physical medium. The Junge particle size distribution (Equation 8.2) connects the particulate environment to the optical clarity of the water column (Chapter 10): increased particle loading raises the attenuation coefficient $c = a + b$, reduces the depth of the euphotic zone, and alters the spectral composition of underwater light (Dera, 1992). Similarly, underwater noise from shipping (Chapter 14) must be assessed in the context of the acoustic propagation environment created by the temperature, salinity, and pressure profiles discussed in Chapters 8 and 12 (Clark, 2001).

The emission estimation framework of Guedes Soares and Santos (2015) demonstrates two complementary approaches: the bottom-up trip emission calculation (Equation 8.1), which quantifies operational emissions from fuel consumption data, and the life cycle impact assessment (Equation 8.5), which extends the analysis across the full cradle-to-grave life cycle of the vessel. The regression-based approach linking emissions to block coefficient C_B (Equation 8.3) connects hull form design to environmental performance, enabling emissions to be considered as early as the pre-design stage.

The trajectory toward decarbonisation of international shipping requires a portfolio approach: no single technology or fuel can deliver the $\geq$50% GHG reduction target by 2050 (Guedes Soares & Santos, 2015). The energy efficiency regulatory instruments (EEDI, EEXI, CII; Section 8.3.1) address the design and operational dimensions, while the alternative fuels and WHR technologies of

Sections 8.4.2 and 8.4.5 address the fuel carbon intensity. The life cycle impact assessment framework (Equation 8.5) provides the analytical tool for comparing these options on a consistent well-to-wake basis.

The environmental trade-offs are complex: scrubbers (Section 8.4.1) solve the air quality problem but transfer pollutants to the water; LNG eliminates SO_x but introduces methane slip risk; antifouling coatings (Section 8.4.4) reduce resistance and emissions but may release biocides to the marine environment. The optimization of these trade-offs requires the quantitative physics-based analysis developed throughout this chapter, underpinned by the fundamental oceanographic properties—optical, acoustic, and thermodynamic—of the marine environment (Clark, 2001; Dera, 1992; Guedes Soares & Santos, 2015).

8.6 Conclusion

The environmental physics of maritime operations links the fundamental properties of seawater—density, optical absorption and scattering, acoustic propagation—to the assessment of anthropogenic impacts. Suspended particles in seawater follow the Junge distribution $N_c(D) = k\,D^{-m}$ (Equation 8.2), with the concentration coefficient k spanning orders of magnitude between open ocean ($\sim 10^4$) and coastal/harbour waters ($\sim 10^7$–10^8) (Dera, 1992). This particle population governs the optical clarity of the water column: anthropogenic inputs from dredging, ballast water discharge, and land-based runoff alter the natural size distribution, raising the attenuation coefficient and reducing the euphotic zone depth with direct consequences for ecosystem productivity (Clark, 2001). The bottom-up trip emission framework (Equation 8.1) quantifies operational emissions from fuel consumption and engine-specific emission factors, while the life cycle impact assessment (Equation 8.5) extends the analysis across the vessel's full cradle-to-grave trajectory, with the operational phase dominating all impact categories at $>$94% of the total (Guedes Soares & Santos, 2015). The regression-based link between hull block coefficient C_B (Equation 8.3) and annual emissions enables environmental performance to be considered as early as the pre-design stage, bridging hull form hydrodynamics (see the *Fluid Dynamics and Ship Resistance* chapter of the companion volume) and environmental regulation (Guedes Soares & Santos, 2015; Papanikolaou, 2014).

References

Clark, R. B. (2001). *Marine pollution* (5th ed.). Oxford University Press. https://doi.org/10.1016/S0025-326X(01)00138-2

Dera, J. (1992). *Marine physics* (P. Senn, Trans.) [Translated from Polish. Original: *Fizyka morza*, 1983]. Elsevier.

Fischer-Cripps, A. C. (2014). *The physics companion* (2nd ed.). CRC Press. https://doi.org/10.1201/b17356

Guedes Soares, C., & Santos, T. A. (Eds.). (2015). *Maritime technology and engineering: Proceedings of MARTECH 2014*. CRC Press.

Kristiansen, S. (2005). *Maritime transportation: Safety management and risk analysis*. Elsevier Butterworth-Heinemann. https://doi.org/10.4324/9780080473369

Medwin, H., & Clay, C. S. (1998). *Fundamentals of acoustical oceanography*. Academic Press.

Molland, A. F. (Ed.). (2008). *The maritime engineering reference book: A guide to ship design, construction and operation*. Butterworth-Heinemann. https://doi.org/10.1016/B978-0-7506-8987-8.X0001-7

Papanikolaou, A. (2014). *Ship design: Methodologies of preliminary design*. Springer. https://doi.org/10.1007/978-94-017-8751-2

Urick, R. J. (1983). *Principles of underwater sound* (3rd ed.). McGraw-Hill.

Wallace, J. M., & Hobbs, P. V. (2006). *Atmospheric science: An introductory survey* (2nd ed.). Academic Press.

Woodyard, D. (2009). *Pounder's marine diesel engines and gas turbines* (9th ed.). Butterworth-Heinemann.

List of Abbreviations

Abbreviation	Definition
AAF	Amplitude Amplification Factor
ADCP	Acoustic Doppler Current Profiler
AIS	Automatic Identification System
ALARP	As Low As Reasonably Practicable
ARPA	Automatic Radar Plotting Aid
AUV	Autonomous Underwater Vehicle
BVP	Boundary-Value Problem
CAF	Cost of Averting a Fatality
CFD	Computational Fluid Dynamics
CII	Carbon Intensity Indicator
COLREGs	International Regulations for Preventing Collisions at Sea
CPA	Closest Point of Approach
CTD	Conductivity–Temperature–Depth (oceanographic profiler)
DALR	Dry Adiabatic Lapse Rate
DOP	Dilution of Precision
DSL	Deep Scattering Layer
ECA	Emission Control Area
ECDIS	Electronic Chart Display and Information System
EEDI	Energy Efficiency Design Index
EEXI	Energy Efficiency Existing Ship Index
EGNOS	European Geostationary Navigation Overlay Service
EGR	Exhaust Gas Recirculation
ELR	Environmental Lapse Rate
ENC	Electronic Navigational Chart
EOS	Equation of State (of Seawater)
ETA	Event Tree Analysis
FLS	Forward-Looking Sonar
FOG	Fibre Optic Gyroscope
FORM	First-Order Reliability Method

Abbreviation	Definition
FSA	Formal Safety Assessment
FTA	Fault Tree Analysis
GBS	Goal-Based Standards
GNSS	Global Navigation Satellite System
GPS	Global Positioning System
HF	High Frequency
HFO	Heavy Fuel Oil
IACS	International Association of Classification Societies
IMO	International Maritime Organization
INS	Inertial Navigation System
ITCZ	Intertropical Convergence Zone
JONSWAP	Joint North Sea Wave Project
LAT	Lowest Astronomical Tide
LCA	Life Cycle Assessment
LCIA	Life Cycle Impact Assessment
LEL	Lower Explosive Limit
LNG	Liquefied Natural Gas
LOC	Limiting Oxygen Concentration
LRIT	Long Range Identification and Tracking
MBES	Multi-Beam Echo Sounder
MDO	Marine Diesel Oil
MF	Medium Frequency
MGO	Marine Gas Oil
MMSI	Maritime Mobile Service Identity
NLSE	Nonlinear Schrödinger Equation
NO_x	Nitrogen Oxides
P–I	Pressure–Impulse (interaction diagram)
PEM	Proton Exchange Membrane
PLL	Potential Loss of Life
PM	Particulate Matter; also Pierson–Moskowitz (spectrum)
PSS	Practical Salinity Scale
QRA	Quantitative Risk Assessment
RCS	Radar Cross Section
RLG	Ring Laser Gyroscope
ROV	Remotely Operated Vehicle
RTK	Real-Time Kinematic (positioning)
SALR	Saturated Adiabatic Lapse Rate
SBAS	Satellite-Based Augmentation System
SBES	Single-Beam Echo Sounder
SCF	Stress Concentration Factor
SCR	Selective Catalytic Reduction
SHM	Simple Harmonic Motion
SO_x	Sulphur Oxides

Abbreviation	Definition
SOFAR	Sound Fixing and Ranging
SOLAS	Safety of Life at Sea
SOTDMA	Self-Organising Time Division Multiple Access
SSS	Side-Scan Sonar
SST	Sea Surface Temperature
TBT	Tributyltin
TCPA	Time to Closest Point of Approach
TRACEr-MAR	Technique for the Retrospective and Predictive Analysis of Cognitive Errors in Maritime Transportation
UKC	Under-Keel Clearance
URN	Underwater Radiated Noise
UV	Ultraviolet (radiation)
VDR	Voyage Data Recorder
VHF	Very High Frequency
VLCC	Very Large Crude Carrier
VOC	Volatile Organic Compounds
WAAS	Wide Area Augmentation System
WHR	Waste Heat Recovery

Glossary

Acoustic impedance
: Product of medium density and sound speed, $Z = \rho\, c$; governs the reflection and transmission of acoustic energy at interfaces between media of different properties.

Airy wave theory
: Linear wave theory describing surface gravity waves through a linearised boundary-value problem for the velocity potential; valid when wave steepness $ka \ll 1$.

Amphidromic point
: Point in the ocean where tidal amplitude is zero; tidal co-phase lines rotate around such points, and the amplitude increases with distance from them.

Antifouling coating
: Surface treatment that prevents or inhibits settlement of marine organisms on ship hulls, maintaining surface smoothness and reducing frictional resistance.

Attained subdivision index
: Probabilistic measure of a ship's damage stability obtained by summing, over all feasible flooding scenarios, the product of the probability of each damage case and its corresponding survival factor.

Ballast water treatment
: Physical or chemical processes—filtration, UV irradiation, electrochlorination—applied to ballast water to eliminate invasive aquatic species before discharge in a different biogeographic region.

Baroclinic
: Fluid condition in which density surfaces and pressure surfaces are inclined to one another, producing horizontal density gradients that drive geostrophic currents.

Beaufort scale
: Empirical wind force scale relating sea state appearance to wind speed; ranges from Force 0 (calm) to Force 12 (hurricane).

Bending moment
Internal rotational force at any cross-section of the hull girder, arising from the difference between weight and buoyancy distributions along the ship's length.

Biofouling
Colonisation of submerged surfaces by marine organisms (algae, barnacles, mussels) that increases surface roughness and hull frictional resistance.

Bore
Translating front of elevated water that propagates into a region of lower water depth under gravity; occurs in tidal rivers, tsunamis, and as a limiting case of cnoidal waves.

Brunt–Väisälä frequency
Maximum oscillation frequency for internal gravity waves in a density-stratified fluid; $N = \sqrt{-(g/\rho)\,\mathrm{d}\rho/\mathrm{d}z}$.

Bryan plate buckling stress
Critical compressive stress at which a flat rectangular plate buckles elastically; depends on the plate aspect ratio, thickness, and boundary conditions.

Buys Ballot's law
Navigation rule: facing the wind in the Northern Hemisphere, the centre of the low-pressure system lies approximately 90° to the right.

Capillary wave
Surface wave with period ~ 0.1 s restored by surface tension rather than gravity; the first ripples generated by wind stress on a calm surface.

Cavitation
Formation of vapour-filled cavities when local pressure falls below the vapour pressure; a dominant source of propeller noise and structural erosion.

Celerity
Phase velocity of a wave; the speed at which an individual wave crest propagates.

Chemical relaxation
Molecular structural rearrangements in seawater (involving $\mathrm{MgSO_4}$ and $\mathrm{H_3BO_3}$) that dissipate acoustic energy at characteristic frequency-dependent rates.

Cnoidal wave
Nonlinear shallow-water wave whose surface profile is expressed using Jacobi elliptic functions; includes the solitary wave as a limiting case when the elliptic modulus approaches unity.

Coastal upwelling
Vertical water motion driven by alongshore wind and Ekman transport divergence, bringing cold nutrient-rich deep water to the surface.

Collision mechanics
Physics of ship-to-ship or ship-to-object impact, divided into external mechanics (rigid-body dynamics and hydrodynamic added mass) and internal mechanics (structural deformation and energy absorption).

Convergence zone (acoustic)
Annular region at approximately 50–65 km range where refracted sound rays converge, producing anomalously high intensity; a key long-range propagation mechanism in deep water.

Coriolis effect
Apparent deflection of moving objects in a rotating reference frame; deflects ocean currents and winds to the right in the Northern Hemisphere and to the left in the Southern Hemisphere.

Corrosion wastage
Progressive loss of structural plate thickness due to chemical oxidation and electrolytic action in the marine environment; reduces hull girder section modulus over time.

Cumulative fatigue damage
Sum of fractional damage increments from each stress cycle experienced by a structural detail; failure is predicted when the Palmgren–Miner sum reaches unity.

Dangerous semicircle
The right-hand half (Northern Hemisphere) of a tropical cyclone's circulation, where the storm's translational velocity adds to the rotational wind speed.

Dead reckoning
Navigation by advancing a known position along a known heading using estimated speed and elapsed time, without external position fixes.

Deep scattering layer
Concentration of sound-reflecting organisms (fish, zooplankton) at depths of 300–700 m that produces volume reverberation and migrates diurnally toward the surface.

Deflagration
Subsonic combustion propagation driven by thermal conduction and molecular diffusion, producing moderate overpressures in confined spaces.

Detonation
Supersonic combustion coupled with a shock wave, producing overpressures an order of magnitude greater than deflagration of the same fuel–air mixture.

Deviation (magnetic compass)
Angular difference between the compass-indicated magnetic north and true magnetic north, caused by the ship's own ferromagnetic structure.

Diffuse attenuation coefficient (K_d)
Exponential decay rate of downward irradiance with depth in seawater; varies with wavelength and water type across the Jerlov classification.

Directional spreading function
Mathematical description of how wave energy distributes across propagation directions; typically modelled using a cosine-power form centred on the dominant wave direction.

Dispersion relation
Frequency–wavenumber relationship for propagating waves: $\omega^2 = gk\tanh(kh)$ for surface gravity waves, linking wave period, wavelength, and water depth.

Doppler effect
Frequency shift observed when a sound source and observer are in relative motion; exploited in ADCP current profiling and sonar target speed estimation.

Double diffusion
Convective instabilities in the ocean arising from the vastly different molecular diffusivities of heat ($\sim 10^{-7}$ m^2/s) and salt ($\sim 10^{-9}$ m^2/s).

Ekman spiral
Rotation and exponential decay of the current velocity vector with depth in the wind-driven surface boundary layer, resulting from the balance of Coriolis force and eddy viscosity.

Ekman transport
Depth-integrated mass transport in the Ekman layer, directed 90° to the right of the wind stress in the Northern Hemisphere; independent of the eddy viscosity magnitude.

Envelope soliton
Exact solution of the nonlinear Schrödinger equation representing a stable, localised wave group in which dispersive spreading and nonlinear self-focussing balance.

Euphotic zone
Sunlit upper ocean layer where downward irradiance exceeds 1% of its surface value; supports photosynthesis and primary production.

Event tree analysis
Forward-looking probabilistic method that traces branching sequences of barrier successes and failures following an initiating event to quantify outcome probabilities.

Exergy
Maximum useful work extractable from a thermodynamic flow stream relative to the ambient environment; governs the potential of waste heat recovery systems.

Faraday's law
The induced electromotive force in a closed conducting loop equals the negative rate of change of magnetic flux through the loop; foundation of electromagnetic induction.

Fault tree analysis
Top-down deductive method that identifies the logical combination of component failures leading to a defined top event (accident or system failure).

Fetch
Horizontal distance over open water along which wind acts on the sea surface; determines the energy input and thus the wave growth potential.

Flashover
Rapid transition from localised fire to fully involved compartment fire, occurring when the upper hot gas layer radiates sufficient flux (~ 20 kW/m^2) to ignite all exposed combustible surfaces.

Flettner rotor
Spinning vertical cylinder that generates lateral aerodynamic lift via the Magnus effect; used as a wind-assisted ship propulsion device.

Floodable length
Maximum compartment length, centred at any longitudinal position, that may be flooded without the vessel sinking below the margin line.

Formal safety assessment
IMO's structured five-step methodology—hazard identification, risk analysis, risk control options, cost–benefit assessment, and recommendations—for developing risk-based maritime regulations.

Frontal system
Boundary between air masses of different temperature and humidity; includes warm fronts, cold fronts, and occluded fronts that govern mid-latitude weather.

Fully developed sea
: Equilibrium wave state in which further energy input from the wind is balanced by dissipation and nonlinear transfer; wave height and period reach their maxima for the given wind speed.

Gaussian plume model
: Atmospheric dispersion model in which pollutant concentration follows Gaussian distributions transverse and vertical to the wind direction downwind of the stack.

Geometric spreading
: Reduction in acoustic intensity with range due to the expansion of wave fronts; spherical spreading gives $\mathrm{TL} = 20\log_{10} R$ and cylindrical spreading gives $10\log_{10} R$.

Geostrophic current
: Ocean current in which the horizontal pressure gradient force is exactly balanced by the Coriolis force, producing flow along isobars.

Global warming potential
: Relative climate forcing factor for a greenhouse gas compared to $\mathrm{CO_2}$ over a specified time horizon; methane has a 100-year GWP of approximately 28–34.

Group velocity
: Speed at which the energy envelope of a wave packet propagates; equals half the phase velocity for deep-water gravity waves.

Hadley cell
: Large-scale atmospheric circulation cell between the equator and approximately 30° latitude, driven by tropical heating and poleward heat transport.

Hogging
: Hull girder bending condition in which the midship region is supported on a wave crest while the bow and stern are in troughs, producing tensile stress in the deck and compressive stress in the bottom.

Hull girder
: The ship treated as a free–free beam subject to distributed weight and buoyancy loads; the primary structural model for longitudinal strength analysis.

JONSWAP spectrum
: Fetch-limited wave energy spectrum developed from the Joint North Sea Wave Project; extends the Pierson–Moskowitz spectrum with a peak-enhancement factor γ.

Jerlov water types
Classification scheme for ocean optical properties based on the diffuse attenuation coefficient K_d; ranges from Type I (clear open ocean) to Coastal 9 (highly turbid).

Life cycle assessment
Standardised methodology (ISO 14040) for quantifying the environmental impact of a product or system over its entire life—from raw material extraction through disposal.

Lost buoyancy method
Damaged stability calculation technique in which the flooded compartment volume is removed from the intact buoyancy, and the vessel's equilibrium is recomputed without the flooded volume.

Margin line
Reference line drawn 76 mm below the upper surface of the bulkhead deck at the ship's side; defines the submergence limit for deterministic damage stability assessment.

Methane slip
Unburnt methane released to the atmosphere from LNG-fuelled engines; must be accounted for in well-to-wake greenhouse gas assessments due to methane's high global warming potential.

Modulational instability
(Benjamin–Feir instability.) Growth of sideband perturbations in a regular deep-water wave train when the wave steepness exceeds a threshold; can lead to rogue wave formation.

Normal mode theory
Decomposition of the underwater acoustic field into a sum of discrete depth-dependent modes, each propagating horizontally with its own phase and group velocity.

Parabolic equation method
Efficient numerical technique for solving the full-wave acoustic propagation problem in range-dependent ocean environments with variable bathymetry and sound speed.

Palmgren–Miner rule
Linear damage accumulation hypothesis: fatigue failure occurs when $\sum n_i/N_i = 1$, where n_i is the number of cycles at stress range i and N_i is the corresponding fatigue life.

Peregrine breather
Exact solution of the nonlinear Schrödinger equation that is localised in both space and time, reaching an amplitude amplification factor of exactly three; a candidate mechanism for rogue waves.

Permeability
Fraction of a compartment's volume actually occupiable by floodwater, accounting for structure, machinery, and cargo; used in damage stability calculations.

Pierson–Moskowitz spectrum
Fully developed wind-wave energy spectrum parameterised solely by wind speed; assumes equilibrium between energy input, dissipation, and nonlinear transfer.

Probabilistic damage stability
Regulatory framework in which a ship's attained subdivision index A must exceed a required index R, with each damage scenario weighted by its statistical probability and survival factor.

Radar equation
Relationship between transmitted power, antenna gain, target radar cross section, and range that determines the received echo power: $P_r \propto \sigma / R^4$.

Redundancy index
Measure of a structural system's tolerance to partial component failure; quantifies the reserve strength available after removal of one or more members.

Reliability index (β)
Probabilistic safety measure defined as the shortest distance from the origin to the failure surface in standard normal space; higher values indicate greater structural safety.

Reverberation
Unwanted return of acoustic energy scattered by the ocean surface, seabed, and volume inhomogeneities; when it exceeds ambient noise, detection becomes reverberation-limited.

Rogue wave
An abnormally large ocean wave—conventionally defined as $H > 2H_s$—that can arise from modulational instability, wave focusing, or current–wave interaction.

Sagnac effect
Optical path length difference experienced by counter-propagating laser beams in a rotating closed loop; the operating principle of ring laser and fibre optic gyroscopes.

Sagging
Hull girder bending condition in which the bow and stern are supported on wave crests while the midship region is in a trough, producing compressive stress in the deck and tensile stress in the bottom.

Shadow zone (acoustic)
Region of the ocean where no direct acoustic rays arrive due to downward refraction; forms beneath a near-surface sound speed minimum and limits sonar detection.

Significant wave height (H_s)
Standard measure of sea severity: $H_s = 4\sqrt{m_0}$, where m_0 is the zeroth spectral moment of the wave energy spectrum.

Snell's law (acoustics)
$\cos\theta/c = \text{const}$ along any acoustic ray path in a horizontally stratified ocean, governing ray bending due to sound speed gradients.

SOFAR channel
Sound speed minimum at approximately 1000 m depth in the open ocean; acts as a waveguide trapping low-frequency acoustic energy over transoceanic distances.

Sonar equation
Fundamental detection criterion comparing the signal excess (source level minus transmission loss plus target strength) against the noise-masking background (noise level minus directivity index plus detection threshold).

Stokes drift
Net forward mass transport by surface waves arising from the difference between forward orbital velocity at the crest and backward velocity at the trough: $\bar{u}_S = \omega k a^2 e^{2kz}$.

Stress concentration factor
Ratio of the peak local stress at a structural discontinuity (notch, weld toe, opening) to the nominal far-field stress; governs fatigue crack initiation.

Sverdrup balance
Relationship between the depth-integrated meridional ocean transport and the wind stress curl; explains the pattern of gyre circulation in the ocean interior.

Thermohaline circulation
Global-scale overturning circulation driven by density differences arising from temperature and salinity variations; transports heat poleward and ventilates the deep ocean.

Tidal constituent
Harmonic component of the tide at a specific astronomical frequency; each constituent is characterised by its amplitude, phase, and Doodson number classification.

Transmission loss
: Reduction in acoustic intensity between a source and a receiver due to geometric spreading and absorption; measured in dB re the intensity at 1 m from the source.

Trochoidal wave
: Classical wave profile in which surface particles trace circular orbits, producing sharper crests and flatter troughs than a sinusoidal wave; historically used for hull girder design loads.

Ursell number
: Dimensionless parameter $U_r = HL^2/h^3$ that measures the relative importance of nonlinear to dispersive effects; when $U_r > 1$, cnoidal wave theory is more appropriate than linear theory.

Waste heat recovery
: Capture and conversion of thermal energy from engine exhaust and cooling water into useful work or electrical power, reducing specific fuel consumption and emissions.

Wave energy spectrum
: Distribution of wave energy density over frequency (and direction), $S(\omega, \theta)$; the foundation of spectral analysis for describing irregular sea states.

Well-to-wake assessment
: Comprehensive emissions accounting that includes upstream fuel production, transport, and bunkering in addition to the on-board combustion emissions.